POLITECNICO DI MILANO

Department of Energy
Doctoral Program in
Energy and Nuclear Science and Technology

DMFC MODELING: MASS TRANSPORT PHENOMENA AND ELECTROCHEMICAL IMPEDANCE SPECTROSCOPY

Doctoral Dissertation of:
Matteo Zago

Supervisor:
Prof. Renzo MARCHESI
Co-supervisor:
Dr. Andrea CASALEGNO
Tutor:
Prof. Fabio INZOLI
The Chair of the Doctoral Program:
Prof. Carlo E. BOTTANI

Year 2013 - XXV Cycle

Abstract

This work aims to propose a combined experimental and modeling analysis in order to provide an insight into the basic principles regulating water transport and impedance behavior in Direct Methanol Fuel Cells (DMFCs). DMFCs are a promising energy source for portable and automotive applications, mainly due to the direct use of a liquid fuel and low emissions. However the widely use of the DMFC technology is still hindered by some technological issues, among which water management is one of the most important. Water crossover through the membrane may cause two problems named anodic water consumption and cathode flooding. Moreover water management can affect DMFC lifetime, that is limited by several interconnected degradation phenomena. The most common technique to monitor system internal losses during real operation is the Electrochemical Impedance Spectroscopy (EIS). Despite the potentiality of this *in-situ* measurement technique, the interpretation of impedance data is still object of discussion in the literature. The interpretation of impedance spectra is usually carried out by means of equivalent electric circuit method (ECM), but in this way, only few useful qualitative information are achieved.
The major outcomes of this work are represented by a steady-state and an impedance DMFC model. The former, that has been validated on three different typologies of measure at the same time over a wide range of operating conditions, increases the understanding of the mechanisms that regulate water transport and flooding in DMFC. The latter, that is constituted by an analytical electric circuit model of cathode and a physical model of the anode, elucidates the origin of impedance features and provides a quantitative interpretation of experimental observations. Moreover the developed impedance model can be applied to the analysis of DMFC degradation tests.

Keywords: Direct Methanol Fuel Cell, Model, Water transport, Flooding, Electrochemical Impedance Spectroscopy.

Contents

Introduction

In the last decades Polymer Electrolyte Membrane Fuel Cells (PEMFCs) attracted increasing attention as energy conversion systems, especially for stationary and mobile applications, due to their advantageous features: high efficiency, high power density, low emissions and modularity. Despite these potentialities, further improvements in terms of performance, durability and cost are necessary before commercial application. Moreover the limited availability of the anode feeding fuel, hydrogen, plays a crucial role in the commercialization of PEMFCs.
The direct methanol fuel cell (DMFC) is a further development of PEMFC technology, particularly promising for portable and automotive applications, mainly due to the direct use of a liquid fuel, quick recharging and low operating temperature. However the widely use of the DMFC technology is still hindered by some technological issues, among which the water management is one of the most important.
DMFCs are fed at the anode with a liquid mixture composed by water and methanol and the water as well as the methanol flow through the membrane from anode to cathode. Water crossover through the membrane may cause two problems named anodic water consumption and cathode flooding. The former enhances methanol cross-over through the membrane, implying fuel waste, the latter decreases oxygen diffusivity at cathode, lowering cell voltage. During the last years, water management in DMFCs has been extensively studied. However the mechanisms that regulate water transport in DMFC are not fully consolidated and limited effort has been dedicated to analyze flooding onset and its consequences on DMFC operation. A detailed comprehension of such phenomena is required to further optimize compo-

nents and operation strategies. For this reason also modeling analysis deals with DMFC. However the most of developed models are validated on few experimental results. This strongly reduces the effectiveness of the models in fuel cell design and optimization.
Moreover water management can affect DMFC lifetime, that is limited by several interconnected degradation phenomena. The most common technique to monitor the system internal losses during real operation is the Electrochemical Impedance Spectroscopy (EIS), that permits to evaluate the kinetic and transport phenomena in the system. Despite the potentiality of this in situ measurement technique, the interpretation of impedance data is still object of discussion in the literature, with no common agreement. Usually the interpretation of experimental observations is carried out by means of equivalent circuit method (ECM). Even though simple and fast, this method is not reliable and provides only few qualitative information.
The main research activities on fuel cell impedance spectroscopy regard the development of innovative modeling approaches, that permit to understand the origin of impedance features and provide a quantitative interpretation of experimental observations. Up to now these activities have been focused on PEMFCs and solid oxide fuel cells (SOFCs) technology. The modeling of DMFC impedance behavior is at the very beginning and in the literature only few simple and not validated models can be found.
In addition to the above described issues, the DMFC suffers from the well known anode sluggish kinetic and methanol permeation from anode to cathode. The understanding of the main physicochemical phenomena regulating these technological problems is consolidated in the literature and the research has been focused on material development: innovative anode catalyst layer and membrane with low methanol permeability.
Considering the presented framework of research activities, this work aims to propose a combined experimental and modeling analysis in order to increase the understanding of the mechanisms that regulate water transport and impedance behavior in DMFC. This work is organized as follows:

- in chapter 1 the fundamental aspects and the research activities regarding DMFC technology are described;
- in chapter 2 a steady-state experimental characterization of mass transport phenomena, mainly focused on water flux at cathode outlet, is reported;
- in chapter 3 a DMFC model is developed to further investigate the effects of water transport on performance (i.e., flooding phenomena) and methanol crossover;

- in chapter 4 a systematic experimental characterization by impedance spectroscopy is performed in order to figure out the most relevant operating parameters on EIS measurements;
- in chapter 5 a preliminary model for quantitative interpretation of DMFC impedance is developed;
- in chapter 6 a detailed physical model of anode impedance is illustrated and its capability to interpret degradation effects is exposed.

Chapter 1

State of the art of Direct Methanol Fuel Cell technology

In the following chapter a summary on the main DMFC properties, issues and research activities is provided with the aim to introduce this technology. More specific information about the related chemical and physical aspects can be found in the cited works.

1.1 Fundamental aspects

A fuel cell is an electrochemical energy device that converts the chemical energy in a fuel directly into electrical energy. Among the different kinds of fuel cells, the direct methanol fuel cell (DMFC) is very promising because of the direct use of a liquid fuel. The basic operating principle of the DMFC is shown in Fig. 1.1.
On the anode, the methanol feed solution is transported from the channel to the catalyst layer, where part of methanol is electrochemically oxidized to form protons, electrons, and CO_2, while the remainder is transported to the cathode through the membrane. The electrochemical reaction on the anode catalyst layer is:

$$CH_3OH + H_2O \longrightarrow CO_2 + 6H^+ + 6e^- \qquad (E_{0,anode} = 0.046V) \qquad (1.1)$$

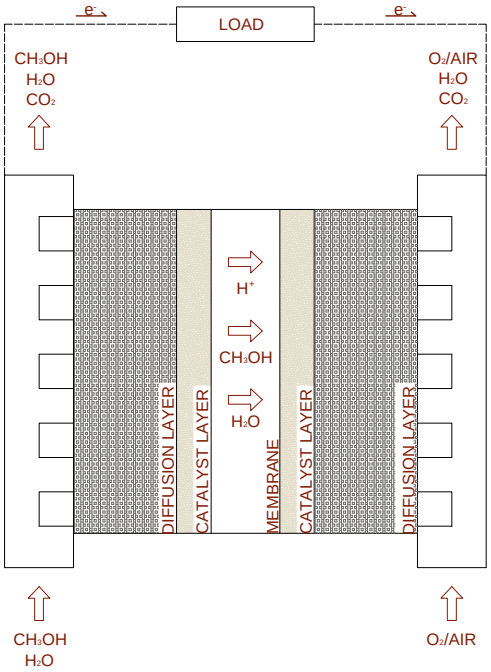

Figure 1.1: DMFC operating principle.

The produced carbon dioxide is transported through the diffusion layer to the flow channel, determining a two-phase flow, and it is then vented out of the cell. This results in a rather complicated mass transport process.
Instead the protons are transported through the ion-conducting membrane to the cathode, where they react with oxygen and electrons, transported through the external circuit, to form water. The electrochemical reaction on the cathode catalyst layer is:

$$6H^+ + 6e^- + \frac{3}{2}O_2 \longrightarrow 3H_2O \qquad (E_{0,cathode} = 1.23V) \tag{1.2}$$

It follows that the overall reaction in the DMFC is:

$$CH_3OH + H_2O + \frac{3}{2}O_2 \longrightarrow CO_2 + 3H_2O \qquad (E_{0,cell} = 1.18V) \tag{1.3}$$

Calculating the thermodynamic open circuit cell voltage (OCV, i.e. without current flow), the Nernst equation predicts values around 1.2 V, depending on methanol feed concentration [1]. Considering an ideal behavior, the theoretical fuel cell voltage of 1.2 V would be realized at all operating currents. Instead, during the real operation, DMFC achieves its highest output voltage at OCV and then the voltage drops off with increasing current. This behavior is known as polarization losses or overpotentials and it is represented by

the polarization curve, that characterizes the output voltage as a function of the current density. An example of a typical DMFC polarization curve is reported in Fig. 1.2.

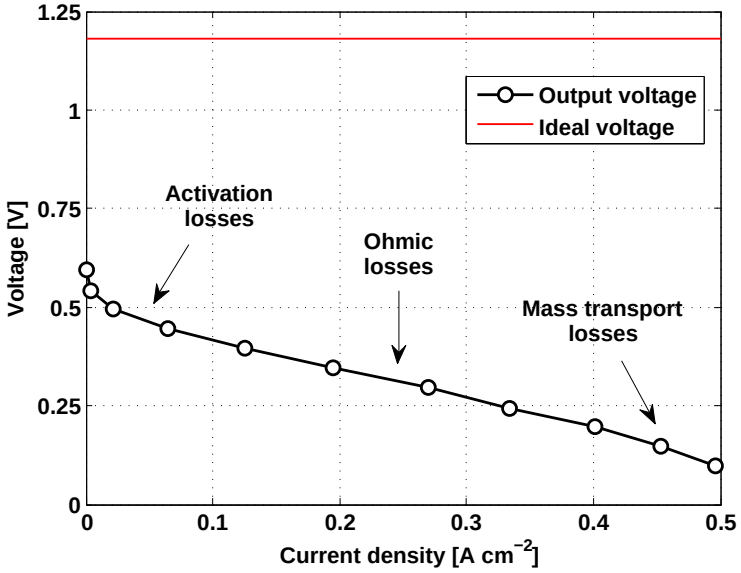

Figure 1.2: DMFC polarization curve.

It is evident that the output voltage is significantly lower than the ideal value. The curve reflects the different limiting mechanisms occurring during DMFC operation: at low current densities the voltage is mainly influenced by the kinetic limitations, while at high current densities mass transport limitations are predominant. In between, where the curve shows a nearly linear trend, the voltage is mainly affected by membrane overpotential, that is due to its ion conductivity.
DMFC presents cathode and membrane overpotentials very similar to hydrogen PEMFC, instead the anode overpotential is much more important, because the methanol oxidation reaction rate is at least three to four orders of magnitude slower than hydrogen electro-oxidation [2], whose overpotential is generally negligible. Moreover the membrane is permeable to methanol and water, that are transported to the cathode with negative effects on DMFC performance and operation. In particular when methanol reaches the cathode it is oxidized, leading to a mixed potential and an inevitable decrease of cathode performance. Furthermore the oxidized methanol is effectively wasted fuel with clear negative impact in the overall efficiency of the cell. Instead the high rate of water cross-over enhances flooding phenomena, hindering the transport and causing a non uniform distribution of oxygen over

the catalyst layer, with a consequent decrease of DMFC performance. In PEMFC technology only a limited hydrogen cross-over is observable, especially at open circuit voltage.
In conclusion, in spite of a similar ideal voltage of about 1.2 V, DMFC exhibits lower voltage than PEMFC at similar current density. Therefore DMFC presents lower efficiency (30%[1]) and power density (0.1-0.2 $W \cdot cm^{-2}$) compared to PEMFC, characterized by an efficiency of nearly 50% and a power density up to 1.5 $W \cdot cm^{-2}$.

1.2 DMFC components

Fig. 1.3 illustrates the components of a typical DMFC, that consists of a membrane electrode assembly (MEA) sandwiched by anode and cathode distributors. The MEA is a multi-layered structure that is composed of an anode diffusion layer (DL), an anode catalyst layer (CL), a polymer electrolyte membrane (PEM), a cathode catalyst layer (CL) and a cathode diffusion layer (DL). A brief description of these components is reported in the following paragraphs.

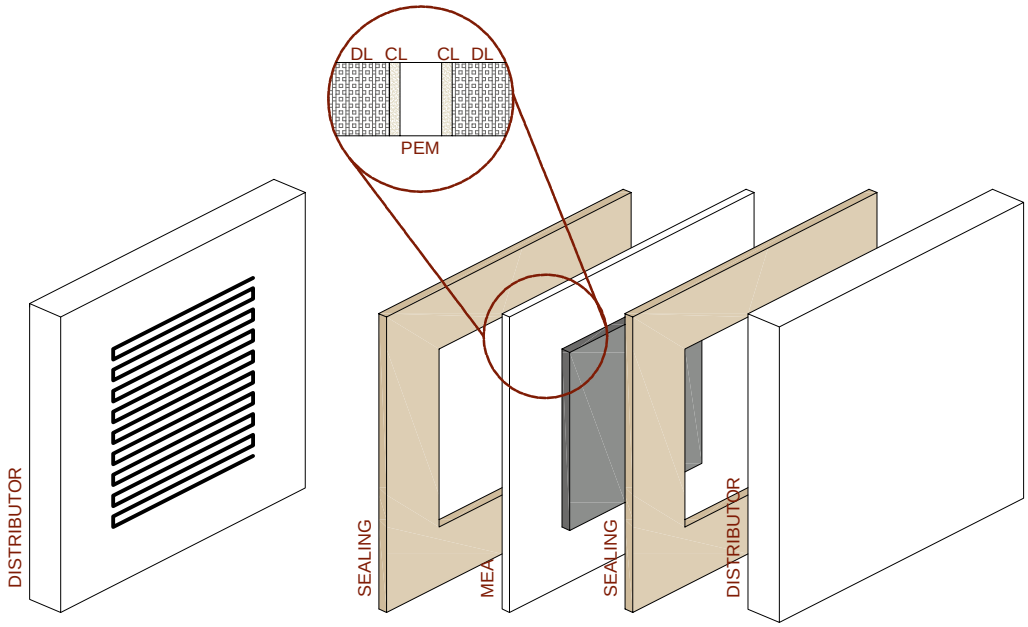

Figure 1.3: DMFC components.

[1]The efficiencies reported in this work are calculated on the base of low heating value (LHV), to permit a direct comparison with traditional technologies.

1.2.1 Proton exchange membrane

The main function of the membrane is to conduct protons from the anode to the cathode and to provide electronic insulation between the two catalyst layers. Furthermore common requirements for a polymer electrolyte membrane in DMFC applications include: low methanol and ruthenium crossover and high chemical and mechanical durability [3]. The most commonly used membrane is the perfluorinated sulfonic acid (PFSA) polymer membrane, developed by DuPont and named Nafion®. PFSA polymers exhibit high proton conductivity only when fully hydrated due to their typical water assisted proton transport mechanism. In fact in such systems the proton transfer is mainly due to the physical movement of hydronium ions (H_3O^+), that cross the polymer membrane. Water is thus involved with proton transport: at least 3 molecules of water can move together with a proton, generating what is named water electro-osmotic drag [4, 5]. The liquid nature of DMFC anode feeding favors membrane hydration.
Typical thickness of PFSA membranes for DMFC applications is included between 100-200 μm; it is higher than PEMFC one (50-60 μm) in order to partially reduce methanol cross-over.

1.2.2 Catalyst layers

The fundamental function of the anode and cathode catalyst layers is to promote methanol oxidation and oxygen reduction, respectively. The CLs are also characterized by good proton and electron conductivity. In fact both anode and cathode CLs are made of carbon supported catalysts mixed with ionomer in order to provide the triple-phase boundaries, where the simultaneous transport of protons, electrons and reactants/products takes place [6].
Methanol oxidation is a slow reaction that requires multiple active sites for the adsorption of methanol and for the formation of OH_{ads} species, that completely oxidize to CO_2 the adsorbed methanol residues. Until now the best effective catalyst is the bimetallic platinum-ruthenium, in ratio from 1:1 to 2:1.
Instead the most utilized catalyst for oxygen reduction at DMFC cathode is platinum, the same catalyst of PEMFC technology. However in DMFC electrodes a higher catalyst loading is necessary, 1-2 $mg \cdot cm^{-2}$, in order to enhance the slow methanol electro-oxidation at the anode and to improve oxygen reduction at the cathode, limited by methanol cross-over. Usually catalyst layers have a reduced thickness, included between 10 and 25 μm.

1.2.3 Diffusion layers

The function of diffusion layers is to ensure a uniform distribution of reactants over the catalyst layers. In addition the diffusion layers are the support to the corresponding catalyst layer and the electrical conductor, that transports electrons to the current collector [7]. Typically, gas diffusion layers are constructed from porous carbon paper, or carbon cloth, with a thickness in the range of 100-300 μm.
The diffusion layers also assist in water management during DMFC operation. Diffusion layers are normally wet-proofed with a PTFE (Teflon) coating, so that the surface and pores in the diffusion layer are not fully obstructed by liquid water. Moreover diffusion layer is often composed by an additional micro porous layer (MPL), characterized by a reduced porosity and a high hydrophobicity. The presence of MPL plays a significant role in reducing water cross-over through the membrane [8] and flooding phenomena [9] during DMFC operation.

1.2.4 Distributors

Distributors are designed to permit reactants and products transport to and from the corresponding diffusion layers. Moreover distributors have to ensure electron conduction to the current collector and to minimize pressure losses, in order to reduce the power demand of auxiliary components, as pumps and compressors. Distributors are composed by a system of channels, with a typical cross-section of 1 mm x 1 mm, that are machined in a metallic or graphite plate. The most common distributors have serpentine or parallel channels. In both anode and cathode channels the typical Reynolds number varies in the range of 100-1000 and therefore the flows are laminar [10].

1.3 Research activities

DMFC has been extensively studied in the last decades. The main advantage of this technology for portable and automotive applications is the direct use of a liquid fuel. However, the fuel is also the cause of its major drawbacks: anode sluggish kinetic, methanol cross-over, complicated water management and severe degradation. The most of the work in the literature report systematic experimental analyses, but a deep understanding of the physicochemical phenomena governing DMFC operation has been carried out by means of modeling.
In the following paragraphs the main research activities regarding the DMFC technology are described.

1.3.1 Anode kinetics and methanol cross-over

The electrochemical oxidation of methanol is complicated; in the overall reaction six electrons are transferred and consequently many reaction intermediates can be expected. A relatively large number of publications propose different reaction mechanisms [11, 12, 13, 14]. The conclusion of all these works is the presence of some very stable reaction intermediates and a widely accepted opinion is that carbon monoxide is the long-living intermediate [1], which is the responsible of the slow overall reaction kinetics. However the reaction mechanism is still not fully understood and the optimization of the catalysts is thus more complicated. Up to now the most common catalyst for methanol oxidation is the carbon supported platinum-ruthenium, but the development of alternative catalyst is still in progress. In [15] an extensive review is reported: some promoting effects can be achieved by the presence of element such as Sn, Mo, W, Os, as well as some refractory metal oxides. Furthermore other researchers are aiming to optimize the nature of the support, the catalyst particle size and the atomic ratio between platinum and ruthenium. A thinner support layers can improve the performance [16] and a reduced particles size is beneficial for methanol oxidation [17].
Another critical issue related to the anode feeding is the methanol cross-over. When methanol comes into contact with the membrane it is transported to the cathode by three transport mechanisms: electro-osmotic drag by proton transport, diffusion by methanol concentration gradient and convection by the hydraulic pressure gradient [18]. During typical DMFC operation diffusion is the predominant transport mechanism. In the literature methanol cross-over has been extensively studied both experimentally and theoretically [19, 20, 21, 22, 23]. It has been widely demonstrated that it is closely related to membrane structure, morphology and thickness, and DMFC operating conditions such as temperature, pressure, and methanol concentration. The understanding of the physical phenomena governing methanol cross-over is already consolidated in the literature and the researches are focusing on the modifications of PFSA membranes to reduce methanol cross-over. The most promising solutions include the deposition of palladium films on the surface [24] and the creation of composite membranes, obtained with the addition of both organic-inorganic composites and acidic-basic polyaryl composites. In [3, 18] a detailed review on DMFC membranes is reported.

1.3.2 Water management

The water management issue has been going with DMFCs since the initial development of this technology in 1990. Until nowadays, several studies in this

area are still continuing for achieving better DMFC performance and understanding of the physical phenomena regulating water transport [25, 26, 27]. The major cause of the water management issue is the PFSA polymer membrane, that exhibits high proton conductivity only when fully hydrated. The liquid nature of DMFC anode feeding enhances membrane hydration: the water as well as the methanol flow through the membrane from the anode to the cathode [28].
However water crossover through the membrane may cause two problems named anodic water consumption [29, 30, 31] and cathode flooding [32, 33, 34, 35]. The increased water consumption, caused by water crossover through the membrane, implies the necessity of additional water feeding and storage, reducing the compactness of the DMFC systems [32, 36]. Secondly, the high rate of water crossover increases the cathode flooding, especially during dynamic operation, therefore a suitable management of water transport and flooding is considerably important in order to improve DMFC performance and stable operation.
During the last years, water crossover in DMFCs has been extensively studied [37, 38, 39, 40]. It has been found that the cathode gas diffusion layer (GDL), composed by a carbon macro-porous layer and usually by an additional micro-porous layer (MPL) coated on it, plays an important role in both water crossover through the membrane and water removal to the cathode. The effect of cathode GDL properties on water transport in DMFCs has been widely investigated [41, 42, 43]. Several works studied also how to minimize water transport, especially in passive DMFC, modifying the GDLs characteristics in anode and cathode [44, 45, 46]. The characterization of flooding onset and its effect on the performance has not been significantly examined, despite this phenomenon could occur also in optimized DMFC during dynamic operation or after GDL degradation [47].

1.3.3 Degradation

At present, the degradation of DMFC is still one of the major concerns on the commercialization of this technology [48, 49, 50]. The performance degradation rates of DMFC, generally higher than that of hydrogen-air PEMFCs, are typically in the range of 10-25 $\mu V \cdot h^{-1}$ [51] and can be divided into a permanent and a temporary component [52, 53]; the latter is recoverable after operation interruption. Despite this subject is attracting a growing scientific interest [54, 55, 56], in the literature only few experimental investigations can be found. These works mainly focus on catalyst characterization before and after the degradation test, highlighting the presence of different degradation mechanisms such as catalyst agglomeration, ruthenium dissolution

and crossover, carbon corrosion, membrane thinning and loss of hydrophobic properties of the GDLs [57, 58]. The temporal evolution of the above cited degradation mechanisms and their dependence on the operating conditions are a very difficult topic, due to the complexity of the different interconnected degradation phenomena and the long time test. Moreover the deficiency of standard test procedures makes the comparison between different durability tests more difficult.
At the moment fuel cells degradation is studied in a wide and growing number of research projects [59], among which the European project Premium Act [60] is very interesting. One of the primary goal of this project is to develop a reliable method, based on combined experimental and modeling approach, that can predict system lifetime and improve operating strategies with respect to a durability target. Nonetheless a detailed comprehension of each different degradation mechanism is necessary to develop a such reliable methodology. For this reason particular effort is dedicated to electrochemical impedance spectroscopy (EIS), an in situ measurement technique that permits to monitor the system internal losses during continuous operation. Despite its potentiality the interpretation of EIS data is still object of discussion in the literature [61] and modeling becomes crucial to analyze experimental observations.

1.3.4 Model development

Modeling deals with both water transport [62, 63, 64] and EIS [65, 66] in DMFCs. Regarding water management some works can be found in the literature. Schultz and Sundmacher [67] presented a one-dimensional dynamic model, validated also on water transport experimental measurements, neglecting the two-phase behavior in both diffusion layers and flooding effects. Ko et al. [68] developed a 1-D model where the two-phase behavior was considered, but water diffusion in gas phase through the cathode GDL was neglected and the model was validated on a single operating condition. Yang and Zhao [69, 70] presented a complete two dimensional and two-phase DMFC model, validated only on the experimental performance and a limited set of operating conditions was considered. Casalegno et al. [71, 72, 73] presented a 1-D model validated with respect to overall polarization, anode polarization, methanol cross-over, showing a good agreement with the experimental data, but water transport was not analyzed in detail. Pasaogullari and Wang [74] developed a two phase numerical model to analyze the multilayer cathode GDL. They particularly investigated the effects of porosity, thickness and hydrophobicity of an MPL on the two-phase transport [74]. The results showed that the addition of the MPL between catalyst layer and

GDL could enhance liquid water removal and reduce the liquid saturation in the catalyst layer. However the proposed model [74] considers only the two-phase transport of reactants and products across cathode GDL, neglecting the modeling of all the others cell components.
Therefore in the literature there is no comprehensive works on water transport modeling, in which the validation is approached systematically over a wide range of operating conditions and with respect to different typologies of measure. Such a work would be necessary to increase the understanding of the phenomena regulating water transport in DMFC. Moreover a consolidate interpretation of water management would be useful to increase the comprehension of DMFC lifetime, that is limited by several interconnected and complex phenomena [75, 76].
As mentioned in paragraph 1.3.3, the interpretation of impedance measurements is very complicated and modeling plays a fundamental role in the analysis of experimental data. Until now the interpretation has mostly been carried out by means of equivalent circuit method (ECM) [77, 78, 79, 80]. Though simple and fast, this method is not reliable, since the equivalent circuit is not unique; moreover ECM provides only few useful qualitative information.
M. Orazem [81] proposed an innovative and relatively simple approach for a quantitative interpretation of EIS measurements: the developed methodology consists in expressing the equivalent circuit element as a function of the physical parameters of the system. In [82] this method was used for the interpretation of PEMFC cathode impedance, but in principle it could be applied to any electrochemical system, including DMFC.
An alternative approach is represented by physically based EIS models, that in the last years attracted increasing scientific interest. The development and experimental validation of this type of models are very complicated, but the results are not related to the choice of a suitable equivalent electric circuit. In the literature many works regarding both SOFC [83, 84, 85] and PEMFC [86, 87] technology can be found. Bessler et al. carried out an extensive physically based model activity on SOFC [88, 89, 90]: the flexibility and modularity of the developed models, including detailed elementary kinetic electrochemistry and diffusion processes, allowed the assignment of the origin of SOFC impedance features with high accuracy. Springer et al. [91] developed one of the first numerical models for PEMFC cathode impedance: the first impedance loop was attributed to the effective charge-transfer resistance and double-layer charging, while the second one was related to the mass-transport limitation in the gas phase.
In DMFCs the anode catalyst layer internal losses are not negligible, as in PEMFC technology, and moreover the mass transport phenomena at anode

side are very complex, due to the two-phase and multi component nature of the flows. Thus the interpretation of impedance behavior is even more complicated than in PEFC and SOFC technology and in fact in the literature only two recent physical models of DMFC cathode are present [65, 66], while for the anode there is no reference. However the proposed models [65, 66] are only 1-D in the direction of electrode thickness and no attempts to fit experimental data have been done.
Therefore a validated model for a quantitative interpretation of DMFC impedance would be necessary to increase the understanding of all the physicochemical phenomena regulating the operation of this technology.

1.4 Aims of the work

Considering the above described research activities, this work, carried out in the framework of Premium Act project [60], aims to systematically investigate water transport and impedance behavior in DMFC by means of a combined experimental and modeling approach.
The first objective of the work is to increase and consolidate the understanding of the phenomena governing DMFC water transport. In particular in chapter 2 an experimental characterization of mass transport phenomena, mainly focused on water flux at cathode outlet, is reported. Subsequently, in chapter 3, an interpretation model is developed to further investigate the effects of water transport on performance (i.e., flooding phenomena) and methanol crossover.
Instead the second objective of the work is to develop DMFC impedance models for a quantitative interpretation of experimental observations. In chapter 4 a systematic experimental characterization by EIS is performed to figure out the most influent operating parameters and to provide an insight into the development of interpretation models. In chapter 5 a preliminary innovative model, based on analytical equivalent circuit, is developed; while in chapter 6 a detailed physical model of anode impedance is illustrated and its capability to interpret degradation effects is exposed.

Chapter 2

Mass transport phenomena: experimental analysis

A complete experimental characterization of fuel cell mass transport phenomena and performance is reported in this chapter. The investigation is based on the analysis of water fluxes at cathode outlet, methanol cross-over and polarization curves under a wide range of operating conditions. Moreover the effect of different GDL configurations is evaluated.

2.1 Experimental setup

The experimental analyses of DMFC performance and methanol crossover are carried out implementing, in the equipment previously developed [92], the measure of water concentration at cathode outlet.
Cathode side was modified introducing, Fig. 2.1:

- a heat exchanger to warm up the cathode exhaust to evaporate eventual liquid water;
- a thermo-hygrometer for humidity (uncertainty 2%) and temperature (uncertainty 0.2 ℃) measurements, located in a thermo-stated housing to avoid condensation.

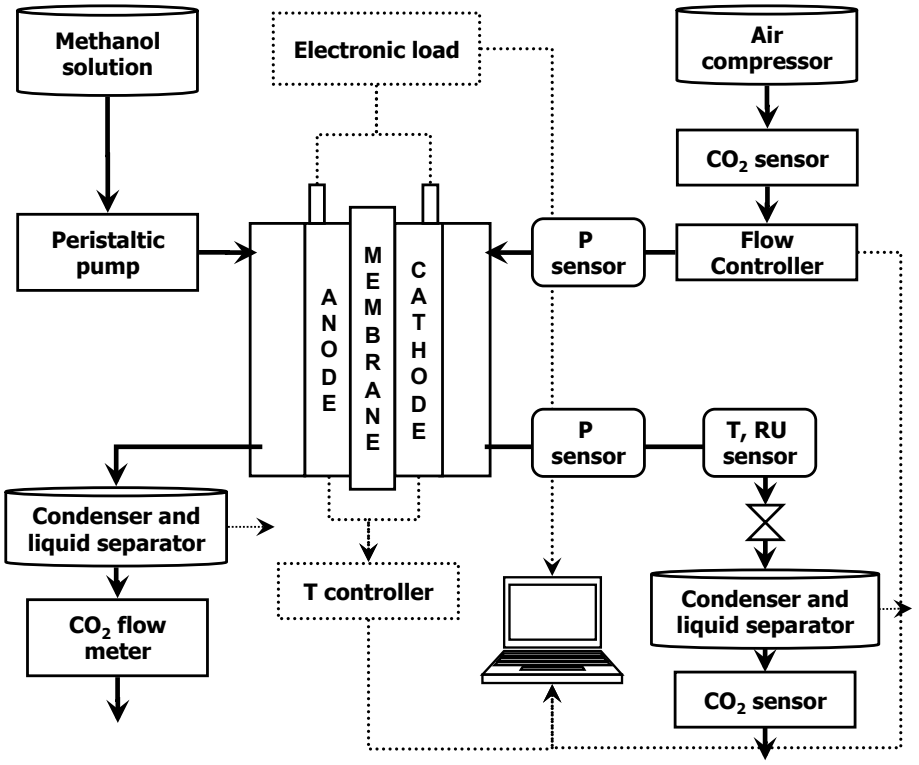

Figure 2.1: Experimental setup scheme.

The above modifications permit to measure the water content in the cathode exhaust $X^c_{H_2O}$ and considering the mass balance equations 1-8 reported in [92], the water flow at the cathode outlet is given by:

$$N^{H_2O,c}_{out} = X^c_{H_2O} \cdot N^c_{out,tot} \tag{2.1}$$

These new components have negligible pressure drop and do not increase considerably the transient time necessary to reach steady state in the vessels.
The experimental analysis is carried out on the three MEAs already characterized in [92]:

- MEA GM, GDL without MPL at anode and GDL with MPL at cathode;
- MEA GG, GDL without MPL on both anode and cathode;
- MEA MM, GDL with MPL on both anode and cathode.

A set of the measurement already examined in [92] have been reproduced by means of the improved experimental setup. Note that in all the investigated operating conditions (Table 2.1[1]) the anode flow rate is set at 1 $g \cdot min^{-1}$ and the anode mean pressure at 105 kPa. The results of performance and methanol crossover reported in [92], as well as measurement uncertainty and reproducibility evaluation, remain valid. The uncertainty associated to the measurement of water flow is evaluated, according to [93], equal to 7% in the whole investigated range.

MEA	T $[K]$	X_{CH_3OH} $[\%wt]$	$\dot{m}_{air}$ $[g \cdot min^{-1}]$	p^c_{in} $[kPa]$	p^c_{out} $[kPa]$
GM	333	3.25	0.62	112	108
GM	333	3.25	0.62	151	147
GM	333	3.25	1.14	122	115
GM	333	3.25	1.14	155	148
GM	333	6.50	0.62	112	108
GM	333	6.50	0.62	151	147
GM	333	6.50	1.14	122	115
GM	333	6.50	1.14	155	148
GM	353	3.25	0.62	112	108
GM	353	3.25	1.14	122	115
GM	353	6.50	0.62	112	108
GM	353	6.50	1.14	122	115
GG	333	3.25	0.62	112	108
GG	333	3.25	1.14	122	115
GG	333	6.50	0.62	112	108
GG	333	6.50	1.14	122	115
GG	333	6.50	1.14	155	148
GG	353	6.50	1.14	122	115
MM	333	3.25	0.62	112	108
MM	333	3.25	1.14	122	115
MM	333	6.50	0.62	112	108
MM	333	6.50	1.14	122	115
MM	333	6.50	1.14	155	148
MM	353	6.50	1.14	122	115

Table 2.1: Investigated operating conditions.

[1]In the followings unpressurized cathode is named as 1 *bar*, instead pressurized cathode is named as 1.5 *bar*.

2.2 Experimental analyses

2.2.1 Influence of operating conditions (MEA GM)

In Fig. 2.2 the water flow at cathode outlet, in function of current density, is reported for different operating conditions. A general behavior can be

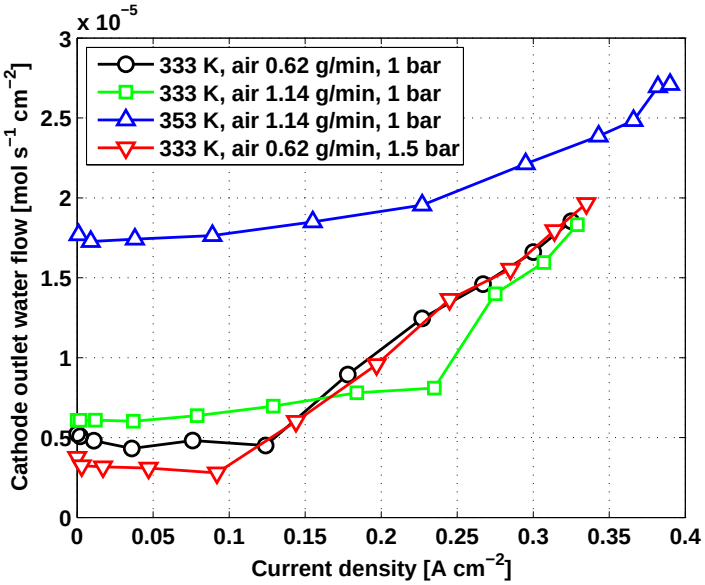

Figure 2.2: Influence of operating conditions on water flux (MEA GM, methanol concentration 3.25%).

distinguished: at low current density the water flow is approximately constant, a sort of plateau is evident, then it increases, in some cases suddenly, with an approximately linear trend. This behavior suggests the presence of two different mechanisms regulating water transport to cathode channel. A possible interpretation could be based on the two main mechanisms of water transport through GDL reported in the literature [94]: diffusion in vapor phase and permeation in liquid phase.
The plateau could be caused by water vapor diffusion through the cathode GDL, determined by an approximately constant water concentration along the cathode electrode. Small current density variations do not affect significantly water concentration profile. Instead at higher current density the linear trend could be due to the onset of liquid water permeation, forced by enhanced electro-osmotic drag and water production at cathode, both directly proportional to current density.
This preliminary interpretation is discussed analyzing the experimental results in different operating conditions.

The proposed plateau origin is coherent with the following considerations regarding Fig. 2.2:

- an increase of airflow rate induces a decrease of water concentration in cathode channel, as a consequence the water concentration difference across the GDL and the relative diffusive flow grow; therefore the water flow at cathode outlet, i.e. the plateau value, increases;
- an increase of temperature determines a general increment of both GDL diffusivity and water concentration at cathode electrode, related to saturation concentration; thus the water flow at cathode outlet increases;
- at higher cathode mean pressure, the total gas mixture concentration increases, therefore at similar water concentration, water fraction $X^c_{H_2O}$ lowers; consequently the plateau value decreases, according to Eq. 2.1.

Regarding the linear behavior at higher current density, the curves at lower temperature assume the same linear trend, coherently with the proposed dependence on electro-osmotic drag and water production, not affected considerably by the airflow or pressure variation.
A further confirmation of the proposed interpretation is obtained comparing the experimental results at higher methanol concentration, Fig. 2.3. Doubling methanol concentration, the plateau values do not change signif-

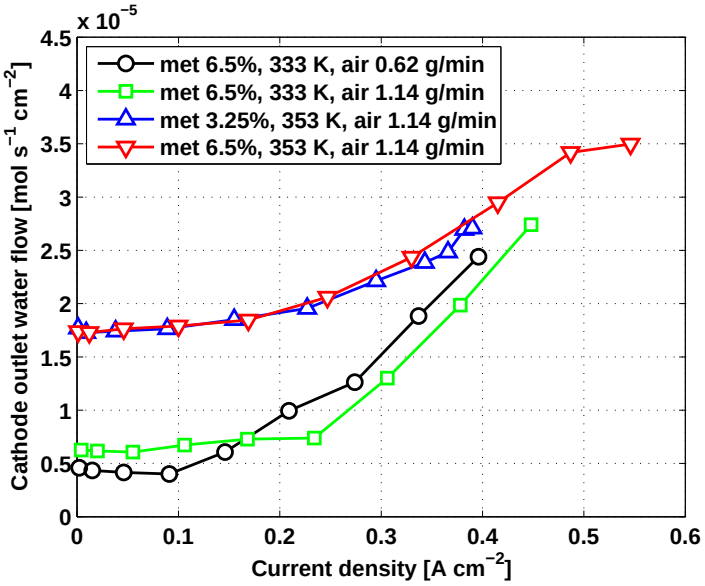

Figure 2.3: Influence of operating conditions on water flux (MEA GM, cathode pressure 1 *bar*).

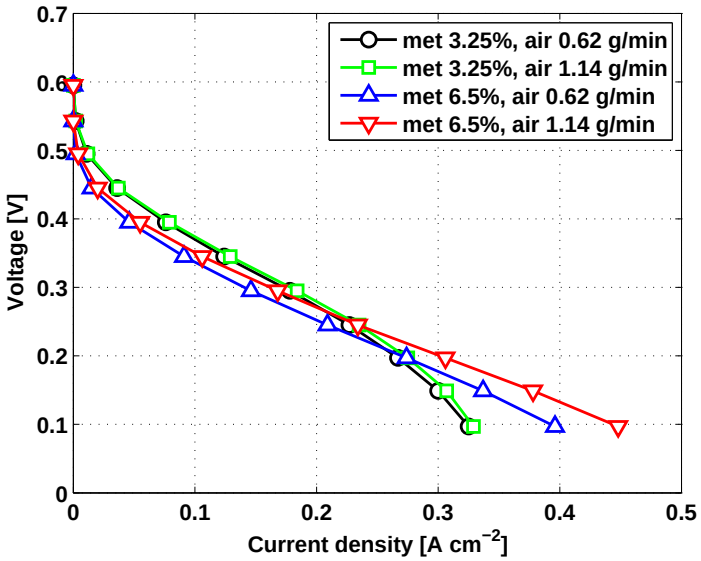

Figure 2.4: Influence of operating conditions on performance at 333 K and 1 *bar* (MEA GM).

icantly, while the performances are considerably different, Fig. 2.4, as well as the methanol crossover [92]. Therefore, the plateau is confirmed to be influenced exclusively by cathode flow conditions. Moreover a linear trend with a similar slope is present, as expected in these operating conditions, Fig. 2.3.
A consequence of the considerable water transport through the cathode GDL is the pore flooding that hinders oxygen transport and DMFC performance. Liquid water permeation through the GDL is expected to cause a significant pores obstruction. A comparison of polarization curves in different operating conditions is reported in Fig. 2.4. At low methanol concentration an increase of airflow rate determines negligible variations of DMFC performance. In contrast, water flow at cathode outlet varies significantly and considerable water permeation is expected to occur in both cases at high current density. This behavior can be explained considering that the performance at high current density is strongly limited by the anode feeding, worsen by low methanol concentration, as discussed previously in [92]. In such conditions, the effect of an oxygen transport hindered by flooding is undetectable.
The behavior is different at higher methanol concentration: the performance is not anymore limited by anode feeding but a negative effect of airflow reduction is evident. The water transport increases at high current density when the airflow decreases, Fig. 2.3. Both the lower airflow rate and the increased water flow imply a reduction of oxygen concentration at cathode electrode

leading to a decrease in the performance. The performance decrease could be due to such oxygen concentration reduction or to a further pore flooding effect, but it cannot be distinguished from these experimental results. A further interpretation of this aspect is discussed in the next paragraph.

2.2.2 Cathode MPL influence (MEA GG)

In order to clarify the effect of water transport on DMFC performance, the results regarding the MEA GG (without cathode MPL) and the MEA GM (with cathode MPL) are discussed and compared. In Fig. 2.5, the water

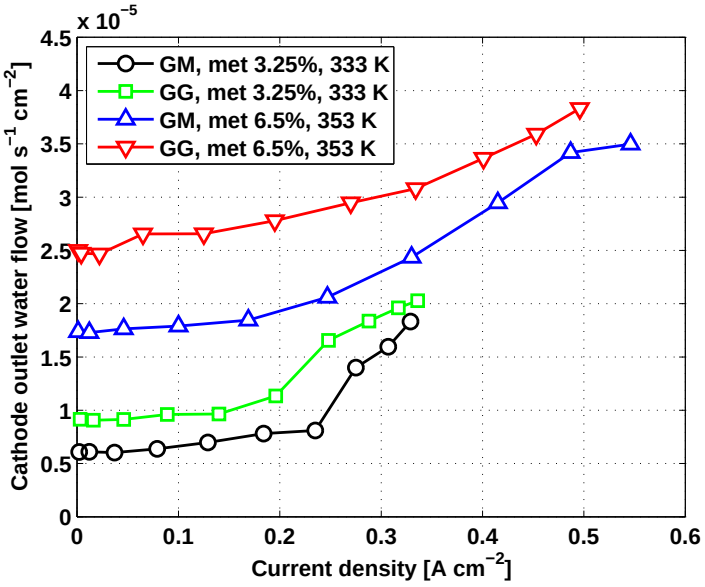

Figure 2.5: Influence of operating conditions on water flux with airflow of 1.14 $g \cdot min^{-1}$ at 1 bar.

flow at the cathode outlet for the two MEAs is reported. An enhanced water transport is evident in the MEA without MPL: the mass transfer resistance at cathode side decreases eliminating the additional micro-porous layer, coherently with the results reported in [95]. The plateau rises approximately by a factor 1.5 in both the two temperature conditions.
Morevoer analyzing methanol crossover measurements reported in Fig. 2.6, it is evident that there is a consistency with the water transport measurements of Fig. 2.5. An enhanced water flux at cathode outlet causes an increase of the average methanol concentration at anode side. Coherently with this mechanism of dilution, MEA GG exhibits a higher methanol crossover than MEA GM.

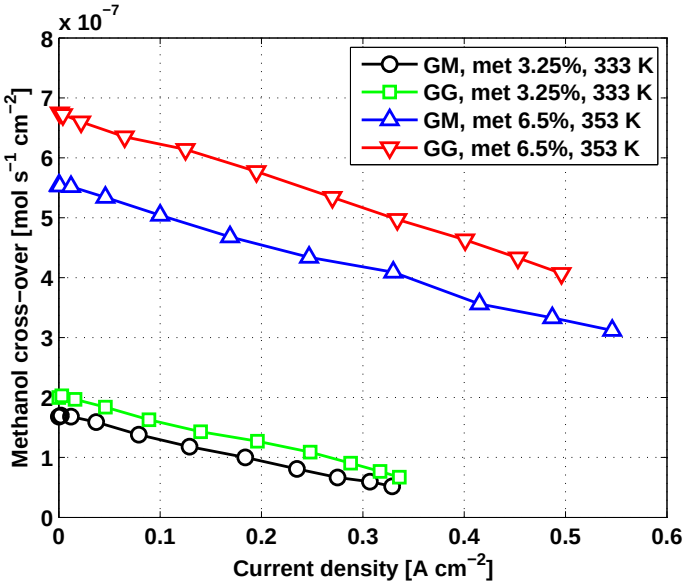

Figure 2.6: Influence of operating conditions on methanol corss-over with airflow of 1.14 $g \cdot min^{-1}$ at 1 bar.

A general improvement of performance is evident with cathode without MPL, Fig. 2.7, accordingly to the enhanced mass transport through the GDL that increases oxygen concentration at cathode electrode. A clear exception is evident: the performance of MEA GG drops and becomes lower than MEA GM one at current density higher than 0.35 $A \cdot cm^{-2}$. This behavior has been already found in literature [9, 96, 97] and it is probably caused by a considerable GDL flooding phenomenon.
In order to confirm flooding presence and quantify its effect a specific modeling analysis is reported in the next chapter.

2.2.3 Anode MPL influence (MEA MM)

In order to further investigate the effect of water transport on DMFC operation, the experimental data regarding MEA MM (with MPL on both anode and cathode) are compared with those of MEA GM. In Fig. 2.8 the water flow at cathode outlet is reported. Considering MEA MM a reduced water transport is evident: this feature is coherent with a lower water crossover through the membrane, due to the presence of a liquid water barrier to the anode (i.e., the MPL). The water flow of MEA MM is nearly constant as the current density changes: this implies that the only mechanism governing water transport through cathode GDL is gas diffusion. Moreover the plateau

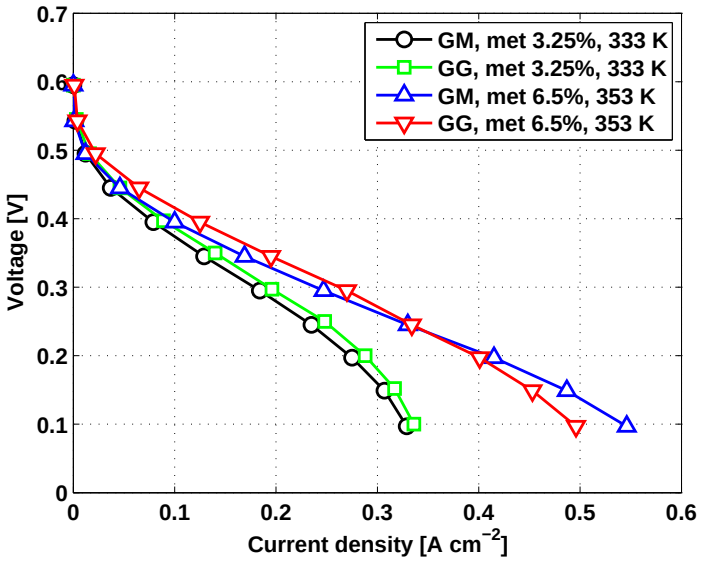

Figure 2.7: Influence of operating conditions on performance with airflow of 1.14 $g \cdot min^{-1}$ at 1 bar.

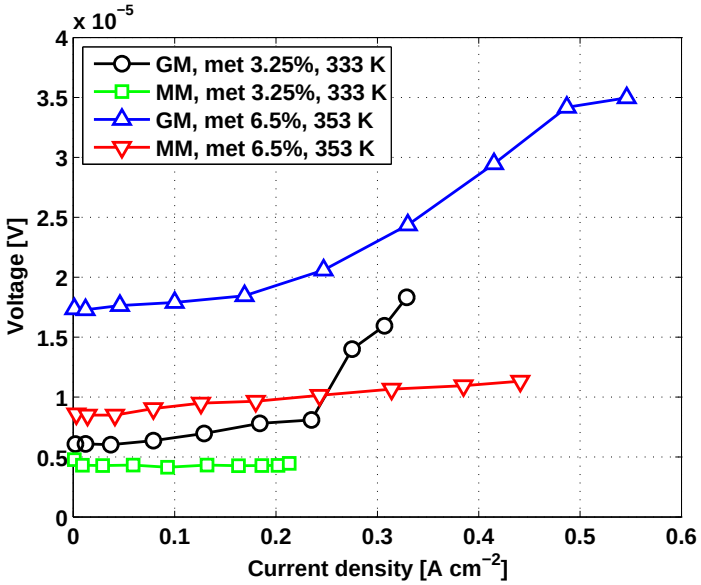

Figure 2.8: Influence of operating conditions on water flux with airflow of 1.14 $g \cdot min^{-1}$ at 1 bar.

value decreases: the reduced water cross-over lowers cathode water concentartion.
The presence of anode MPL nearly halves methanol cross-over (Fig. 2.9). This is partially due to the reduced water cross-over: in fact, as already ob-

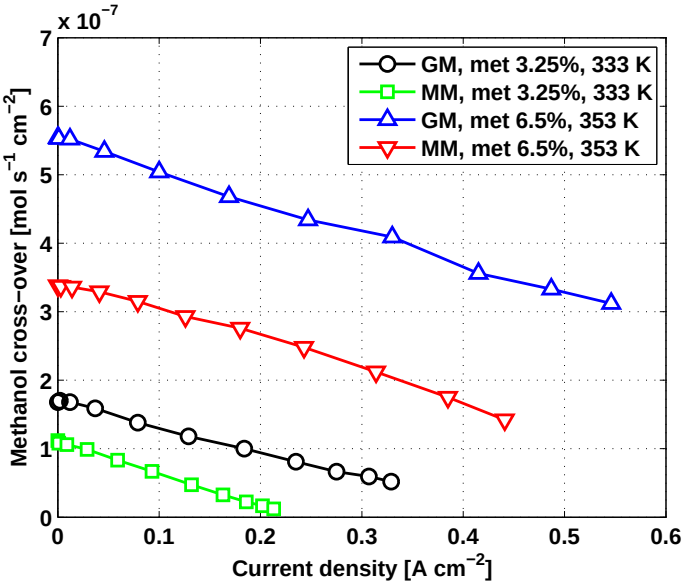

Figure 2.9: Influence of operating conditions on methanol cross-over with airflow of 1.14 $g \cdot min^{-1}$ at 1 bar.

served in Fig 2.6, the lower the water flux at cathode outlet, the lower the methanol crossover. However the magnitude of dilution effect is not sufficient to cause such a marked reduction of methanol cross-over: the presence of anode MPL increases mass transfer resistance entailing a further reduction of avergae methanol concentration.

2.3 Remarks

The proposed experimental analysis underlines the importance of the water transport in the operation of DMFC. In particular the following considerations have been highlighted:

- The water removal from the cathode GDL is regulated by two different transport mechanisms: gas diffusion and liquid permeation. The former determines a plateau at low current densities, the latter a linear trend at high current densities; influence of temperature, pressure and airflow confirm the expectations.

- The absence of cathode MPL causes a general increase of water flow at cathode outlet, that favors methanol cross-over. The higher cathode oxygen diffusivity generally enhances DMFC performance, but some exceptions are evident, probably due to cathode flooding phenomenon.
- The presence of a liquid water barrier at the anode (i.e., the MPL) implies a reduction of both methanol and water cross-over and the water removal from the cathode is mainly governed by gas diffusion.

In order to validate the proposed interpretation of water management and its impact on performance and methanol crossover, a DMFC model has been developed in the following chapter.

Chapter 3

Mass transport phenomena: model development

In this chapter the model already presented in [71, 72] is integrated with equations, that describe water transport phenomena and flooding effects. The original model includes the complete mass balance, considering two-phase anode flow, but single-phase cathode flow and consequently cathode flooding was not considered. Moreover the water crossover is calculated as the sum of electro-osmosis and liquid phase diffusion, neglecting liquid water concentration at cathode side.
In the new model the implementation of water transport phenomena, including two-phase cathode flow and flooding, is introduced to validate the proposed interpretations of water transport and elucidate flooding effects on performance.

3.1 Water transport description

According to the proposed interpretation, the water fluxes through a DMFC are those illustrated in Fig. 3.1. The water availability at anode side is considered to be very high and the anode GDL is assumed to be flooded with fully liquid pathways [35], therefore the water transport through the MEA is generally regulated by water transport through membrane and cathode

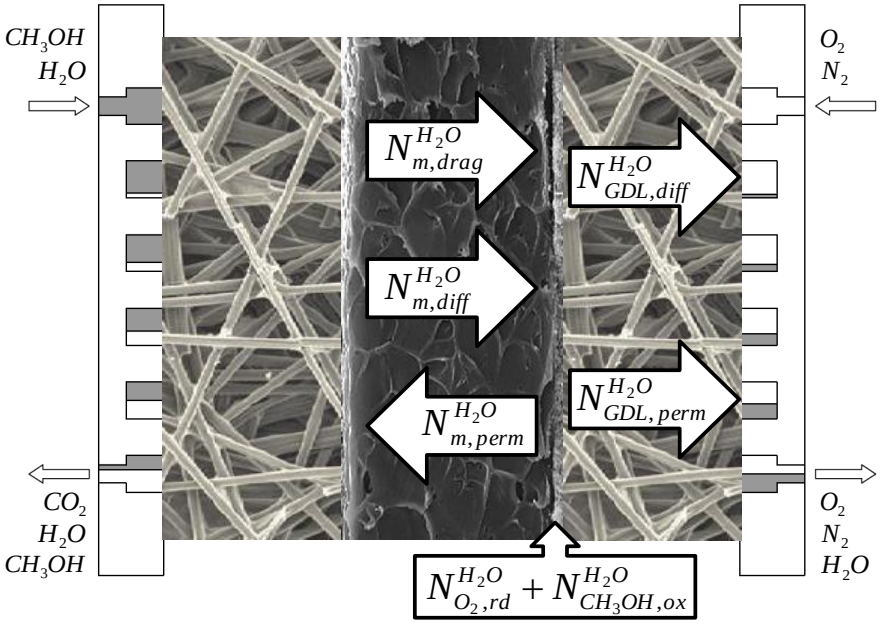

Figure 3.1: Water fluxes through the DMFC.

diffusion layer, in agreement with the literature [96].

3.1.1 Membrane

The water cross-over through the membrane is due to three transport mechanisms [98, 99, 100], electro-osmotic drag by proton transport, diffusion by water concentration gradient and convection by hydraulic pressure gradient, as reported in the following equation:

$$N^{H_2O}_{m,cross} = N^{H_2O}_{m,drag} + N^{H_2O}_{m,diff} - N^{H_2O}_{m,perm} \tag{3.1}$$

The water flux due to electro-osmotic drag can be determined from:

$$N^{H_2O}_{m,drag} = \eta_d \cdot \frac{i}{F} \tag{3.2}$$

Permeation flux depends on the liquid pressure difference across the membrane and can be expressed as:

$$N^{H_2O}_{m,perm} = \frac{K_m \cdot \rho_{H_2O}}{\mu_{H_2O} \cdot M_{H_2O} \cdot l_m} \cdot \left(p^{c,L}_{H_2O} - p^{a,L}_{H_2O} \right) \tag{3.3}$$

Since the flow velocity through the liquid pathways of anode GDL can be neglected, $p^{a,L}_{H_2O}$ is assumed equal to the total pressure in the anode flow channel p^a. At cathode side material hydrophobicity and water transport could

determine a considerable capillary pressure, thus $p_{H_2O}^{c,L}$ can be significantly greater than gas pressure. The capillary pressure is proportional to water saturation in the electrode [101] and consequently to liquid concentration at membrane interface [45]:

$$\Delta p_c = p_{H_2O}^{c,L} - p_{H_2O}^{c,G} \quad \propto \quad s \quad \propto \quad C_{H_2O}^{m,c,L} \tag{3.4}$$

This dependence is uncertain and strongly affected by material characteristics, in fact a general correlation is not available in literature[1]. In the present work a first order dependence is assumed:

$$C_{H_2O}^{m,c,L} = W_2 \cdot \left(p_{H_2O}^{c,L} - p_{H_2O}^{c,G} \right) \tag{3.5}$$

where W_2 is calibrated over experimental data.
Due to negligible gas pressure gradient across the entire porous media, $p_{H_2O}^{c,G}$ can be assumed equal to total cathode pressure p^c, as widely accepted in literature [74]. Generally, under typical operating conditions $p_{H_2O}^{c,L}$ is greater than $p_{H_2O}^{a,L}$, leading to a permeation flux from cathode to anode. Both anode and cathode total pressures are assumed to vary linearly with channel length x:

$$p_{in}^{a,c} - (p_{in}^{a,c} - p_{out}^{a,c}) \cdot \frac{x}{L} = p^{a,c} \tag{3.6}$$

The flux of water due to liquid diffusion can be expressed as:

$$N_{m,diff}^{H_2O} = \frac{D_{m,H_2O}}{l_m} \cdot \left(C_{H_2O}^{m,a,L} - C_{H_2O}^{m,c,L} \right) \tag{3.7}$$

where $C_{H_2O}^{m,a,L}$ and $C_{H_2O}^{m,c,L}$ represent, respectively, liquid water concentrations at the membrane interfaces. Generally, the magnitude of both $C_{H_2O}^{m,a,L}$ and $C_{H_2O}^{m,c,L}$ depends on the properties of the MEA and the operating conditions. Moreover in the literature magnitude and direction of water diffusion flux are controversial [102, 103]. In this work $C_{H_2O}^{m,a,L}$ is assumed equal to the liquid concentration corresponding to a fully hydrated membrane, with water content about 30 [104]; $C_{H_2O}^{m,c,L}$ is already defined in Eq. 3.5.

3.1.2 Cathode diffusion layer

The water flow through cathode GDL, $N_{GDL}^{H_2O}$, is equal to the sum of water cross-over through the membrane, $N_{m,cross}^{H_2O}$, and water sources in the cathode

[1]Note that the correlations reported in literature [45] are generally between the saturation and the dissolved water concentration in the ionomer of the catalyst layer, that is different from membrane one, $C_{H_2O}^{m,c,L}$.

catalyst layer due to methanol cross-over oxidation, $N^{H_2O}_{CH_3OH,ox}$, and to oxygen reduction, $N^{H_2O}_{O_2,rd}$, according to:

$$N^{H_2O}_{GDL} = N^{H_2O}_{CH_3OH,ox} + N^{H_2O}_{O_2,rd} + N^{H_2O}_{m,cross} \tag{3.8}$$

$$N^{H_2O}_{GDL} = 2 \cdot N^{H_2O}_{CH_3OH,cross} + \frac{i}{2 \cdot F} + N^{H_2O}_{m,cross} \tag{3.9}$$

As reported in [94], the water flow through GDL is due to different contributions: diffusion and permeation in gas phase and permeation in liquid phase. The assumption of a constant gas phase pressure across the entire porous media [74] allows neglecting gas permeation through the GDL. Therefore water transport through cathode GDL occurs mainly by vapor diffusion, $N^{H_2O}_{GDL,diff}$, and liquid permeation, $N^{H_2O}_{GDL,perm}$, according to the proposed interpretation. The two-phase behavior at cathode side is simplified as a plug flow, where plugs and bubbles have the same local velocity. Equation 14 of the original model [71] is replaced by the following:

$$\frac{h^c}{2} \cdot \frac{\partial \left(v^c \cdot \bar{C}^c_{H_2O} \right)}{\partial x} = N^{H_2O}_{GDL,diff} + N^{H_2O}_{GDL,perm} \tag{3.10}$$

$\bar{C}^c_{H_2O}$ is the time-averaged total water concentration in the cathode channel, defined as:

$$\begin{cases} \bar{C}^c_{H_2O} = C^{c,G}_{H_2O} & \text{if} \quad \bar{C}^c_{H_2O} \leq C^{sat}_{H_2O} \\ \bar{C}^c_{H_2O} = \varepsilon^c \cdot C^{sat}_{H_2O} + (1 - \varepsilon^c) \cdot \dfrac{\rho_{H_2O}}{M_{H_2O}} & \text{if} \quad \bar{C}^c_{H_2O} > C^{sat}_{H_2O} \end{cases} \tag{3.11}$$

where ε^c is the cathode volumetric gas fraction.
According to [95], the overall mass transport coefficient in gas-phase can be determined from:

$$R^G_{H_2O} = R^G_{H_2O,conv} + R^G_{H_2O,diff} = \frac{1}{h_{conv}} + \left(\frac{l_{GDL}}{D_{GDL}} + \frac{l_{MPL}}{D_{MPL}} \right) \tag{3.12}$$

where h_{conv} is the convective mass transport coefficient in the channel. The resulting water flux can thus be expressed as:

$$N^{H_2O}_{GDL,diff} = \frac{\left(C^{t,c,G}_{H_2O} - C^{c,G}_{H_2O} \right)}{R^G_{H_2O}} \tag{3.13}$$

where $C^{t,c,G}_{H_2O}$, the water vapor concentration in the cathode electrode, depends on the liquid concentration in the membrane interface $C^{m,c,L}_{H_2O}$; the data reported in [5] are interpolated with a third order polynomial.

The interpretation of water permeation onset at high current density is reported in the experimental analysis discussion and it is implemented in the model as follows. Water diffusion through cathode GDL led to an increase of water concentration along the cathode channel: this transport mechanism becomes less and less considerable along cathode channel when its driving force diminishes.
This implies an increase of the liquid pressure in the cathode electrode, $p_{H_2O}^{c,L}$: when it becomes greater than a threshold value, p_{lim}, liquid permeation through cathode GDL occurs. The values of $p_{H_2O}^{c,L}$ and $N_{GDL,perm}^{H_2O}$ are calculated by solving the following water balance at electrode-GDL interface:

$$\begin{aligned} N_{m,drag}^{H_2O} + N_{m,diff}^{H_2O} - N_{m,perm}^{H_2O} + N_{CH_3OH,ox}^{H_2O} + N_{O_2,rd}^{H_2O} \\ = N_{GDL,diff}^{H_2O} + N_{GDL,perm}^{H_2O} \end{aligned} \tag{3.14}$$

considering the following two cases:

$$\text{if } p^{c,L} \leq p_{lim} \quad \begin{cases} N_{m,perm}^{H_2O} = \dfrac{K_m \cdot \rho_{H_2O}}{\mu_{H_2O} \cdot M_{H_2O} \cdot l_m} \cdot \left(p_{H_2O}^{c,L} - p_{H_2O}^{a,L} \right) \\ N_{m,diff}^{H_2O} = \dfrac{D_{m,H_2O}}{l_m} \cdot \left(C_{H_2O}^{m,a,L} - W_2 \cdot p_{H_2O}^{c,L} \right) \\ N_{GDL,perm}^{H_2O} = 0 \end{cases}$$

$$\text{if } p^{c,L} > p_{lim} \quad \begin{cases} N_{m,perm}^{H_2O} = \dfrac{K_m \cdot \rho_{H_2O}}{\mu_{H_2O} \cdot M_{H_2O} \cdot l_m} \cdot \left(p_{lim} - p_{H_2O}^{a,L} \right) \\ N_{m,diff}^{H_2O} = \dfrac{D_{m,H_2O}}{l_m} \cdot \left(C_{H_2O}^{m,a,L} - W_2 \cdot p_{lim} \right) \\ N_{GDL,perm}^{H_2O} = N_{m,drag}^{H_2O} + N_{m,diff}^{H_2O} - N_{m,perm}^{H_2O} \\ \qquad + N_{CH_3OH,ox}^{H_2O} + N_{O_2,rd}^{H_2O} - N_{GDL,diff}^{H_2O} \end{cases} \tag{3.15}$$

3.2 Flooding description

It is widely known that flooding reduces fuel cell performance, while the effective mechanisms are not fully understood. Many authors agree on the main reason known as the hindrance of oxygen transport caused by GDL and electrode pore obstruction with liquid water [68, 70, 101]. The following model does not pretend to be a detailed and exhaustive description of

such complex phenomenon, but a tool to increase its understanding and for further studies. In this work, flooding effects are modeled considering two contributions:

- Superficial pores obstruction, Fig. 3.2a: if water concentration in cathode channel exceeds the saturation value, drops of water condense on GDL surface[2]. This effect is considered as a reduction of GDL diffusivity proportional to liquid water concentration [95], where correlations for similar GDLs are proposed. A suitable one is adapted as follows:

$$D^c_{GDL,O_2} = D^c_{GDL,eff,O_2} - B_1 \cdot \left(\bar{C}^c_{H_2O} - C^{sat}_{H_2O}\right)^{0.58} \tag{3.16}$$

  where B_1 is derived from the model calibration.

- Bulk pores obstruction, Fig. 3.2b: if liquid water permeation through cathode GDL occurs, the flow obstructs GDL pores, establishing liquid pathways [105]. Both effects imply a reduction of GDL diffusivity proportional to liquid water permeation through cathode GDL[3]. To take into account this effect a correlation is proposed:

$$D^c_{GDL,O_2} = D^c_{GDL,eff,O_2} - B_2 \cdot \left(N^{H_2O}_{GDL,perm}\right)^{B_3} \tag{3.17}$$

  where B_2 and B_3 are obtained by model calibration.

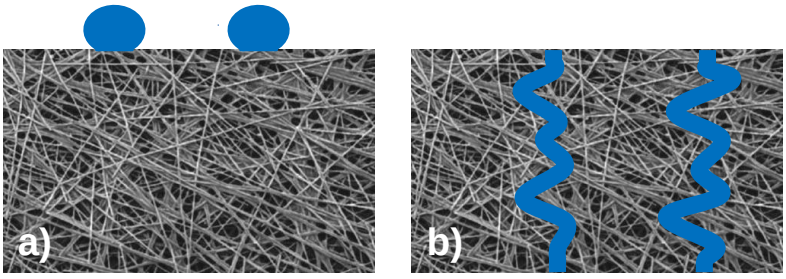

Figure 3.2: a) Superficial pores obstruction. b) Bulk pores obstruction.

[2]Generally liquid water is not present in bulk GDL because of its high hydrophobicity.

[3]Bulk obstruction of MPL is neglected, because its saturation is generally much lower than GDL one [70]. Anyway the GDL diffusivity reduction includes also the eventual MPL one.

3.3 Model validation

The proposed DMFC model is constituted by 7 differential equations, 29 algebraic equations, 36 variables and two correlations to take into account flooding effects, Eq. 3.16 and 3.17. This DAE system is solved in MATLAB®, applying the appropriate initial conditions, regarding inlet flows, potential difference and fuel cell temperature and pressures. The values of the parameters utilized for the calculation are reported in Table 3.1.
The calibration procedure consists in the minimization of the residuals between model estimation and experimental results and permits to determine the values of the most uncertain physicchemical parameters. The considered experimental data set for calibration concern the MEA GM and is composed of 132 measurement points, coming from 12 polarization curves, Table 2.1. The model is calibrated with respect to three different typologies of measure: performance, water transport and methanol cross-over. The residuals between model results and experimental data have reasonably normal distribution and they are generally lower than measurement uncertainty for all the three typologies of measure. This implies that the model is sufficiently accurate to estimate the available experimental results and that the phenomena neglected with the proposed assumptions have minor effects. A comparison between simulations and experimental measurements of water transport in two very different operating conditions is reported as example in Fig. 3.3.

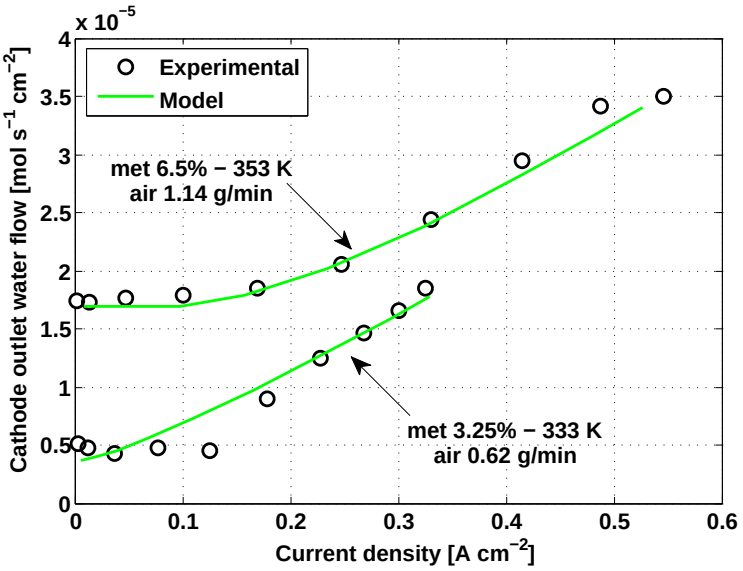

Figure 3.3: Comparison of the simulated and measured water fluxes at cathode outlet (MEA GM, 1 *bar*).

$D^c_{MPL,eff}$	W_3	$cm^2 \cdot s^{-1}$	Cal.
$D^c_{GDL,eff}$	$1.59 \cdot 10^{-1} \cdot (T/333)^{1.75}$	$cm^2 \cdot s^{-1}$	[95]
$D^{a,L}_{GDL,CH_3OH}$	$10^{-5.4163-999.778/T} \cdot 10^4$	$cm^2 \cdot s^{-1}$	[106]
$D^{a,G}_{GDL,CH_3OH}$	I_1	$cm^2 \cdot s^{-1}$	Cal.
D_{m,CH_3OH}	$C_1 \cdot exp\,(C_2 \cdot (1/303 - 1/T))$	$cm^2 \cdot s^{-1}$	Cal.
D_{m,H_2O}	$4.17 \cdot 10^{-4} \cdot 22 \cdot (161 \cdot$ $exp\,(-22) + 1) \cdot exp\,(-2436/T)$	$cm^2 \cdot s^{-1}$	[45]
$h_{conv,@333K}$	$0.115 \cdot 10^2$	$cm \cdot s^{-1}$	[95]
$h_{conv,@353K}$	$0.125 \cdot 10^2$	$cm \cdot s^{-1}$	[95]
C^a_{ref}	$1 \cdot 10^{-3}$	$mol \cdot cm^{-3}$	[107]
C^c_{ref}	$7.25 \cdot 10^{-6}$	$mol \cdot cm^{-3}$	[107]
γ^a	I_2	$-$	Cal.
γ^c	1	$-$	[62]
α^a	I_3	$-$	Cal.
α^c	0.6	$-$	[72]
i^a_*	$I_4 \cdot exp\,(I_5/R \cdot (1/353 - 1/T))$	$A \cdot cm^{-2}$	Cal.
i^c_*	$1.37 \cdot 10^{-4} \cdot exp$ $(50750/R \cdot (1/353 - 1/T))$	$A \cdot cm^{-2}$	[72]
σ_m	$0.073 \cdot exp\,(1268 \cdot (1/298 - 1/T))$	$\Omega^{-1} \cdot cm^{-1}$	[108]
K_m	W_1	m^2	Cal.
$p_{lim,MPL}$	6700	Pa	[105]
$C^{m,c,L}_{H_2O}$	$W_2 \cdot \left(p^{c,L}_{H_2O} - p^{c,G}_{H_2O}\right)$	$mol \cdot cm^{-3}$	Cal.
η_d	$W_4 \cdot exp\,(1029 \cdot (1/333 - 1/T))$	$-$	Cal.
η_{dx}	$C_3 \cdot exp\,(C_4 \cdot (1/333 - 1/T))$	$-$	Cal.
ρ_{H_2O}	$(-0.0028 \cdot (T - 273)^2 - 0.1757 \cdot$ $(T - 273) + 1003.8) \cdot 10^{-3}$	$g \cdot cm^{-3}$	[106]
μ_{H_2O}	$3.56 \cdot 10^{-4}$	$Pa \cdot s$	[106]
K_{H,CH_3OH}	$2.2 \cdot exp\,(5200 \cdot (1/T - 1/298))$	$mol \cdot J^{-1}$	[106]
K_{H,CO_2}	$3.5 \cdot exp\,(2400 \cdot (1/T - 1/298))$	$mol \cdot J^{-1}$	[106]
E_0	1.21	V	$-$
F	94495	$C \cdot mol^{-1}$	$-$
R	8314	$J \cdot mol^{-1} \cdot K^{-1}$	$-$
l_m	0.018	cm	$-$
l^c_{MPL}	0.005	cm	$-$
l^c_{GDL}	0.025	cm	$-$
l^a_{GDL}	0.03	cm	$-$
A_{cell}	22.1	cm^2	$-$
h^a	0.08	cm	$-$
h^c	0.08	cm	$-$
L	138.125	cm	$-$

Table 3.1: Parameters utilized for the calculation (Cal.=Calibrated).

All the obtained values of fitting parameters are coherent with those reported in the literature. The fitting parameters of performance, Table 3.2, are composed of quantities affected by high uncertainty, demonstrated by a high variability in the literature [62, 107, 108, 109].

		Present work	Literature
I_1	$cm^2 \cdot s^{-1}$	$2.17 \cdot 10^{-2}$	$2.36 \cdot 10^{-2}$ [110]
I_2	–	$6.5 \cdot 10^{-2}$	0 [107], 0.5 [62], 1 [111]
I_3	–	0.5	0.5 [70]
I_4	$A \cdot cm^{-2}$	$2.69 \cdot 10^{-4}$	$94.25 \cdot 10^{-4}$ [107] to $2 \cdot 10^{-4}$ [70]
I_5	$J \cdot mol^{-1}$	66712	70000 [112]
B_1	–	37	[95]
B_2	–	$5.24 \cdot 10^2$	–
B_3	–	0.8	–

Table 3.2: Fitting parameters of performance.

The effective methanol diffusivity in the gas phase through the diffusion layer is noticeably uncertain, considering the contribution of CO_2 convective transport, the variation in void fraction and the methanol mixture phase transition. The obtained value is very close to that reported in [110]. The order of the overall anode reaction, γ^a, in literature varies from 0 [107] to 0.5 [62] to 1 [111]; the value obtained by calibration, 0.065, evidences a very weak current dependence on methanol concentration. With regard to the fitting parameters for flooding effects, the value of B_1 is very similar to that reported in [95], instead for the values of B_2 and B_3 there is no reference for comparison. Nevertheless the reduction of cathode diffusivity due to liquid water flux through cathode GDL can be considered reasonable and is discussed in the next paragraph.
The fitting parameters for water transport are reported in Table 3.3.

		Present work	Literature
W_1	m^2	$3 \cdot 10^{-19}$	$2 \cdot 10^{-18}$ [70] to $1 \cdot 10^{-21}$ [107]
W_2	–	$7.7 \cdot 10^{-6}$	–
W_3	$cm^2 \cdot s^{-1}$	$2.38 \cdot 10^{-2}$	$1.55 \cdot 10^{-2}$ [113]
W_4	–	4.6	2.9 [5] to 6 [114]

Table 3.3: Fitting parameters of water transport.

For the fitting parameter W_2 there is no reference in the literature; anyway

the resulting values of $C_{H_2O}^{m,c,L}$, in the investigated conditions, are always coherent with a highly hydrated membrane. Electro-osmotic drag coefficient has a considerable variability [104]: the most of the works reports a value of about 3 at 333 K [4, 38, 5], some studies higher values, near 6 [104, 114], moreover this value can increase considerably when methanol is present [114]. The resulting value of 4.6 at 333 K is thus considered acceptable.
The fitting parameters reported in Table 3.4 characterize methanol cross-over through the membrane.

		Present work	Literature
C_1	$cm^2 \cdot s^{-1}$	$2.17 \cdot 10^{-6}$	$0.5 \cdot 10^{-6}$ [42] to $4.9 \cdot 10^{-6}$ [70]
C_2	K	1976	2436 [70]
C_3	$-$	1.81	2.9 [71] to 0.87 [72]
C_4	K	410	1029 [71]

Table 3.4: Fitting parameters of methanol cross-over.

C_3 is methanol drag coefficient, the fitting value, 1.82, lower than water drag coefficient, confirms the influence of methanol concentration gradient in the membrane, as reported in [72]. The dependence of electroosmotic drag on temperature, C_4, is lower than that reported in [71], evidencing a limited effect of temperature.
Summarizing, the values of the parameters obtained by calibration result are acceptable and coherent with those reported in literature. This consideration, together with the high accuracy of the model in reproducing the experimental results, provides a first validation of the proposed interpretation and model of water transport in DMFC.

3.4 Modeling results discussion

Fig. 3.4 illustrates the water fluxes through the GDL at different current densities: when liquid permeation occurs, the magnitude of diffusion flux diminishes due to the increased water concentration in the cathode channel. At high current densities, when cathode flooding occurs, the permeation is the predominant water transport mechanism.
Fig. 3.5 reports the water fluxes through the membrane. It is interesting to note that permeation flux is negligible and is directed from cathode to anode. On the contrary the diffusion flux is always directed from anode to cathode; at low current densities it is the predominant water transport mechanism, due to a low water concentration at cathode side, while at high

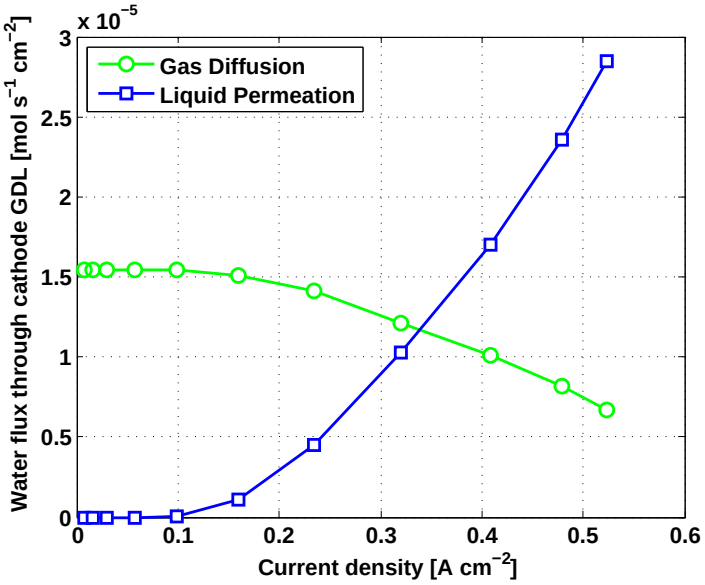

Figure 3.4: Water fluxes through cathode GDL (MEA GM, met 6.5%, 353 K, air 1.14 $g \cdot min^{-1}$, 1 bar).

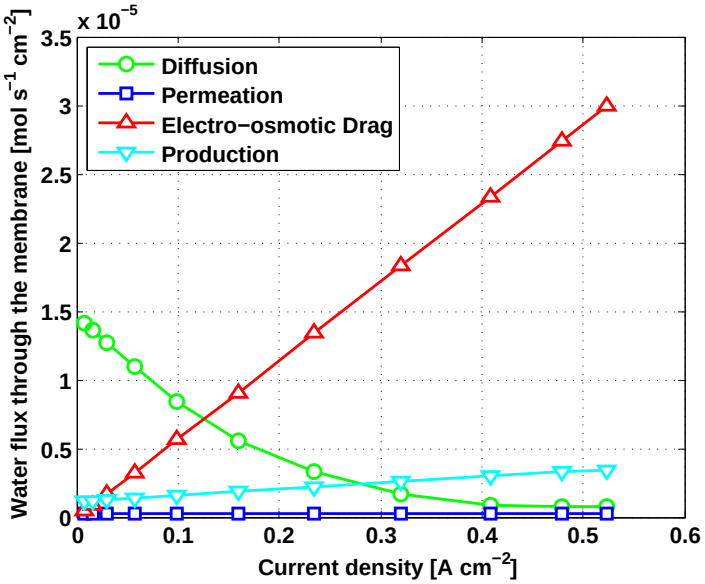

Figure 3.5: Water fluxes through the membrane (MEA GM, met 6.5%, 353 K, air 1.14 $g \cdot min^{-1}$, 1 bar).

current densities it becomes negligible. The resulting trend of membrane water fluxes is coherent with that reported in [70].
In this paragraph a specific analysis of flooding effects on performance and a further validation of the model on MEA GG and MEA MM experimental results are reported.

3.4.1 Flooding effects

The developed model appears able to predict the flooding onset and to quantify its effects. Fig.3.6 reports a comparison between simulation results with

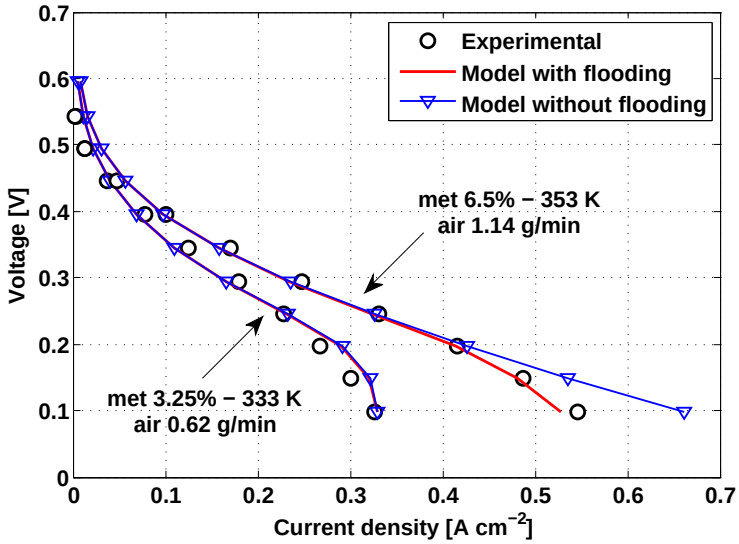

Figure 3.6: Comparison of simulated performances with and without flooding effects (MEA GM, 1 *bar*).

and without the implementation of flooding effects, in the same operating conditions of Fig. 3.3. At lower methanol concentration, the water flow at cathode outlet is low and the modeling results with and without the implementation of flooding effects are superimposed: this indicates that flooding does not occur. Instead at higher methanol concentration, where flooding is expected as discussed in paragraph 2.2.1, a considerable difference omitting flooding model is evident at high current density: this indicates that flooding occurs significantly at current densities higher than 0.4 $A \cdot cm^{-2}$.
A specific analysis is carried out to evaluate the contributions of the two flooding phenomena considered in the present model, superficial and bulk pore obstructions. Fig. 3.7 illustrates a comparison of modeling results ex-

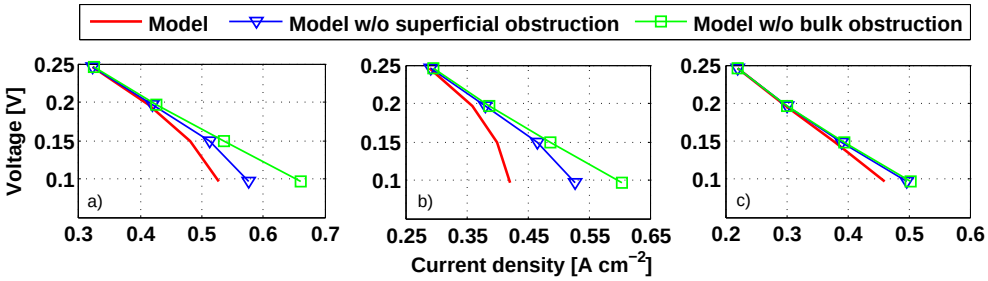

Figure 3.7: Effects of superficial and bulk obstruction (MEA GM, 1 *bar*) a) met 6.5%, 353 K, air 1.14 $g \cdot min^{-1}$, b) met 6.5%, 353 K, air 0.62 $g \cdot min^{-1}$, c) met 6.5%, 333 K, air 0.62 $g \cdot min^{-1}$.

cluding superficial or bulk pore obstruction correlations, in three different operating conditions, in order to distinguish and quantify their effects:

- in Fig. 3.7a, the effect of bulk obstruction is much more relevant than the superficial one;
- in Fig. 3.7b, water concentration in cathode channel increases due to the lower airflow rate, enhancing water condensation and superficial obstruction, nevertheless bulk obstruction is still more influent;
- in Fig. 3.7c, the saturation concentration diminishes due to the lower temperature, leading to a further enhancement of water condensation on GDL surface. In this case bulk and superficial obstructions are comparable.

Generally the effect of bulk obstruction is more relevant compared to the superficial obstruction one. However both types of obstruction must be taken into account to accurately reproduce experimental data: calibrating the model without one type of obstruction, the model accuracy decreases dramatically.
Fig. 3.8 reports the current density profiles along the channel at different voltages. From Fig. 3.6 it is possible to figure out that flooding occurs at voltages lower than 0.2 V. Analyzing the current density profiles, a flooding effect is already evident at 0.2 V: the current density profile presents a more steep decrease than at 0.3 V. The slope decreases even more at 0.1 V, evidencing a hindered fuel cell operation near channel outlet, caused by low oxygen concentration at cathode electrode. Such high current density gradient not only worsens performance, but could also determine inhomogeneous and aggravated components degradation.
Fig. 3.9 illustrates the reduction of cathode GDL effective diffusivity at dif-

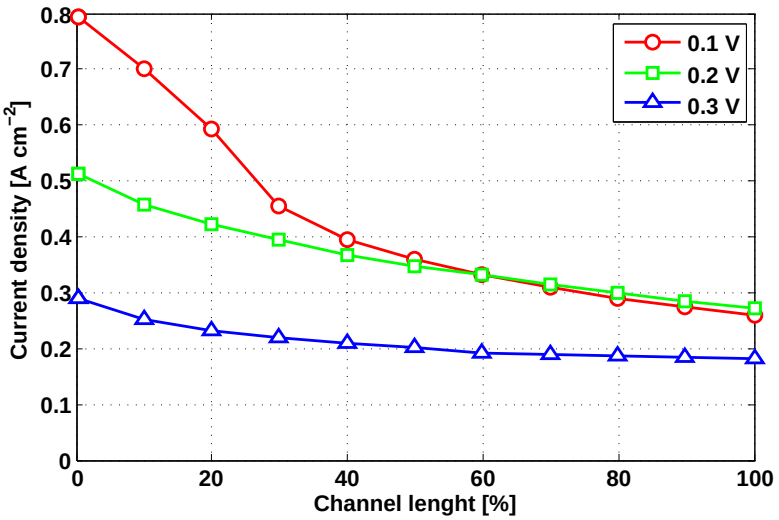

Figure 3.8: Current density profiles at different voltages (MEA GM, met 6.5%, 353 K, air 1.14 $g \cdot min^{-1}$, 1 bar).

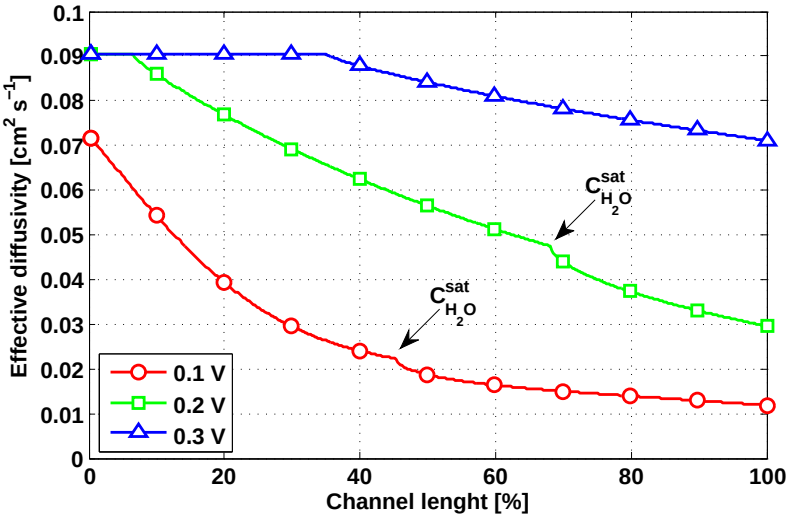

Figure 3.9: Cathode GDL + MPL effective diffusivity profiles at different voltages (MEA GM, met 6.5%, 353 K, air 1.14 $g \cdot min^{-1}$, 1 bar).

ferent voltages[4]. At 0.3 V the reduction is in the order of 20% and it is only due to liquid permeation, i.e. bulk pore obstruction. At 0.2 V the reduction is more pronounced, in agreement with the higher water production and the steeper current density profile, Fig. 3.8. In this operating condition the water concentration in the channel reaches the saturation value approximately at two-thirds of the channel and consequently the effective diffusivity presents a further reduction due to superficial pores obstruction. At 0.1 V the superficial pores obstruction occurs nearly in the middle of the channel and the overall diffusivity at channel end is reduced by one order of magnitude: in this condition the cathode GDL is severely flooded.

3.4.2 Cathode MPL influence

The model is further validated on the experimental data of the MEA GG (66 measurement points, three types of measures), Table 2.1. Two parameters, affected by the absence of cathode MPL, are calibrated. The parameters reported in Tables 3.1-3.4 remain valid, with the exception of the five parameters, related to cathode GDL, reported in Table 3.5.

B_2	$-$	$6.21 \cdot 10^2$
W_2	$-$	$2.76 \cdot 10^{-5}$
l^c_{MPL}	cm	0
l^c_{GDL}	cm	0.03
$p_{lim,GDL}$	Pa	1700 [105]

Table 3.5: Fitted and assumed parameters for model validation (MEA GG).

It is interesting to note that the fitting parameter B_2, that quantify the bulk obstruction effect, is higher than the MEA GM one, Table 3.2: the bulk obstruction effect appears more relevant without cathode MPL at constant water permeation.
The fitting parameter W_2, that characterizes the dependence of $C^{m,c,L}_{H_2O}$ on capillary pressure, is higher compared to MEA GM one, Table 3.3: the lower GDL hydrophobicity implies a lower capillary pressure at constant membrane water concentration [35]. The p_{lim} value is assumed lower according to a less hydrophobic GDL compared to MEA GM one [105].
Although the uncertainty of material characteristics and the unpredictable interactions among components, the model is able to reproduce accurately the experimental data of MEA GG, Fig. 3.10.

[4]The GDL + MPL effective diffusivity is calculated with Eq. 16 [95].

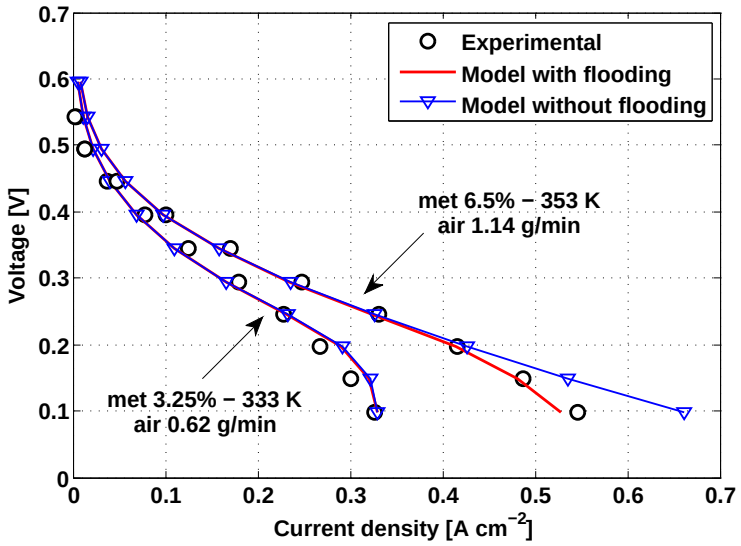

Figure 3.10: Comparison of simulated performances with and without flooding effects (MEA GG, 1 *bar*).

Moreover the model residuals are close to measurement uncertainty and the fitting parameters assume reasonable values. This result provides a further validation of both water transport and flooding proposed models.
The analysis of modeling results permits also to evaluate the cathode MPL influence. Fig. 3.10 points out the effect of flooding in two considerably different operating conditions. The behavior is similar to that reported in Fig. 3.6. At higher methanol concentration, two differences are appreciable: flooding effect magnitude increases and flooding onset occurs at lower current densities, nearly at 0.35 $A \cdot cm^{-2}$. These aspects are coherent respectively with the increase of bulk obstruction effect, B_2, and the reduction of breakthrough pressure, p_{lim}. This analysis confirms the explanation suggested discussing Fig. 2.5 and 2.7: the presence of cathode MPL increases mass transport resistance, reduces considerably water loss toward cathode channel and increases DMFC performance exclusively in case of significant GDL flooding.

3.4.3 Anode MPL influence

The model is further validated on the experimental data of MEA MM (66 measurement points, three types of measures). As already observed in the experimental analysis of paragraph 2.2.3, the presence of a high hydrophobic liquid barrier reduces water cross-over through the membrane. As a conse-

quence at the anode interface facing to the membrane it is no longer possible to assume that $C_{H_2O}^{m,a,L}$ is equal to the liquid concentration corresponding to a fully hydrated membrane (Eq. 3.7).
As reported in [45], under a condition of phase equilibrium between the water dissolved in the ionomer in the catalyst layer and the liquid water in the pores of the catalyst layer, the water content in the ionomer of the anode catalyst layer can be related to the anode void fraction[5] by:

$$\lambda^{t,a} = (1 - \varepsilon^a) \cdot \lambda_{eq}^{L} + \varepsilon^a \cdot \lambda_{eq}^{G} \tag{3.18}$$

where λ_{eq}^{L} and λ_{eq}^{G} denote the equilibrium water concentration in the ionomer when the ionomer is in phase equilibrium with the liquid water [115, 116] and water vapor saturated gas [70], respectively. Therefore the dissolved water concentration in the ionomer of the anode catalyst layer is equal to:

$$C_{H_2O}^{t,a,L} = \frac{\rho_{dry} \cdot \lambda^{t,a}}{EW} \tag{3.19}$$

where ρ_{dry} and EW denote, respectively, the density of a dry membrane and the equivalent weight of ionomer in the membrane.
As already stated in paragraph 3.1.1, the dissolved water concentration in the ionomer of the catalyst layer is different from the membrane one, $C_{H_2O}^{m,a,l}$. The strong uncertainties related to material characteristics at this interface make this concentration difficult to determine theoretically, so that an empirical approach is taken in this work. In particular a first order dependence on water concentration in the ionomer of the catalyst layer is assumed:

$$C_{H_2O}^{m,a,L} = W_5 \cdot C_{H_2O}^{t,a,L} \tag{3.20}$$

where W_5 is calibrated over experimental data.
The above discussed modifications have been introduced in the model and the calibration parameters, reported in Table 3.6, have reasonable values.

I_1	$cm^2 \cdot s^{-1}$	$8.29 \cdot 10^{-3}$
W_4	–	2.9
W_5	–	0.5

Table 3.6: Fitted parameters for model validation (MEA MM).

Methanol gas diffusivity is consistent with the values of the experimental

[5] In [71] the anode void fraction is assumed constant within diffusion and catalyst layers thickness.

characterization reported in [95]; because of the presence of the MPL the resulting value of $D^{a,G}_{GDL,CH_3OH}$ is minor than that reported in Table 3.1. The electro-osmotic drag coefficient has a considerable variability in the literature [104] and its value can increase considerably when methanol is present: the resulting value of 2.9 [5], lower than that reported in Table 3.3, is coherent with a reduced methanol concentration [114]. For the calibration parameter W_5 there is no reference for comparison in the literature; however $C^{m,a,L}_{H_2O}$ is always included between 0.055 and 0.025 $mol \cdot cm^{-3}$: these values correspond to a fully hydrated membrane and a membrane with a water content of 14, respectively.
The model is able to reproduce experimental observations with high accuracy, Fig. 3.11 and 3.12. Methanol cross-over simulations are in full agreement with experimental data; as reported in Fig. 2.6 and 2.9 the methanol cross-

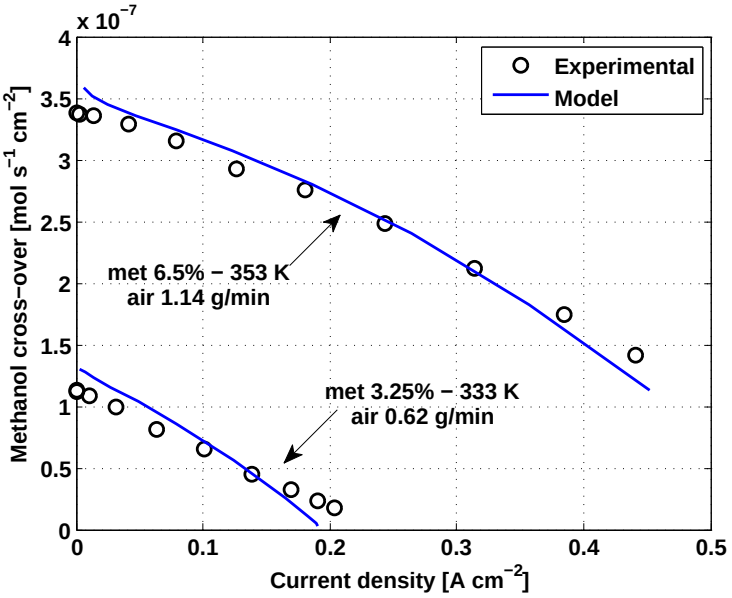

Figure 3.11: Comparison of the simulated and measured methanol cross-over fluxes (MEA MM, 1 *bar*).

over behavior is the same for different configurations of diffusion layers, only the magnitude is different. Therefore the developed model confirms that methanol cross-over is mainly due to two different contributions: liquid diffusion and electro-osmotic drag. The former is predominant at low current density, when high methanol concentration is present, the latter increases with the current density. However, in the most of the investigated operating conditions the magnitude of methanol liquid diffusion is more relevant than the electro-osmotic one.

In Fig. 3.12 the model overestimates cathode outlet water flow at 353 K, but the trend is the same: a re-calibration of cathode diffusivity at 353 K would be necessary to improve model accuracy, but it is not the aim of this paragraph.

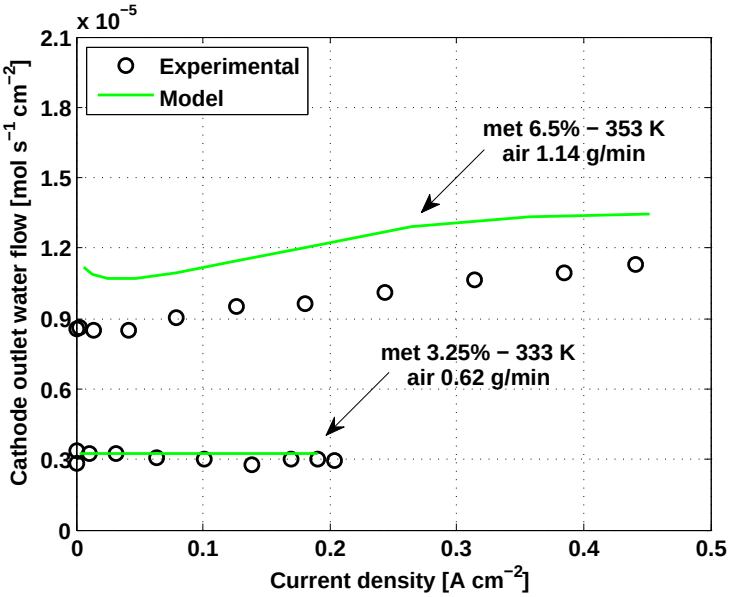

Figure 3.12: Comparison of the simulated and measured water fluxes at cathode outlet (MEA MM, 1 *bar*).

Fig. 3.13 illustrates the water fluxes through the GDL at different current densities, in the same operating condition of Fig. 3.4. It is evident that liquid permeation does not occur and the only mechanism regulating water transport through cathode GDL is gas diffusion, as expected from the experimental analysis in paragraph 2.2.3. Moreover gas diffusion slightly increases with the current density: this implies an increase of water concentration in the electrode, that at low current density is not close to the saturation value. Comparing the water fluxes through the membrane of MEA MM (Fig. 3.14) with those of MEA GM (Fig. 3.5), the main difference concerns the liquid diffusion flux. The presence of anode MPL entails a reduction of $C_{H_2O}^{m,a,L}$; as a consequence there is an inversion of liquid diffusion flux, that is directed from the cathode to the anode for current densities higher than 0.3 $A \cdot cm^{-2}$. In the literature the magnitude and direction of diffusion flux are controversial [102, 103]; the developed model, that has been validated on three types of measure at the same time, provides a further insight into the understanding of the basic principles regulating water diffusion through the membrane.

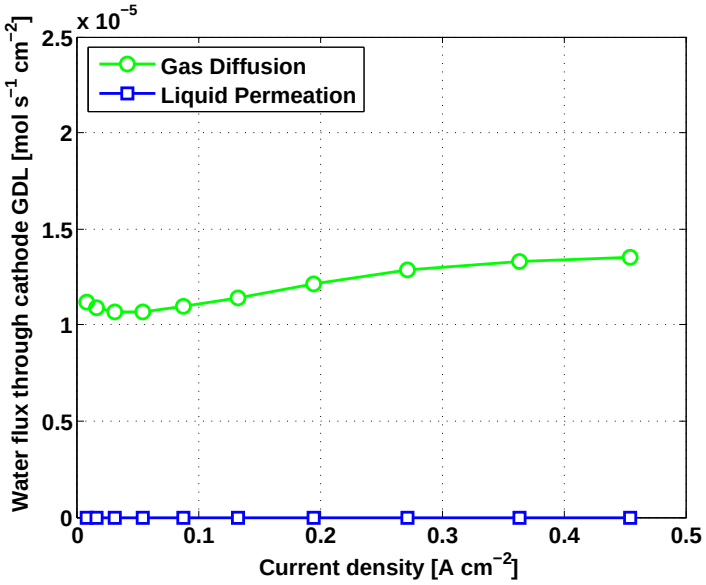

Figure 3.13: Water fluxes through cathode GDL (MEA MM, met 6.5%, 353 K, air 1.14 $g \cdot min^{-1}$, 1 bar).

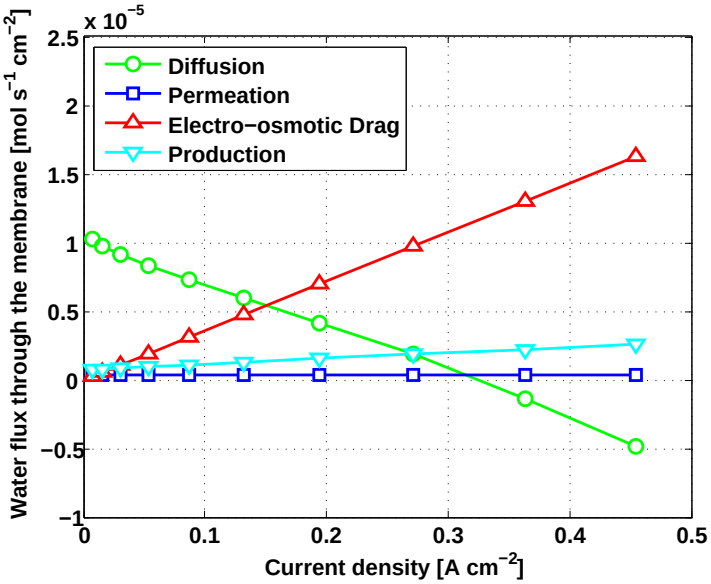

Figure 3.14: Water fluxes through the membrane (MEA MM, met 6.5%, 353 K, air 1.14 $g \cdot min^{-1}$, 1 bar).

3.5 Remarks

The developed model, that has been validated on three different typologies of measure at the same time over a wide range of operating conditions, provides an exhaustive interpretation of the mechanisms that regulate water transport and flooding phenomena. This triple calibration constitutes an innovative aspect in DMFC modeling: in the literature more detailed models can be found [64, 67, 69], but none of them is calibrated on different typologies of measure, considering such a wide range of operating conditions. This approach permits to provide an accurate estimation of local fluxes and concentrations and moreover the calibration on water transport measurements is of fundamental importance to correctly quantify the flooding effects.
The main conclusions on these phenomena are the following:

- Water diffusion through cathode GDL is regulated by vapor concentration gradient; in the most of operating conditions of MEA GM and MEA GG the vapor concentration in the electrode is close to saturation value, in agreement with a highly hydrated membrane. Instead in MEA MM the vapor concentration in the electrode is lower than the saturation value, coherently with a reduced water cross-over flux, due to the presence of a liquid water barrier to the anode (i.e., the MPL).

- Liquid water permeation through cathode GDL occurs when water pressure exceeds a threshold value, related to GDL characteristics; the permeation linear trend with current density is due to electro-osmotic drag and water production at cathode electrode. In MEA MM liquid permeation through cathode GDL does not occur due to the reduced water cross-over.

- Liquid water diffusion through the membrane in MEA GM and GG is directed from anode to cathode; at low current densities it is the predominant water transport mechanism. Instead in MEA MM there is an inversion of liquid diffusion flux at high current densities; however the water cross-over flux is still directed from anode to cathode.

- Liquid permeation through the membrane is directed from cathode to anode, but its contribution to water cross-over is negligible.

- To reproduce the effects of cathode GDL flooding, two mechanisms have to be considered simultaneously, giving comparable contributions: superficial and bulk pore obstructions. The first is proportional to liquid water concentration in cathode channel; the latter is proportional to liquid water permeation.

- A correlation to reproduce bulk pore obstruction is proposed for two cathode GDLs, with and without MPL; the magnitude of bulk obstruction effect is more relevant without cathode MPL (MEA GG).
- The addition of the MPL on cathode GDL increases the mass transfer resistance, causing a general reduction of water transport through cathode GDL (MEA GM). The performance decreases due to lower oxygen concentration when no flooding occurs, while performance increases with severe flooding, because the MPL limits its effect.
- Methanol cross-over is mainly due to two different contributions: liquid diffusion and electro-osmotic drag. The former is predominant at low current density, while the latter increases with the current density.

The proposed combined experimental and modeling analysis provides an exhaustive characterization of DMFC operation. Furthermore it is the starting point to delve into the interaction between all the physicochemical phenomena of DMFC, that are characterized by EIS measurements.

Chapter 4

EIS: systematic experimental analysis

A systematic experimental analysis of DMFC impedance spectroscopy is reported in this chapter. The aim of this anlysis is to elucidate the main relevant phenomena governing DMFC impedance behavior, in order to provide an insight into the development of innovative mathematical models for a quantitative interpretation of experimental observations

4.1 Electrochemical impedance spectroscopy in DMFC

The Electrochemical Impedance Spectroscopy is a powerful *in-situ* measurement technique that permits to evaluate the kinetic and transport phenomena of an electrochemical system [61]. It consists in perturbing the fuel cell operation with a small AC current signal over a wide range of frequencies and in measuring the voltage response. The module and the phase shift between voltage response and current perturbation are due to the electrical impedance of the fuel cell. According to the frequency of the AC current signal, different physical phenomena are excited depending on their typical time scale: the membrane responds at very high frequencies, while electrochemical reactions and mass transport phenomena are excited at medium-high and low frequen-

cies, respectively. This will originate changes in the impedance module and phase giving useful information on the entity of internal fuel cell losses [117]. Despite the potentialities of this measurement technique the interpretation of experimental observations is very complex. In the literature it has mostly been carried out on the base of equivalent circuit method [77, 78, 79, 80]: even though simple and fast, this method is not reliable, since the equivalent circuit is not unique. Moreover the DMFC anode sluggish kinetic makes the interpretation of impedance spectra more difficult. In fact in hydrogen-air fuel cells, contributions of the anode are usually negligible due to fast kinetics of hydrogen oxidation reaction and a standard practice consists in neglecting anode impedance. In DMFC the slow methanol electro-oxidation does not permit to clearly distinguish anode and cathode contributions by measuring the full fuel cell impedances. An example is reported in Fig. 4.1: the contributions of anode and cathode are superimposed and the resulting shape of impedance spectrum is almost one ideal semicircle.

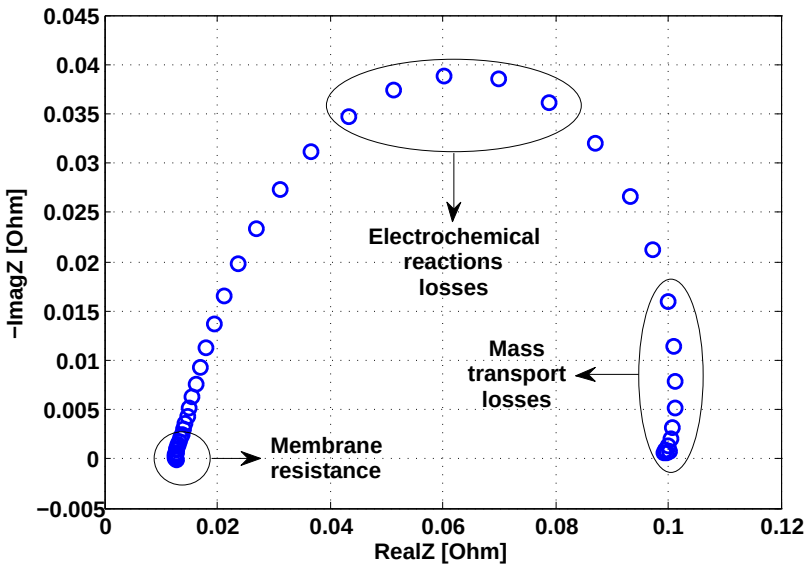

Figure 4.1: Full DMFC EIS at 0.075 $A \cdot cm^{-2}$ (MEA GM, met 3.25% - 1 $g \cdot min^{-1}$, 333 K, air 0.62 $g \cdot min^{-1}$, 1 bar).

However it is possible to eliminate contributions of the cathode in a half-cell DMFC by feeding the cathode with hydrogen, so that protons are reduced and hydrogen is evolved [118, 119, 120, 121]. In this configuration the cathode works as a dynamic hydrogen electrode and it is suitable as a reference and counter electrode for DMFC anode measurements. Then the cathode impedance is extracted by subtracting the anode impedance from the full fuel cell impedance. This experimental approach is not widely spread in

the literature, where only the full fuel cell impedance is usually measured [49, 122].
In order to elucidate the main physical phenomena governing impedance behavior, in this chapter a systematic experimental analysis of both anode and cathode EIS is performed as described above, varying operating conditions and anode GDL configuration. All the impedances are measured under galvanostatic control and the amplitude of the sinusoidal current signal is adjusted so that the potential amplitude does not exceed 10 mV. The impedance is measured at frequency included between 20 kHz and 50 mHz with a logarithmic distribution. The obtained experimental values are processed by a retrospective use of Kramers-Kronig transforms [61, 123] in order to verify the validity of the measurements. The impedance values that do not satisfy such relations are not considered meaningful.

4.2 Anode impedance

This paragraph highlights the effects of operating conditions and GDL configuration on anode impedance behavior. The DMFC operates in half-cell configuration with a cathode hydrogen flow rate of 0.0024 $Nl \cdot min^{-1}$.

4.2.1 Effect of current density

Fig. 4.2 reports two anode EIS performed on the MEA GM at two different current densities. The shape of the anode impedance is considerable different from the full fuel cell one (Fig. 4.1) and it is easier to elucidate the effect of some physical phenomena on impedance features. In fact the anode impedance is an elongated semicircle: this is partially due to proton transport losses in the electrode, that manifest themselves as a almost 45° linear branch at high frequencies, Fig. 4.2. At high-medium frequencies it is evident the effect of the current induced by the charging-discharging of the electrical double layer, that is formed at the anode-membrane interface during voltage perturbations. Instead in the full fuel cell impedance is not possible to clearly separate the contributions of the current densities associated with the capacitive charging of each electrode. With the growth of the cell current, the total resistance decreases, coherently with the results reported in the literature [119].
However varying the operating current density, two relevant differences are appreciable in the low frequency region. At 0.075 $A \cdot cm^{-2}$ an inductive behavior is evident: this could be due to the catalyst surface coverage by adsorbed reaction intermediates. In the literature the mechanisms of methanol

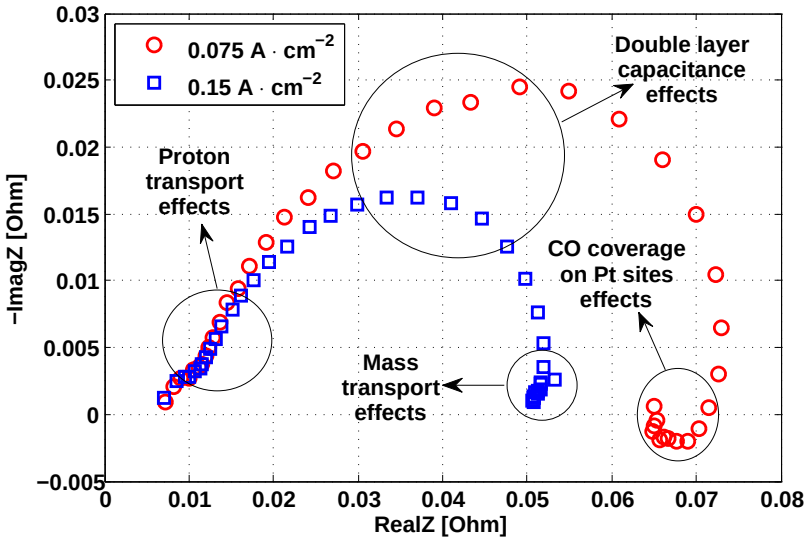

Figure 4.2: Anode EIS at different current densities (MEA GM, met 3.25% - 1 $g \cdot min^{-1}$, 333 K, 1 bar).

electro-oxidation are not fully consolidated. However the presence of carbon monoxide is widely accepted [1, 15] and therefore the inductive loop could be caused mainly by the CO coverage on platinum active sites, as already proposed in [119, 124]. Instead at 0.15 $A \cdot cm^{-2}$ the inductive behavior is no longer present, but a second arch, peculiar of mass transport limitations [125], seems to appear in the low frequencies region. This impedance feature is coherent with the increased mass transport fluxes through the GDL.
In the literature the interpretation of DMFC anode impedance is not fully consolidated and a complete understanding is still hindered by the complex and interconnected phenomena governing DMFC operation, as two-phase transport, CO_2 bubbles evolution and methanol electro-oxidation.
Anyhow, the operating current, that can be associated with the methanol concentration in the electrode, turns out to have a relevant influence on impedance behavior. In fact high current density corresponds to low methanol concentration and the impedance evidences mass transport limitations, while high methanol concentration, peculiar of lower current density, enhances the presence of adsorbed CO on active sites. For this reason further impedance measurements are performed varying the anode feeding.

4.2.2 Effect of anode feeding

The anode impedance measurements reported in this paragraph are performed on a new DMFC, manufactured by IRD® company. This fuel cell has an active area of 25 cm^2 and presents diffusion layer with MPL on both anode and cathode side (Sigracet® SGL 35 DC); for this reason it is named IRD MEA MM.
Table 4.1 reports all the investigated operating conditions. This extensive analysis aims to highlight the most influent parameters on anode impedance behavior and in this paragraph only the main relevant results are discussed.

Parameter		Values
i	$A \cdot cm^{-2}$	$0.01 \div 0.4$
T	K	338, 348
X_{CH_3OH}	$\%wt$	3.25, 6.5
$\dot{m}_{CH_3OH}$	$g \cdot min^{-1}$	1.93, 3.86

Table 4.1: Investigated operating conditions of anode impedance (IRD MEA MM).

Fig. 4.3 illustrates different anode spectra varying methanol inlet concentration and flow rate. All the recorded spectra present the high frequency

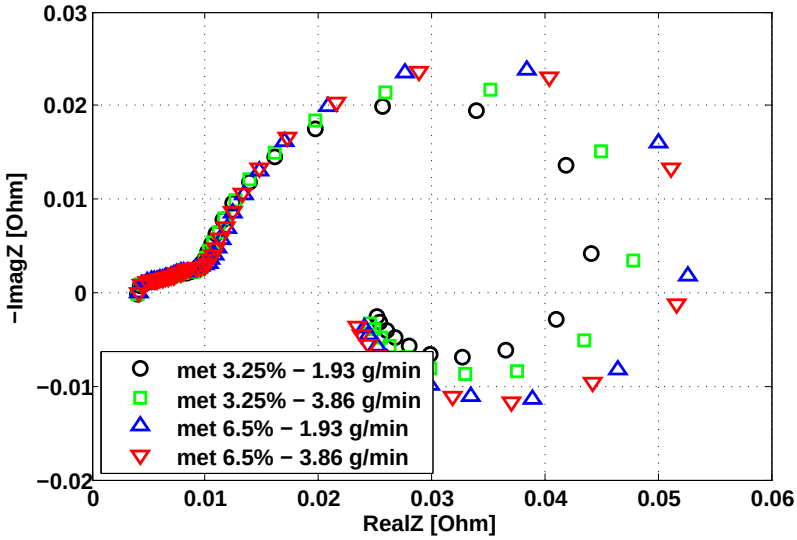

Figure 4.3: Anode EIS at 0.1 $A \cdot cm^{-2}$ (IRD MEA MM, 348 K, 1 bar).

linear branch and the inductive loop in the low frequency region. Doubling

the methanol concentration it is possible to notice a small extension of the linear branch: this could be due to a slight catalyst layer dehydration, that increases proton transport resistance. Instead the loop magnitude is strongly affected by both methanol concentration and flow rate. An increase of methanol concentration implies a larger loop, while the effect of flow rate is relevant only at low methanol concentration.
Moreover, comparing the spectra of Fig. 4.3 with those of Fig. 4.2, an enlargement of the inductive behavior is evident: this feature could be partially due to the different kinetic parameters and operating overpotential, but also the presence of anode MPL could have a relevant influence. In fact the MPL acts as a liquid water barrier to the anode catalyst layer, altering the methanol concentration in the electrode, as demonstrated in paragraph 2.2.3.
Instead at high current density, Fig. 4.4[1], low concentrations and flow rates enhance mass transport limitations, hindering the inductive loop. However doubling the methanol concentration the enlargement of inductive behavior is still evident.

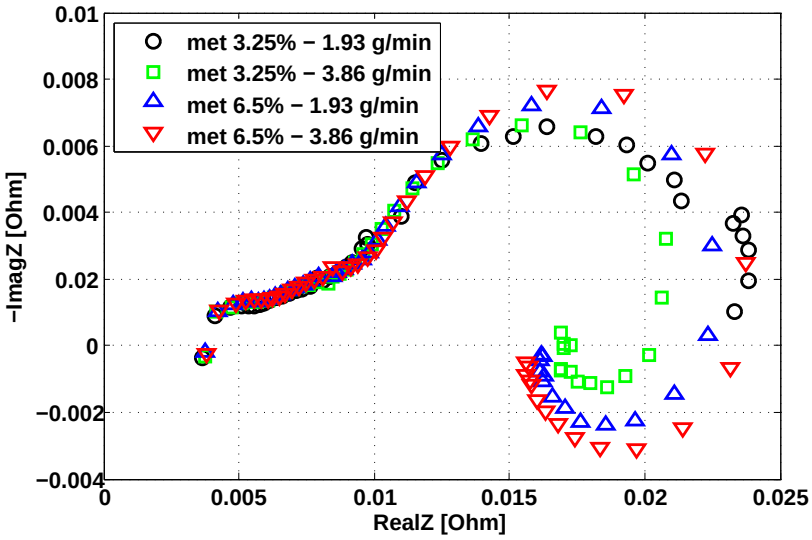

Figure 4.4: Anode EIS at 0.25 $A \cdot cm^{-2}$ (IRD MEA MM, 348 K, 1 bar).

Therefore from this systematic analysis it is possible to figure out that mass transport phenomena have a relevant influence on the magnitude and the shape of the anode impedance. In particular methanol concentration turns out to strongly affect the low frequency region: low methanol concentration enhances mass transport effects, while high methanol concentration enlarges

[1]Note that the spectra of Fig. 4.4 are evidently affected at high frequency by instrument limitations, resulting in a discontinuous behavior.

the inductive behavior. Moreover, also the presence of anode MPL, that, as explained in paragraph 2.2.3 influences mass transport through the MEA, could affect the impedance at low frequencies.
These considerations provide an insight into the development of innovative interpretation models, that should take into account a detailed description of mass transport phenomena through anode side.

4.3 Cathode impedance

The cathode EIS reported in this paragraph are obtained by subtracting the anode impedances from the corresponding full fuel cell ones [118, 124]. However the anode and full fuel cell impedance are not recorded simultaneously: the resulting cathode spectra are often affected by errors [125] and the retrospective use of Kramers-Kronig transforms eliminates some measurement points. Therefore, also the full fuel cell impedances are presented for the sake of completeness.

4.3.1 Effect of current density

The full fuel cell and the cathode impedances, corresponding to the two anode spectra of Fig. 4.2, are reported in Fig. 4.5 and 4.6, respectively. In

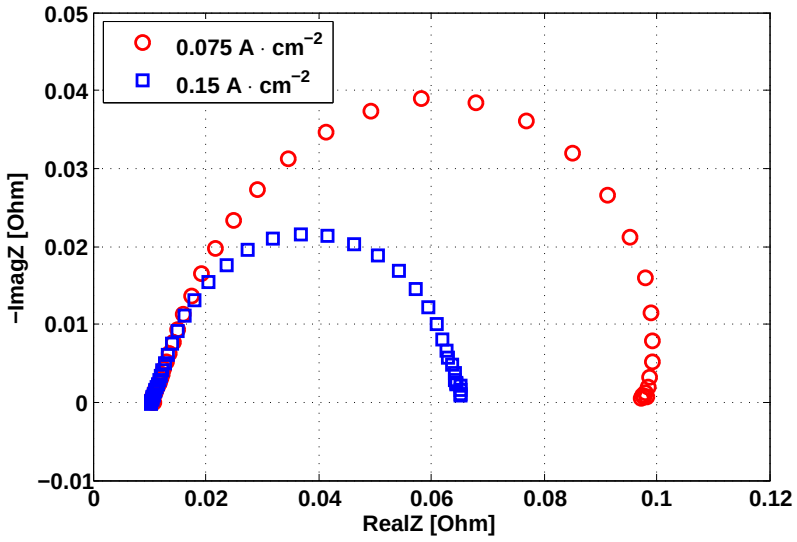

Figure 4.5: Full DMFC EIS at different current densities (MEA GM, met 3.25% - 1 $g \cdot min^{-1}$, 333 K, air 0.62 $g \cdot min^{-1}$, 1 bar).

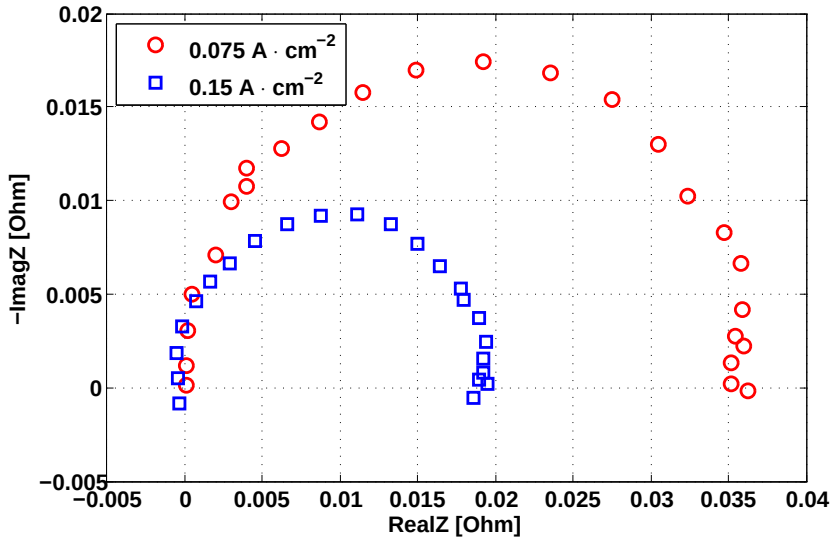

Figure 4.6: Cathode EIS at different current densities (MEA GM, met 3.25% - 1 $g \cdot min^{-1}$, 333 K, air 0.62 $g \cdot min^{-1}$, 1 bar).

Fig. 4.5 the contributions of anode and cathode are almost superimposed and therefore it is not possible to distinguish cathode losses.
Instead the cathode spectra of Fig. 4.6 are almost an ideal semicircle: this implies that mass transport limitations have a minor effect, even at 0.15 $A \cdot cm^{-2}$. Moreover in the cathode spectra there is no effect of proton transport limitations in the electrode: the absence of the linear branch could be due to the reduced thickness and the different electrode morphology.
The recorded cathode spectra are coherent with those reported in the literature [118, 124]: in fact the total resistance decreases with increasing current density. However several studies show the presence of a low frequency second arch [120, 125], peculiar of mass transport limitations. In order to verify the onset of this second arch, further measurements are carried out varying both anode and cathode feeding.

4.3.2 Effect of anode and cathode feeding

The cathode impedance measurements reported in this paragraph are performed on the IRD MEA MM; the corresponding anode spectra have been previously discussed in paragraph 4.2.2. Table 4.2 reports all the investigated operating conditions and once again only the main relevant results are presented.
Fig. 4.7 illustrates different full fuel cell impedances at 0.1 $A \cdot cm^{-2}$ with

Parameter		Values
i	$A \cdot cm^{-2}$	$0.01 \div 0.4$
T	K	338, 348
X_{CH_3OH}	$\%wt$	3.25, 6.5
$\dot{m}_{CH_3OH}$	$g \cdot min^{-1}$	1.93, 3.86
$\dot{m}_{air}$	$g \cdot min^{-1}$	0.43, 0.86

Table 4.2: Investigated operating conditions of cathode impedance (IRD MEA MM).

a constant cathode flow rate. These measurements are coherent with the anode ones of Fig. 4.3: in fact the shape is similar, modified by the presence of a second circle at medium-high frequency related to the cathode electrode. The inductive loop is still present, as well as its dependence on methanol concentration, confirming the considerable contribution of anode to the overall impedance.

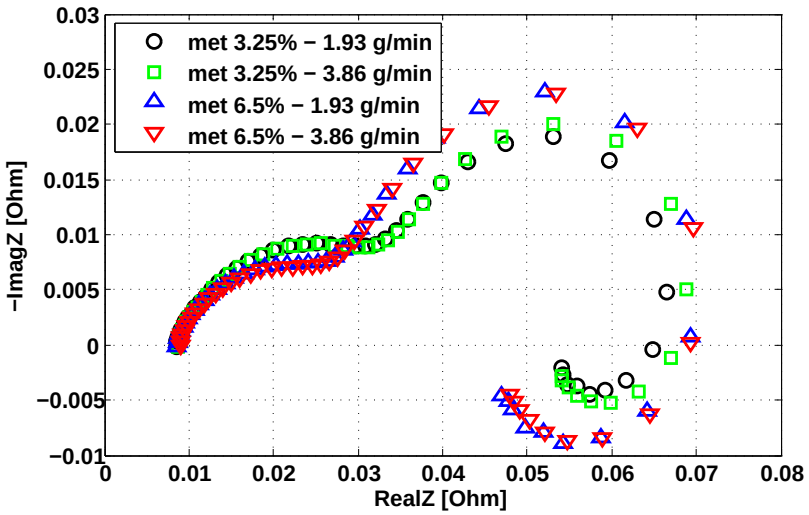

Figure 4.7: Full DMFC EIS at 0.1 $A \cdot cm^{-2}$ (IRD MEA MM, 348 K, air 0.86 $g \cdot min^{-1}$, 1 bar).

Fig. 4.8 reports the calculated cathode spectra. Considering that the corresponding anode spectra present almost the same total resistance (Fig. 4.3), the obtained cathode measurements are coherent with the slope of polarization curves (Fig. 4.9): in fact the higher the slope of polarization curve, the greater the total resistance.
The shape of the spectra is a slightly elongated semicircle, but a second arch

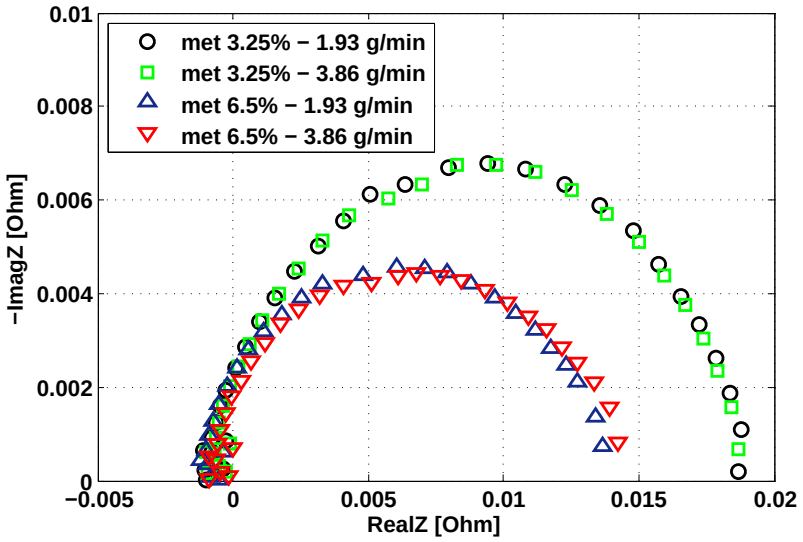

Figure 4.8: Cathode EIS at 0.1 $A \cdot cm^{-2}$ (IRD MEA MM, 348 K, air 0.86 $g \cdot min^{-1}$, 1 bar).

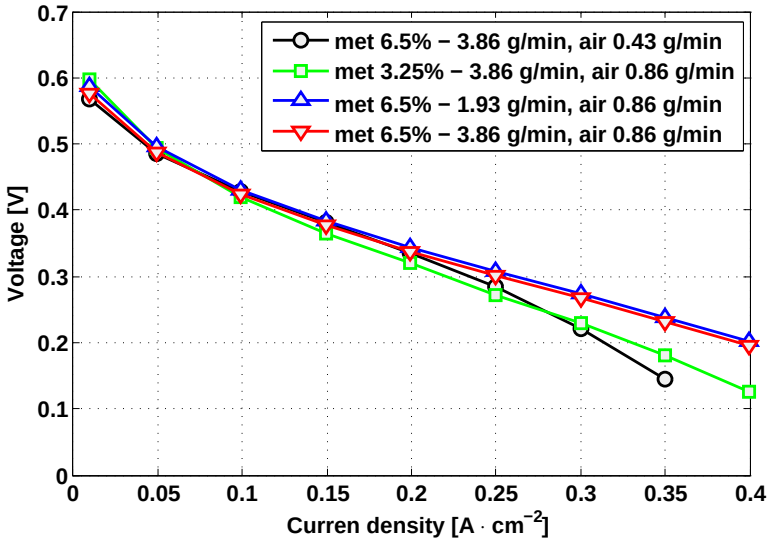

Figure 4.9: Polarization curves (IRD MEA MM, 348 K, 1 bar).

is still not evident. However it is possible to notice that the anode flow rate have a limited influence on the spectra, while high methanol concentrations reduce the total resistance.
Fig. 4.10 illustrates different full fuel cell spectra at 0.25 $A \cdot cm^{-2}$ with a constant anode flow rate, that does not influence cathode impedance behavior (Fig. 4.8).

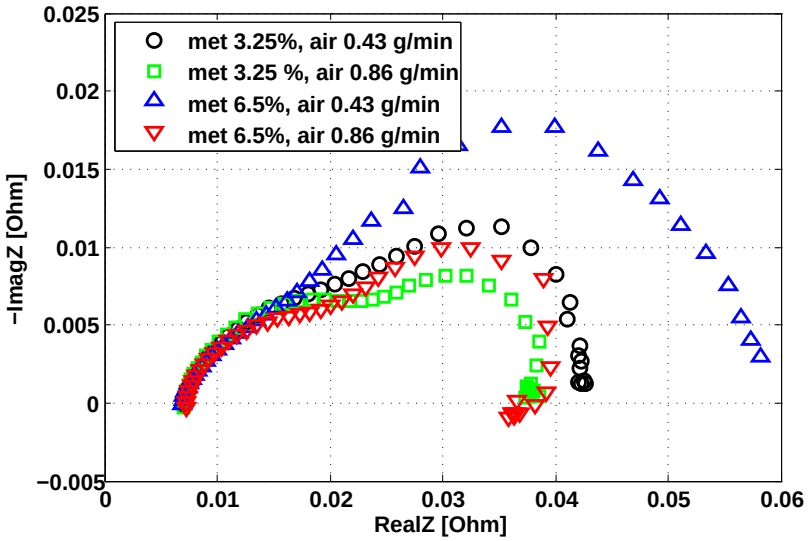

Figure 4.10: Full DMFC EIS at 0.25 $A \cdot cm^{-2}$ (IRD MEA MM, met 3.86 $g \cdot min^{-1}$, 348 K, 1 bar).

The spectra features are different from those reported in Fig. 4.7: at higher current density the inductive loop is not anymore present, while mass transport effects appear in the low frequency region, especially at high methanol concentration and low cathode flow rate. However these mass transport limitations do not manifest themselves as a clear additional arch.
Instead analyzing the corresponding cathode spectra, reported in Fig. 4.11, the mass transport limitations are now evident in all the operating conditions: the second arch is present in the low frequency region and lowering cathode flow rate its magnitude increases. This effect is amplified by an increment of methanol concentration: in fact the associated increment of methanol crossover, Fig. 4.12, implies an enhanced oxygen consumption for methanol oxidation at the cathode electrode as well as a reduced oxygen concentration. In agreement with such interpretation, an increment of airflow rate, that guarantees higher oxygen availability, re-establish a spectrum without a so evident mass transport limitation at low frequency.
The relevant difference between the total resistances of the cathode spectra

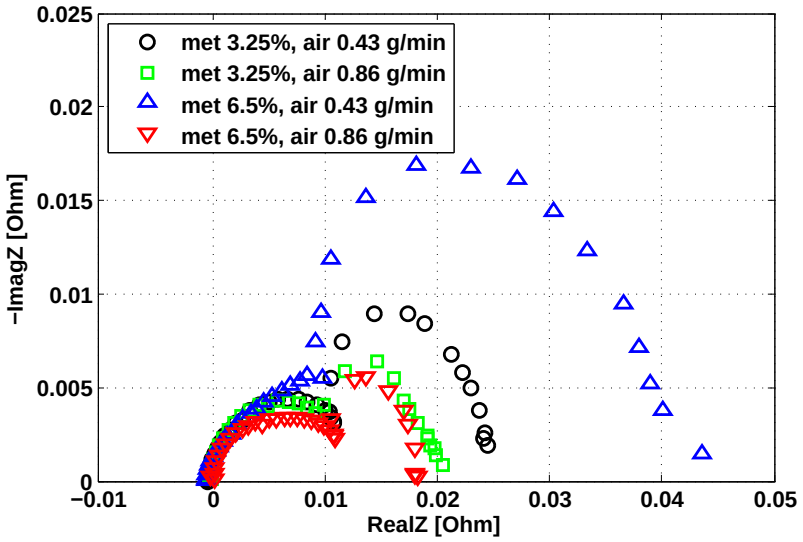

Figure 4.11: Cathode EIS at 0.25 $A{\cdot}cm^{-2}$ (IRD MEA MM, met 3.86 $g{\cdot}min^{-1}$, 348 K, 1 bar).

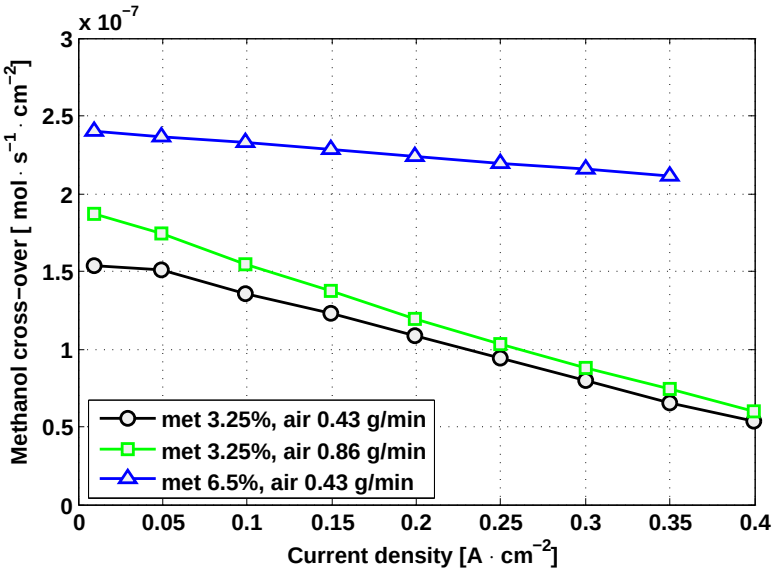

Figure 4.12: Methanol cross-over (IRD MEA MM, met 3.86 $g \cdot min^{-1}$, 348 K, 1 bar).

at high methanol concentration is also confirmed by the slope of the corresponding polarization curves, reported in Fig. 4.9.
The cathode spectra reported in this paragraph are coherent with the expectations: mass transport limitations are enhanced by high current density, reduced cathode flow rate and increased methanol cross-over.

4.4 Remarks

A systematic experimental analysis of anode and cathode impedance has been carried out, in order to elucidate the main relevant phenomena governing impedance behavior and to provide an insight into the development of phenomenological models. The following considerations can be pointed out:

- The high frequency linear branch, due to proton transport limitations through the catalyst layer, is evident in the anode impedance, but not in the cathode one. Therefore these losses have to be considered only in the modeling of anode impedance.
- Anode impedance often presents an inductive loop and thus a methanol oxidation reaction dependent also on surface coverage by an absorbed intermediate has to be introduced in the anode impedance model.
- The magnitude of inductive loop is strongly influenced by methanol concentration in the electrode and probably also by the presence of anode MPL. Moreover the inductive behavior disappears when mass transport limitations occur, usually at high current density and low methanol concentration. Therefore in the anode impedance modeling particular attention has to be focused on mass transport phenomena regulating methanol concentration in the electrode.
- The cathode spectra are often an almost ideal or slightly elongated semicircle, in which mass transport limitations are not evident. However at high current density and low cathode flow rate a second arch appears and it is considerably enlarged by increased methanol cross-over. Therefore in the cathode impedance modeling the effect of methanol cross-over, that reduces oxygen concentration in the electrode, has to be considered.

Chapter 5

EIS: preliminary model development

The preliminary modeling approach described in this chapter consists in expressing the equivalent circuit elements as a function of the physical parameters of the cell, obtained from the validation of the previous 1D+1D steady-state model.

5.1 Model development: basic principles

The basic principles of the modeling approach described in this chapter was proposed by Orazem in [81]. This is the first utilized approach because it can be easily integrated in the previous 1D+1D DMFC model; moreover it has not yet been used for the interpretation of DMFC impedance spectra.
Generally speaking, the current density corresponding to an electrochemical reaction can be expressed as a function of the interfacial potential[1], the surface concentrations and the surface coverage of the absorbed intermediates:

$$i = f\left(\eta, C_i, \gamma_j\right) \tag{5.1}$$

[1]The interfacial potential is the difference between the potential of the electrode and the potential in the electrolyte adjacent to the electrode, measured with respect to the same reference electrode.

When a small amplitude sinusoidal current $\tilde{i}$ is added to the current density, the concentrations of species, the surface coverage of the absorbed intermediates and the interfacial potential are also modulated in a sinusoidal way around their steady state values:

$$\begin{aligned} i &= i_{steady} + Re\{\tilde{i} \cdot e^{j\cdot\omega\cdot t}\} \\ \eta &= \eta_{steady} + Re\{\tilde{\eta} \cdot e^{j\cdot\omega\cdot t}\} \\ C_i &= C_{i,steady} + Re\{\tilde{C}_i \cdot e^{j\cdot\omega\cdot t}\} \\ \gamma_j &= \gamma_{j,steady} + Re\{\tilde{\gamma}_j \cdot e^{j\cdot\omega\cdot t}\} \end{aligned} \tag{5.2}$$

The impedance of the electrode is therefore given by the ratio between the oscillating components of interfacial potential and current at the interface of the electrode facing to the membrane[2]:

$$Z = \left.\frac{\tilde{\eta}}{\tilde{i}}\right|_m \tag{5.3}$$

The oscillating current can be expressed as a Taylor series expansion about the steady-state values:

$$\tilde{i} = \left.\frac{\partial i}{\partial \eta}\right|_{steady} \cdot \tilde{\eta} + \sum_i \left.\frac{\partial i}{\partial C_i}\right|_{steady} \cdot \tilde{C}_i + \sum_j \left.\frac{\partial i}{\partial \gamma_j}\right|_{steady} \cdot \tilde{\gamma}_j \tag{5.4}$$

where $\tilde{\eta}$, $\tilde{C}_i$, $\tilde{\gamma}_j$ are assumed to have a small magnitude such that the higher order terms can be neglected. Oscillations of interfacial potential, concentration and surface coverage are associated with different physical phenomena and in the equivalent electric circuit they are respectively represented by a charge transfer resistance, a mass transfer impedance and an inductance in series with a resistance.
Substituting Eq. 5.4 in Eq. 5.3 and relating the oscillations of concentration $\tilde{C}_i$ and surface coverage $\tilde{\gamma}_j$ to the oscillating potential $\tilde{\eta}$ or current density $\tilde{i}$, it is possible to obtain an analytic expression of equivalent circuit elements as a function of the physical parameters of the system [81]. In the following paragraphs the mathematical expression of each equivalent circuit element is reported for a general electrochemical reaction.

5.1.1 Charge transfer resistance

Considering an electrochemical reaction dependent only on potential, the steady-state Faradaic current associated with this reaction can be expressed

[2]The total impedance of the fuel cell is given by the sum of membrane resistance and anode and cathode impedances.

in terms of Tafel kinetic as:

$$i = i_* \cdot exp\,(\eta/b) \tag{5.5}$$

where i_* is the exchange current density and b is the Tafel slope. Under the assumption that the reaction is not influenced by the concentration of the reactants and the presence of adsorbed intermediates, the oscillating component of the current density can be expressed as:

$$\tilde{i} = \left.\frac{\partial i}{\partial \eta}\right|_{steady} \cdot \tilde{\eta} \tag{5.6}$$

The steady-state derivative of the current density with respect to the potential is equal to:

$$\left.\frac{\partial i}{\partial \eta}\right|_{steady} = i_* \cdot exp\,(\eta/b) \cdot \frac{1}{b} \tag{5.7}$$

and therefore the oscillating current density results:

$$\tilde{i} = i_* \cdot exp\,(\eta/b) \cdot \frac{1}{b} \cdot \tilde{\eta} \tag{5.8}$$

Substituting Eq. 5.8 in the definition of the impedance, Eq. 5.3, the oscillations of interfacial potential cancel out and in the equivalent electric circuit a reaction dependent only on potential can be represented by a unique charge transfer resistance, that is defined in terms of kinetic parameters as:

$$R_{ct} = \frac{\tilde{\eta} \cdot b}{i_* \cdot exp\,(\eta/b) \cdot \tilde{\eta}} = \frac{b}{i} \tag{5.9}$$

5.1.2 Mass transfer impedance

Considering a reaction dependent on potential and concentration, the steady-state Faradaic current associated with this reaction can be expressed in terms of Tafel kinetic as:

$$i = i_* \cdot \frac{C_{el}}{C_{ref}} \cdot exp\,(\eta/b) \tag{5.10}$$

In this case, the oscillating component of the current density can be expressed as:

$$\tilde{i} = i_* \cdot \frac{C_{el}}{C_{ref}} \cdot exp\,(\eta/b) \cdot \frac{1}{b} \cdot \tilde{\eta} + \frac{i_*}{C_{ref}} \cdot exp\,(\eta/b) \cdot \tilde{C}_{el} \tag{5.11}$$

where $\tilde{C}_{el}$ is the oscillating component of the concentration evaluated at the electrode surface.

An additional relation is needed in order to evaluate the oscillating component of the concentration with respect to the oscillating component of the current density. The mass transport process through a diffusion media can be described by the Fick's law of diffusion, that in terms of oscillating components is equal to:

$$\tilde{\tilde{i}} = n \cdot F \cdot D \cdot \frac{\partial \tilde{C}}{\partial y} \tag{5.12}$$

where n is the number of electrons exchanged in the reaction, F is the Farady's constant, D is the diffusivity of the reactant and y is the direction of the diffusion process. Eq. 5.12 in terms of dimensionless position $\zeta = y/\delta$ and concentration $\Theta_{el} = \tilde{C}/\tilde{C}_{el}$ takes the form:

$$\tilde{\tilde{i}} = n \cdot F \cdot D \cdot \frac{\tilde{C}_{el}}{\delta} \cdot \Theta'_{el} \tag{5.13}$$

where δ is the characteristic length of the diffusion process and Θ'_{el} is the derivative of dimensionless concentration at the electrode with respect to the dimensionless position δ.
From Eq. 5.13 it is possible to obtain an expression of $\tilde{C}_{el}$ as a function of $\tilde{\tilde{i}}$, that, after substituting in Eq. 5.11, leads to the following relation:

$$i_* \cdot \frac{C_{el}}{C_{ref}} \cdot exp\,(\eta/b) \cdot \frac{1}{b} \cdot \tilde{\eta} = \tilde{\tilde{i}} \cdot \left(1 - \frac{i_*}{C_{ref}} \cdot exp\,(\eta/b) \cdot \frac{\delta}{n \cdot F \cdot D \cdot \Theta'_{el}}\right) \tag{5.14}$$

The impedance is given by the ratio between the oscillating components of the potential and the current and therefore it is equal to:

$$Z = \frac{\tilde{\eta}}{\tilde{\tilde{i}}} = \frac{1 - \dfrac{i_*}{C_{ref}} \cdot exp\,(\eta/b) \cdot \dfrac{\delta}{n \cdot F \cdot D \cdot \Theta'_{el}}}{i_* \cdot \dfrac{C_{el}}{C_{ref}} \cdot exp\,(\eta/b) \cdot \dfrac{1}{b}} \tag{5.15}$$

The first term in the right end side of Eq. 5.15 corresponds to the expression of the charge transfer resistance obtained in Eq. 5.9, in fact:

$$R_{ct} = \frac{1}{i_* \cdot \dfrac{C_{el}}{C_{ref}} \cdot exp\,(\eta/b) \cdot \dfrac{1}{b}} = \frac{b}{i} \tag{5.16}$$

while the second term represents the mass transfer impedance:

$$Z_{mt} = -\frac{\delta \cdot b}{n \cdot F \cdot D \cdot \Theta'_{el} \cdot C_{el}} \tag{5.17}$$

Under the assumption that mass transfer is through a Nernst stagnant diffusion layer [81], it is possible to obtain an analytical expression of the dimensionless concentration gradient at the electrode, that results equal to:

$$-\frac{1}{\Theta'_{el}} = \frac{tanh\sqrt{j \cdot H}}{\sqrt{j \cdot H}} \tag{5.18}$$

where

$$H = \frac{\omega \cdot \delta^2}{D} \tag{5.19}$$

is the dimensionless frequency of the diffusion process. Therefore the analytic expression of the mass transfer impedance is defined in terms of kinetic parameters as:

$$Z_{mt} = \frac{\delta \cdot b}{n \cdot F \cdot D \cdot C_{el}} \cdot \frac{tanh\sqrt{j \cdot H}}{\sqrt{j \cdot H}} \tag{5.20}$$

Therefore in the equivalent electric circuit a reaction dependent on potential and concentration can be represented by a charge transfer resistance in series with a mass transfer impedance, that are defined in terms of physical parameters by Eq. 5.16 and Eq. 5.20, respectively.

5.1.3 Surface coverage impedance

Considering a reaction dependent on potential and surface coverage of an absorbed intermediate, the hypothetical reaction mechanism can be expressed as:

$$\begin{aligned} &1. \quad R_1 \longrightarrow R_2 + n_1 e^- \\ &2. \quad R_2 \longrightarrow R_3 + n_2 e^- \end{aligned} \tag{5.21}$$

where n_1 and n_2 are the number of electrons exchanged in the first and second reaction step, respectively. The steady-state Faradaic current associated with each reaction step is equal to:

$$i_1 = i_{*1} \cdot (1 - \gamma_{R_2}) \cdot exp(\eta / b_1) \tag{5.22}$$

$$i_2 = i_{*2} \cdot \gamma_{R_2} \cdot exp(\eta / b_2) \tag{5.23}$$

and the current of the overall reaction can be expressed as the sum of Eq. 5.22 and 5.23.
The variation of the surface coverage by the reaction intermediate R_2 is given by the following expression:

$$\Gamma \cdot \frac{\partial \gamma_{R_2}}{\partial t} = \frac{i_1}{n_1 \cdot F} - \frac{i_2}{n_2 \cdot F} \tag{5.24}$$

where Γ is the active site density. In the first reaction step the intermediate R_2 is formed, while in the second step the adsorbed R_2 is consumed. In steady-state the left end side of Eq. 5.24 is equal to zero; assuming for simplicity $n_1 = n_2 = 1$ and substituting Eq. 5.22 and 5.23 into Eq. 5.24, it is possible to obtain an expression of the steady state surface coverage:

$$\gamma_{R_2} = \frac{i_{*1} \cdot exp(\eta/b_1)}{i_{*1} \cdot exp(\eta/b_1) + i_{*2} \cdot exp(\eta/b_2)} \tag{5.25}$$

The oscillating component of the current density for each reaction step is given by the Taylor series expansion about the steady-state values:

$$\tilde{i}_1 = i_{*1} \cdot (1 - \gamma_{R_2}) \cdot exp(\eta/b_1) \cdot \frac{1}{b_1} \cdot \tilde{\eta} - i_{*1} \cdot exp(\eta/b_1) \cdot \tilde{\gamma}_{R_2} \tag{5.26}$$

$$\tilde{i}_2 = i_{*2} \cdot \gamma_{R_2} \cdot exp(\eta/b_2) \cdot \frac{1}{b_2} \cdot \tilde{\eta} + i_{*2} \cdot exp(\eta/b_2) \cdot \tilde{\gamma}_{R_2} \tag{5.27}$$

and the oscillating current of the overall reaction is therefore equal to:

$$\tilde{i} = \tilde{\eta} \cdot \left[\frac{i_{*1}}{b_1} \cdot (1 - \gamma_{R_2}) \cdot e^{\frac{\eta}{b_1}} + \frac{i_{*2}}{b_2} \cdot \gamma_{R_2} \cdot e^{\frac{\eta}{b_2}} \right] + \tilde{\gamma}_{R_2} \cdot \left[-i_{*1} \cdot e^{\frac{\eta}{b_1}} + i_{*2} \cdot e^{\frac{\eta}{b_2}} \right] \tag{5.28}$$

Expressing Eq. 5.24 in terms of oscillating components and substituting Eqs. 5.26 and 5.27 in Eq. 5.24, it is possible to obtain the additional relation between the oscillating coverage and the oscillating potential:

$$\tilde{\gamma}_{R_2} = \frac{i_{*1}/b_1 \cdot (1 - \gamma_{R_2}) \cdot e^{\frac{\eta}{b_1}} - i_{*2}/b_2 \cdot \gamma_{R_2} \cdot e^{\frac{\eta}{b_2}}}{\Gamma \cdot F \cdot j \cdot \omega + i_{*1} \cdot e^{\frac{\eta}{b_1}} + i_{*2} \cdot e^{\frac{\eta}{b_2}}} \cdot \tilde{\eta} \tag{5.29}$$

Substituting Eq. 5.29 in Eq. 5.28, it is possible to express the impedance as:

$$\begin{aligned} Z^{-1} = & \left[\frac{i_{*1}}{b_1} \cdot (1 - \gamma_{R_2}) \cdot e^{\frac{\eta}{b_1}} + \frac{i_{*2}}{b_2} \cdot \gamma_{R_2} \cdot e^{\frac{\eta}{b_2}} \right] + \left[-i_{*1} \cdot e^{\frac{\eta}{b_1}} + i_{*2} \cdot e^{\frac{\eta}{b_2}} \right] \\ & \cdot \frac{i_{*1}/b_1 \cdot (1 - \gamma_{R_2}) \cdot e^{\frac{\eta}{b_1}} - i_{*2}/b_2 \cdot \gamma_{R_2} \cdot e^{\frac{\eta}{b_2}}}{\Gamma \cdot F \cdot j \cdot \omega + i_{*1} \cdot e^{\frac{\eta}{b_1}} + i_{*2} \cdot e^{\frac{\eta}{b_2}}} \end{aligned} \tag{5.30}$$

The first term in the right end side of Eq. 5.30 corresponds to the charge transfer resistance for each reaction step, that is respectively equal to:

$$R_{ct,1} = \frac{b_1}{i_{*1} \cdot (1 - \gamma_{R_2}) \cdot exp(\eta/b_1)} = \frac{b_1}{i_1} \tag{5.31}$$

$$R_{ct,2} = \frac{b_2}{i_{*1} \cdot \gamma_{R_2} \cdot exp(\eta/b_2)} = \frac{b_2}{i_2} \tag{5.32}$$

while the second term represents the impedance due to the surface coverage by the reaction intermediate. It can be rewritten as the sum of a resistance and an inductance:

$$\begin{aligned} Z_{cov} &= \frac{\Gamma \cdot F \cdot j \cdot \omega + i_{*1} \cdot e^{\frac{\eta}{b_1}} + i_{*2} \cdot e^{\frac{\eta}{b_2}}}{\left[-i_{*1} \cdot e^{\frac{\eta}{b_1}} + i_{*2} \cdot e^{\frac{\eta}{b_2}}\right] \cdot \left[i_{*1}/b_1 \cdot (1-\gamma_{R_2}) \cdot e^{\frac{\eta}{b_1}} - i_{*2}/b_2 \cdot \gamma_{R_2} \cdot e^{\frac{\eta}{b_2}}\right]} \\ &= R_{cov} + j \cdot \omega \cdot L_{cov} \end{aligned} \tag{5.33}$$

where

$$R_{cov} = \frac{i_{*1} \cdot e^{\frac{\eta}{b_1}} + i_{*2} \cdot e^{\frac{\eta}{b_2}}}{\left[-i_{*1} \cdot e^{\frac{\eta}{b_1}} + i_{*2} \cdot e^{\frac{\eta}{b_2}}\right] \cdot \left[i_{*1}/b_1 \cdot (1-\gamma_{R_2}) \cdot e^{\frac{\eta}{b_1}} - i_{*2}/b_2 \cdot \gamma_{R_2} \cdot e^{\frac{\eta}{b_2}}\right]} \tag{5.34}$$

$$L_{cov} = \frac{\Gamma \cdot F}{\left[-i_{*1} \cdot e^{\frac{\eta}{b_1}} + i_{*2} \cdot e^{\frac{\eta}{b_2}}\right] \cdot \left[i_{*1}/b_1 \cdot (1-\gamma_{R_2}) \cdot e^{\frac{\eta}{b_1}} - i_{*2}/b_2 \cdot \gamma_{R_2} \cdot e^{\frac{\eta}{b_2}}\right]} \tag{5.35}$$

Therefore in the equivalent electric circuit a reaction dependent on potential and surface coverage can be represented by the charge transfer resistance of the first reaction step in parallel with that of the second reaction step and with an inductance in series with a resistance. The impedance of the corresponding equivalent electric circuit results equal to:

$$Z = \left(\frac{1}{R_{ct,1}} + \frac{1}{R_{ct,2}} + \frac{1}{R_{cov} + j \cdot \omega \cdot L_{cov}}\right)^{-1} \tag{5.36}$$

where the values of equivalent circuit elements as a function of the physical parameters are respectively given by Eq. 5.31, 5.32, 5.34 and 5.35.

5.2 Model of cathode impedance

5.2.1 Impedance model development

Since the interpretation of the impedance related to oxygen reduction reaction is consolidated in the literature, the first electrode that has been analyzed

is the cathode. Many works report analyses on the impedance behavior of PEMFC cathode [126, 127, 128, 129, 130], while only few studies focus on DMFC [125, 131]. However, a part from the effects of methanol cross-over flux, the cathode impedance features of the two technologies are the same.
In [82], the modeling approach of paragraph 5.1 was applied to the interpretation of cathode impedance of an hydrogen-air fuel cell. However the developed model [82] is extremely simplified: the channel length and the thickness of the different layers composing the system are not considered and therefore the fuel cell is modeled in a 0-D domain. Nevertheless the aim of this simplified treatment is to explore the role of specific hypothesized reaction sequences on impedance features and not to provide a detailed and validated model of fuel cell impedance.
In this work, the approach presented in [81] has been integrated in the previous 1D+1D DMFC model [132] in order to provide a quantitative interpretation of DMFC cathode impedance. This is the first modeling approach that has been utilized because it is relatively simple to be coupled with the previous 1D+1D DMFC model: in fact also in [132] the catalyst layer behavior and mass transport are described by Tafel kinetics and Fick's law of diffusion, respectively, as required by the developed approach [81]. However, in respect to [82], the following modifications have been introduced:

- The 1D+1D DMFC model provides an estimation of DMFC physical quantities along channel length and thus it is possible to obtain a local value of equivalent circuit elements. Therefore the impedance model is not constituted by a unique equivalent circuit as in [82], but the impedance behavior is described by N equivalent circuits in parallel, where N is the number of integration steps in which the channel length has been discretized during the numerical resolution of the 1D+1D DMFC model.

- As reported in the experimental analysis (see paragraph 4.3.2), the methanol crossover flux seems to have a relevant influence on impedance behavior of DMFC cathode: a high methanol cross-over enhances oxygen consumption for methanol oxidation and manifests itself as an enlargement of the spectra in the low frequency region, especially at low cathode flow rate.
  In the DMFC 1D+1D model the methanol oxidation at the cathode has been introduced in Tafel kinetic adding the term $6 \cdot F \cdot N_{m,cross}^{CH_3OH}$ to the current density (Eq. 13 in [72]), with the intent to provide a possible description of methanol electro-oxidation at cathode side, as reported in [107]. The proposed equation assumes that methanol is

completely consumed in cathode electrode by a electrochemical reaction with oxygen, characterized by a rate determining step equal to oxygen electro-reduction. Therefore in the impedance model no additional electric circuit elements corresponding to methanol cross-over flux have been introduced, but its effect is considered in the Tafel kinetic as an increase of cathode overpotential. This affects the value of kinetic parameters and local concentrations, that are used for the calculation of the charge transfer resistance and mass transfer impedance of oxygen reduction reaction.

Moreover the previous 1D+1D DMFC model has been validated on three different typologies of measures at the same time over a wide range of operating conditions; therefore the predicted values of all the interested physical quantities are reliable. In particular the water transport and methanol cross-over parameters have been calibrated over the corresponding experimental measures, while both anode and cathode kinetic parameters have been calibrated with respect to polarization curves. In the development of DMFC cathode impedance one additional experimental measure has been added to the validation procedure: the anodic polarization. In fact, as will be discussed later, the anode kinetic parameters are calibrated over the anodic polarization, while the cathode ones are calibrated with respect to the polarization curve, increasing the reliability of the results.
As widely accepted in fuel cell modeling [128], the oxygen reduction reaction can be described by a reaction dependent on potential and concentration. Therefore the equivalent electric circuit utilized for the simulation is the following [81]:

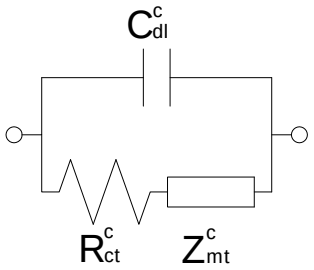

Figure 5.1: Cathode equivalent electric circuit.

It is constituted by a capacitance in parallel with a charge transfer resistance in series with a mass transfer impedance. According to the methodology presented in paragraph 5.1.2 and the nomenclature of the 1D+1D DMFC model [132], the value of the charge transfer resistance and mass transfer

impedance are respectively equal to:

$$R_{ct}^{c} = \frac{b^{c}}{i} \tag{5.37}$$

$$Z_{mt}^{c} = \frac{l_{GDL}^{c} \cdot b^{c}}{4 \cdot F \cdot D_{GDL,O_2}^{c} \cdot C_{O_2}^{t,c}} \cdot \frac{tanh\sqrt{j \cdot H}}{\sqrt{j \cdot H}} \tag{5.38}$$

where i is the local current density and $C_{O_2}^{t,c}$ is the local oxygen concentration at the cathode catalyst layer. Instead, the value of the double layer capacitance, that is assumed constant along the channel length, is fitted over experimental impedance data.
All the local circuit describing cathode impedance features are in parallel and therefore the global value of the DMFC cathode impedance is calculated with the following relation:

$$Z_{tot}^{c} = \left(\sum_{i=1}^{N} \frac{1}{Z_{tot,i}^{c}} \right)^{-1} \tag{5.39}$$

where $Z_{tot,i}^{c}$ is the total impedance of each local circuit element, that is equal to:

$$Z_{tot,i}^{c} = \frac{1}{\left(R_{ct}^{c} + Z_{mt}^{c}\right)^{-1} + j \cdot \omega \cdot C_{dl}^{c}} \tag{5.40}$$

5.2.2 Modeling results

In order to increase the accuracy and the reliability of the results, the cathode kinetic parameters of the 1D+1D DMFC model have been re-calibrated on the polarization curve during which the EIS were performed, while the values of the double layer capacitances are fitted over EIS. The resulting fitting parameters are reported in Table 5.1, while the parameters of Tables 3.1-3.4 still remain valid.

α^{c}	-	0.65
i_{*}^{c}	$A \cdot cm^{-2}$	$1.5 \cdot 10^{-4} \cdot exp(50750/R \cdot (1/353 - 1/T))$
$C_{dl,0.075A \cdot cm^{-2}}^{c}$	$F \cdot cm^{-2}$	$7.4 \cdot 10^{-3}$
$C_{dl,0.15A \cdot cm^{-2}}^{c}$	$F \cdot cm^{-2}$	$5.8 \cdot 10^{-3}$

Table 5.1: Fitted parameters for cathode impedance simulation (MEA GM).

In particular the experimental measurements have been carried out on MEA GM, at 333 K and 1 bar, with a methanol concentration of 3.25%wt and

with methanol and air flow rate equal to 1 $g \cdot min^{-1}$ and 0.62 $g \cdot min^{-1}$, respectively.
Fig. 5.2 illustrates the modeling results at 0.075 $A \cdot cm^{-2}$ and the model reproduces experimental data with high accuracy. Despite the Nernst hypothesis provides a simplified model for convective-diffusion impedance, the approximation is acceptable: in fact the simulated total resistance is close to the measured value.

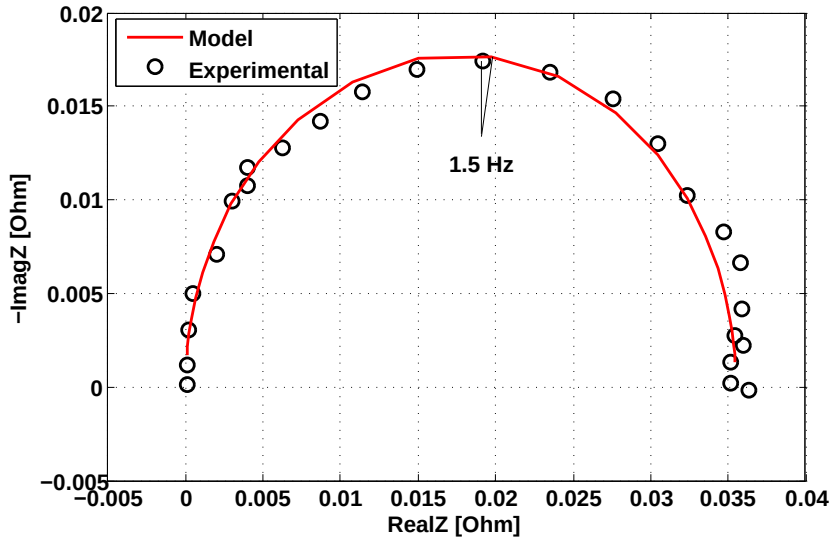

Figure 5.2: Simulated and measured cathode Nyquist plot at 0.075 $A \cdot cm^{-2}$ (MEA GM, met 3.25%wt - 1 $g \cdot min^{-1}$, 333 K, air 0.62 $g \cdot min^{-1}$, 1 bar).

The proposed innovative model for the interpretation of impedance spectra is more reliable than the classical equivalent circuit method, because the equivalent circuit elements are function of the physical parameters of the DMFC. Moreover with the proposed approach it is possible to obtain the values of the equivalent circuit elements along the channel length: this permits to quantify DMFC local internal losses.
Fig. 5.3 reports the values of the charge transfer resistance and the real part of mass transfer impedance along channel length. Both R^c_{ct} and $real(Z^c_{mt})$ increase along channel length, coherently with a reduction of current density and oxygen concentration. As expected from the shape of the spectrum, that is almost an ideal semicircle, the contribution of mass transfer impedance is negligible.
Doubling the current density the model simulates experimental observation with sufficient accuracy, Fig. 5.4.
It is possible to note that in the low frequency region the model slightly

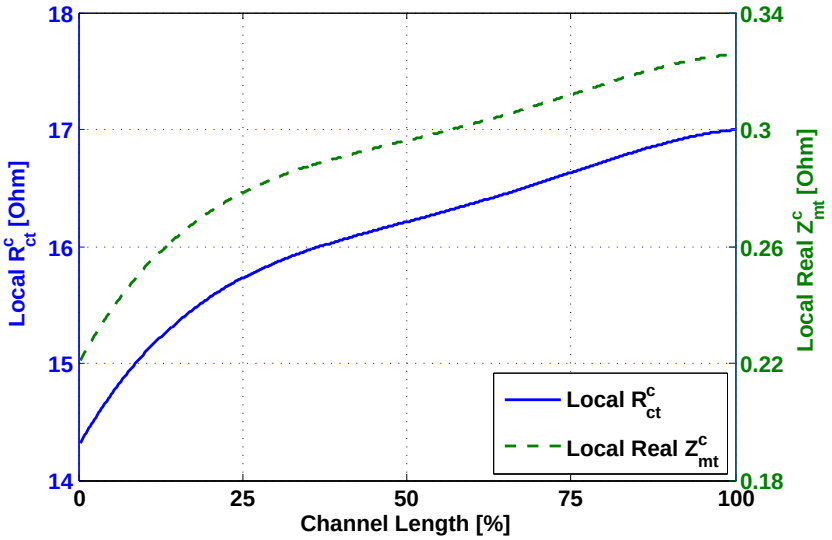

Figure 5.3: Simulated local R^c_{ct} and $real(Z^c_{mt})$ at 0.075 $A \cdot cm^{-2}$ (MEA GM, met 3.25%wt - 1 $g \cdot min^{-1}$, 333 K, air 0.62 $g \cdot min^{-1}$, 1 bar).

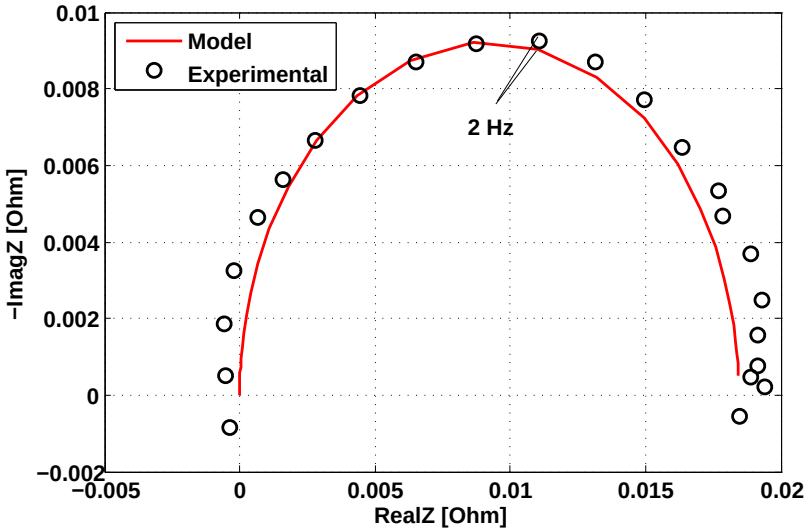

Figure 5.4: Simulated and measured cathode Nyquist plot at 0.15 $A \cdot cm^{-2}$ (MEA GM, met 3.25%wt - 1 $g \cdot min^{-1}$, 333 K, air 0.62 $g \cdot min^{-1}$, 1 bar).

underestimates experimental data: this could be due to the hypothesis of Nernst stagnant diffusion.
Once again the charge transfer resistance and the real part of mass transfer impedance increase along channel length, Fig. 5.5. However comparing these results with those of Fig. 5.3, it is interesting to note that the value of R^c_{ct} is almost halved, coherently with Eq. 5.37. Instead the real part of mass transfer impedance is nearly the same; only a slight increment is evident.

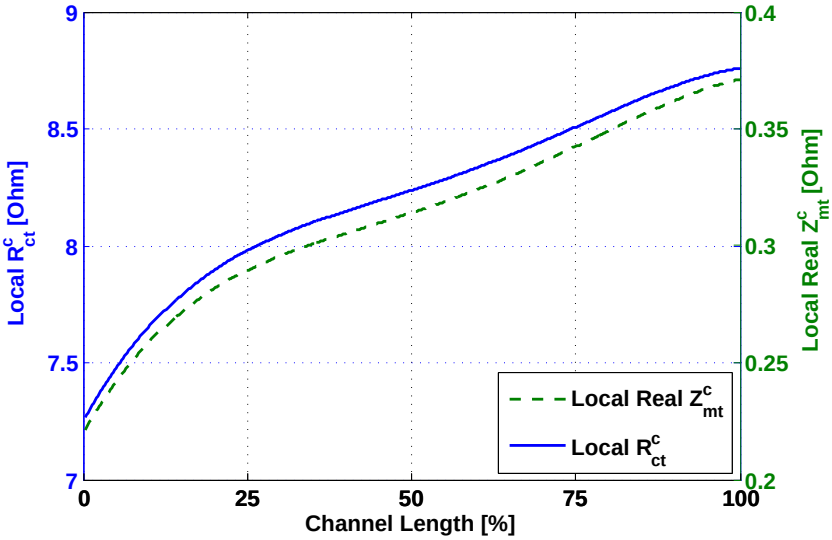

Figure 5.5: Simulated local R^c_{ct} and $real(Z^c_{mt})$ at 0.15 $A \cdot cm^{-2}$ (MEA GM, met 3.25%wt - 1 $g \cdot min^{-1}$, 333 K, air 0.62 $g \cdot min^{-1}$, 1 bar).

This feature could be due to the reduced methanol cross-over, caused by the higher operating current: in fact, as explained in paragraph 4.3.2, high methanol cross-over enhances oxygen consumption at cathode side, especially at high current densities and low cathode flow rate. In such operating conditions mass transport limitations manifest themselves as a clear second arch. For this reason, in order to consolidate the experimental observations of paragraph 4.3.2, a sensitivity analysis has been carried out varying cathode flow rate and methanol feeding concentration at high operating current. In Fig. 5.6 the onset of the second arch is evident and moreover it is possible to notice that a reduction of cathode flow rate and an increase of methanol concentration enlarge its magnitude. Therefore model predictions are in full qualitative agreement with EIS measurements reported in Fig. 4.11, that have been performed on the IRD MEA MM.
Because of the cathode impedance has already been extensively studied [126, 128] and the calibration is a time consuming activity, no efforts to quan-

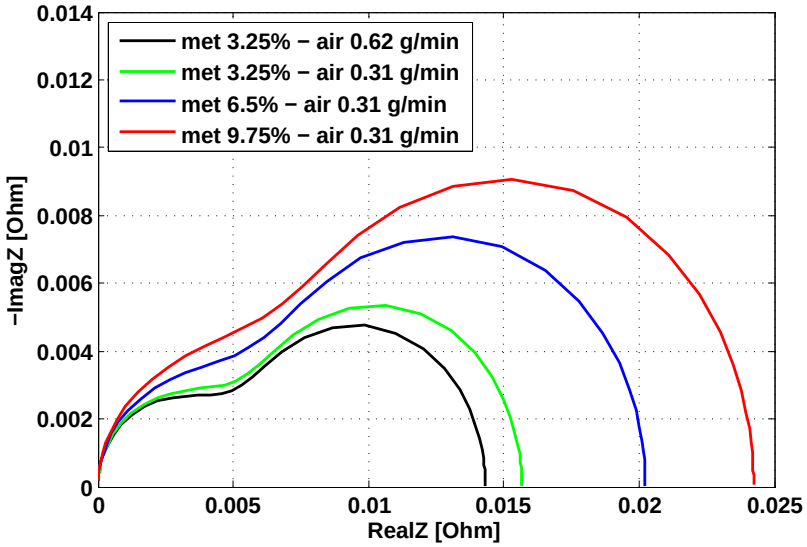

Figure 5.6: Simulated cathode spectra at 0.25 $A \cdot cm^{-2}$ (MEA GM, met 1 $g \cdot min^{-1}$, 333 K, 1 bar).

titative validate the model on IRD MEA MM data have been done. Instead, because of the interpretation of anode impedance is not consolidated and only few experimental investigations can be found in the literature [119, 133], in the next paragraph the proposed approach is applied to the interpretation of anode impedance.

5.3 Model of anode impedance

As previously discussed in chapter 4, in order to measure the anode impedance with a reduced uncertainty it is necessary to perform the EIS during half cell operation, feeding hydrogen at the cathode. As a consequence the 1D+1D DMFC model has been modified to take into account the half cell operation, named anode polarization.

5.3.1 DMFC anode polarization model

During anode polarization cathode is considered a reference electrode, in particular a pseudo-DHE (dynamic hydrogen electrode) [134], whose potential is nearly constant and negligible in comparison to anode. Therefore in the anode polarization model the cathode overpotential is neglected and the voltage variations are mainly attributable to anode and membrane overpotentials, as

described in [135]. The Eq. 29 in [71] is thus replaced by the following:

$$V_{cell} = \eta^a + \eta^{ohm} \tag{5.41}$$

Regarding the continuity equations at cathode side, the following modifications have been introduced:

- air is replaced by hydrogen and therefore Eq. 12 and 15 in [71] are substituted with:
$$\frac{h^c}{2} \cdot \frac{\partial \left(v^c \cdot C^c_{H_2}\right)}{\partial x} = \frac{i}{2 \cdot F} \tag{5.42}$$
- CO_2 (Eq. 13 in [71]) is removed because the methanol cross-over flux is no longer oxidized;
- water production in the cathode catalyst layer is not considered because of the hydrogen feeding and Eq. 14 in [71] becomes:
$$\frac{h^c}{2} \cdot \frac{\partial \left(v^c \cdot \bar{C}^c_{H_2O}\right)}{\partial x} = N^{H_2O}_{cross} \tag{5.43}$$

Moreover, coherently with the presence of low frequency inductive loop (Fig. 4.2-4.4), a reaction mechanism involving intermediate adsorbates is assumed. In particular the following two-steps reaction mechanisms with a single adsorbed intermediate [119, 124, 136] is introduced in the model:

$$\begin{aligned} &1.\quad CH_3OH + Pt \longrightarrow Pt\_CO + 4H^+ + 4e^- \\ &2.\quad Pt\_CO + H_2O \longrightarrow Pt\_CO_2 + 2H^+ + 2e^- \end{aligned} \tag{5.44}$$

In the first reaction step the adsorbed intermediate CO is formed in the process of methanol dehydrogenation, while in the second reaction step adsorbed CO undergoes further oxidation to CO_2 in a process involving the transfer of two protons and two electrons.
Assuming a Tafel Kinetics, the current density related to the first reaction step is:

$$i_1 = i_{*1} \cdot \left(\frac{\bar{C}^{t,a}_{CH_3OH}}{C^a_{ref,1}}\right)^{\gamma^a_1} \cdot (1 - \gamma_{CO}) \cdot exp(\eta / b_1) \tag{5.45}$$

where γ_{CO} represents the surface coverage by the CO intermediate. Instead, the current density associated with the second reaction step is expressed as:

$$i_1 = i_{*2} \cdot \gamma_{CO} \cdot exp(\eta / b_2) \tag{5.46}$$

Due to the high concentration of water in the electrode, for simplicity this reaction step is considered independent on water concentration. The total current density is then equal to:

$$i = i_1 + i_2 \tag{5.47}$$

The variation of the surface coverage by the CO intermediate is given by the following expression:

$$\Gamma_{Pt} \cdot \frac{\partial \gamma_{CO}}{\partial t} = \frac{i_1}{4 \cdot F} - \frac{i_2}{2 \cdot F} \tag{5.48}$$

where Γ_{Pt} is the platinum active site density. Under steady-state conditions the left end side of Eq. 5.48 is equal to zero and $i_1 = 2 \cdot i_2$; by using the corresponding equations 5.45 and 5.46, an expression for steady-state surface coverage is obtained as:

$$\gamma_{CO} = \frac{i_{*1} \cdot (\bar{C}^{t,a}_{CH_3OH}/C^a_{ref,1})^{\gamma^a_1} \cdot exp(\eta/b_1)}{i_{*1} \cdot (\bar{C}^{t,a}_{CH_3OH}/C^a_{ref,1})^{\gamma^a_1} \cdot exp(\eta/b_1) + 2 \cdot i_{*2} \cdot exp(\eta/b_2)} \tag{5.49}$$

Substituting the expression of γ_{CO} in one of the equations 5.45 and 5.46 and considering that under steady-state conditions $i_1 = 2 \cdot i_2$, it is possible to obtain two different implicit expressions of anode overpotential, respectively equal to:

$$\begin{gathered} \eta^a = b_1 \cdot log\left(\frac{2/3 \cdot i}{i_{*1} \cdot (\bar{C}^{t,a}_{CH_3OH}/C^a_{ref,1})^{\gamma^a_1} \cdot (1 - \gamma_{CO})}\right) \\ \eta^a = b_2 \cdot log\left(\frac{1/3 \cdot i}{i_{*2} \cdot \gamma_{CO}}\right) \end{gathered} \tag{5.50}$$

One of Eq. 5.50 substitutes equation 21 in [71].
All the above described improvements and modifications to take into account the half cell operation have been introduced in the previous 1D+1D DMFC model. In order to obtain an accurate estimation of anode kinetic parameters and improve the reliability of the results, the anode kinetic parameters have been re-calibrated on the anode polarization during which anode EIS were performed.
The model reproduces experimental data with high accuracy (Fig. 5.7) and the calibration parameters have reasonable values, Table 5.2. The other parameters reported in Tables 3.1-3.4, characterizing MEA GM operation, still remain valid.

α_1^a	-	0.45
i_{*1}^a	$A \cdot cm^{-2}$	$6.45 \cdot 10^{-4} \cdot exp(66712/R \cdot (1/353 - 1/T))$
γ_1^a	–	0.3
α_2^a	-	0.33
i_{*2}^a	$A \cdot cm^{-2}$	$2.9 \cdot 10^{-3} \cdot exp(66712/R \cdot (1/353 - 1/T))$

Table 5.2: Fitted parameters of anode polarization (MEA GM, met 3.25%wt - 1 $g \cdot min^{-1}$, 333 K, 1bar).

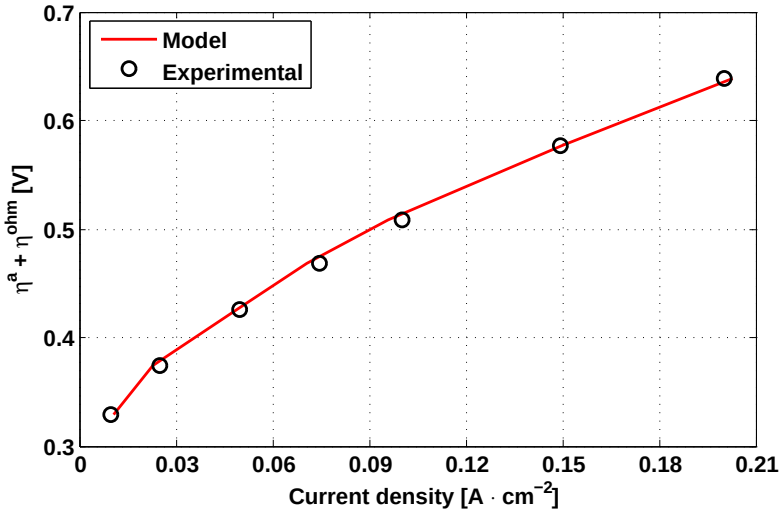

Figure 5.7: Comparison of the simulated and measured anode polarization (MEA GM, met 3.25%wt - 1 $g \cdot min^{-1}$, 333 K, 1 bar).

5.3.2 Impedance model development

In the literature there is no reference on the modeling of DMFC anode impedance, but only few experimental studies can be found [119, 124, 133], in which the interpretation of experimental observation has mostly been carried out by means of equivalent electric circuit method.
In this paragraph, combining the DMFC anode polarization model with the analytical approach presented paragraph 5.1, an anode impedance model has been develop. Therefore the analytical approach for impedance modeling is applied to a two-steps reaction, the first depends on potential, mass transfer and surface coverage at the same time, while the second depends only on potential and surface coverage. This entails a relatively complex equivalent electric circuit, that is reported in the following figure:

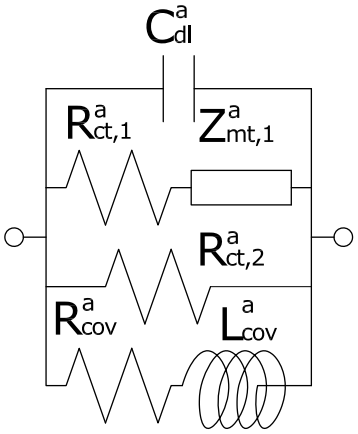

Figure 5.8: Anode equivalent electric circuit.

According to the methodology presented in paragraph 5.1 and the nomenclature of the 1D+1D DMFC anode polarization model, the value of the equivalent circuit elements are respectively equal to[3]:

$$R^a_{ct,1} = \frac{b^a_1}{i^a_{*1} \cdot (\bar{C}^{t,a}_{CH_3OH}/C^a_{ref,1})^{\gamma^a_1} \cdot (1-\gamma_{CO}) \cdot exp(\eta^a/b^a_1)} = \frac{b^a_1}{i_1} \tag{5.51}$$

$$R^a_{ct,2} = \frac{b^a_2}{i^a_{*2} \cdot \gamma_{CO} \cdot exp(\eta^a/b^a_2)} = \frac{b^a_2}{i_2} \tag{5.52}$$

$$Z^a_{mt,1} = \frac{\gamma^a_1 \cdot l^a_{GDL} \cdot b^a_1}{4 \cdot F \cdot \bar{D}^a_{GDL,CH_3OH} \cdot \bar{C}^{t,a}_{CH_3OH}} \cdot \frac{tanh\sqrt{j \cdot H}}{\sqrt{j \cdot H}} \tag{5.53}$$

$$R^a_{cov} = \frac{\dfrac{b^a_1}{(1-\gamma_{CO}) \cdot (R^a_{ct,1} + Z^a_{mt,1})} + \dfrac{2 \cdot b^a_2}{\gamma_{CO} \cdot R^a_{ct,2}}}{\left[\dfrac{b^a_2}{\gamma_{CO} \cdot R^a_{ct,2}} - \dfrac{b^a_1}{(1-\gamma_{CO}) \cdot (R^a_{ct,1} + Z^a_{mt,1})}\right] \cdot \left[\dfrac{1}{R^a_{ct,1} + Z^a_{mt,1}} - \dfrac{2}{R^a_{ct,2}}\right]} \tag{5.54}$$

$$L^a_{cov} = \frac{4 \cdot F \cdot \Gamma_{Pt}}{\left[\dfrac{b^a_2}{\gamma_{CO} \cdot R^a_{ct,2}} - \dfrac{b^a_1}{(1-\gamma_{CO}) \cdot (R^a_{ct,1} + Z^a_{mt,1})}\right] \cdot \left[\dfrac{1}{R^a_{ct,1} + Z^a_{mt,1}} - \dfrac{2}{R^a_{ct,2}}\right]} \tag{5.55}$$

[3]Note that the expression for the elements corresponding to the first reaction step are slightly different from those reported in paragraph 5.1.3 because this reaction step depends on potential, concentration and surface coverage at the same time and moreover the reaction order γ^a_1 is not equal to one.

Instead, the double layer capacitance and the active site density are considered constant along channel length and are fitted over experimental data.
As already done for cathode impedance, the model is integrated along channel length and therefore the total impedance is calculated according to Eq. 5.39, but the total impedance of each local equivalent circuit is equal to:

$$Z^c_{tot,i} = \left(\frac{1}{R^a_{ct,1} + Z^a_{mt,1}} + \frac{1}{R^a_{ct,2}} + \frac{1}{R^a_{cov} + j \cdot \omega \cdot L^a_{cov}} + j \cdot \omega \cdot C^a_{dl} \right)^{-1} \quad (5.56)$$

5.3.3 Modeling results

Fig. 5.9 and 5.10 illustrate simulation results at 0.075 $A \cdot cm^{-2}$; the values of double layer capacitance and active site density are fitted with respect to EIS data and the resulting values are reported in Table 5.3.

C^a_{dl}	$F \cdot cm^{-2}$	$8.1 \cdot 10^{-4}$
Γ_{Pt}	$mol \cdot cm^{-2}$	$3.1 \cdot 10^{-8}$

Table 5.3: Fitted parameters for anode impedance simulation (MEA GM).

The model reproduces inductive behavior with sufficient accuracy (Fig. 5.9) and there is also good agreement between model predictions and experimental relaxation frequencies (Fig. 5.10).
However the simulated spectrum is almost an ideal semicircle and the model underestimates the total resistance. As discussed in paragraph 4.2.1, the elongated shape of the spectrum is partially due to proton transport limitations through the catalyst layer, that in the model are not considered.
Moreover in the 1D+1D DMFC model the complicated mass transport at anode side is described by a two-phase Fick's law of diffusion (Eq. 18 in [71]): this simplification, along with the assumption of Nernst stagnant diffusion, lead to a poor evaluation of mass transfer impedance and the model underestimates the total resistance.
In fact the local values of the real part of mass transfer impedance reported in Fig. 5.11 are comparable with the cathode ones, Fig. 5.3: considering that the anode is fed with liquid methanol, whose diffusivity is nearly 3 order of magnitude lower than the gas one, the resulting value of $real(Z^a_{mt,1})$ would seem too small.
Instead comparing the charge transfer resistances of the two reaction steps of methanol oxidation, it is interesting to notice that $R^a_{ct,2}$ (Fig. 5.12) is almost three times higher than $R^a_{ct,1}$. This implies that the kinetic losses associated with the oxidation of adsorbed CO are predominant. Moreover

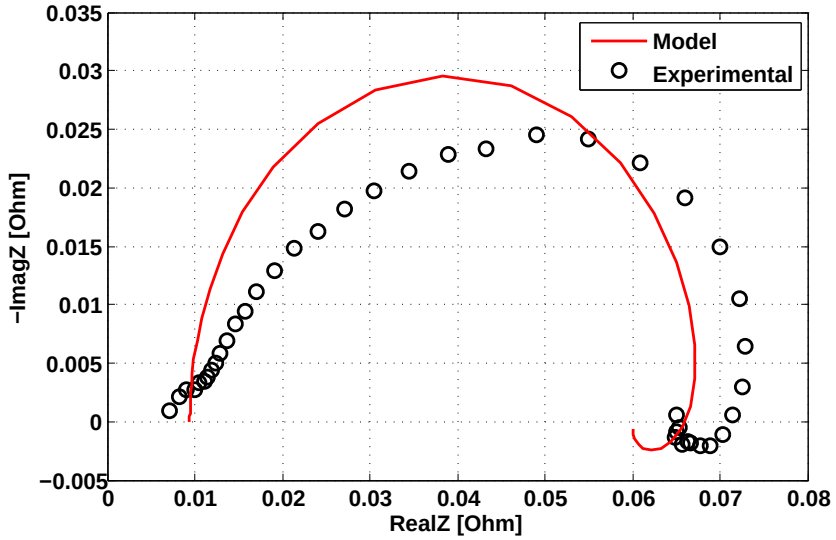

Figure 5.9: Simulated and measured anode Nyquist plot at 0.075 $A \cdot cm^{-2}$ (MEA GM, met 3.25%wt - 1 $g \cdot min^{-1}$, 333 K, 1 bar).

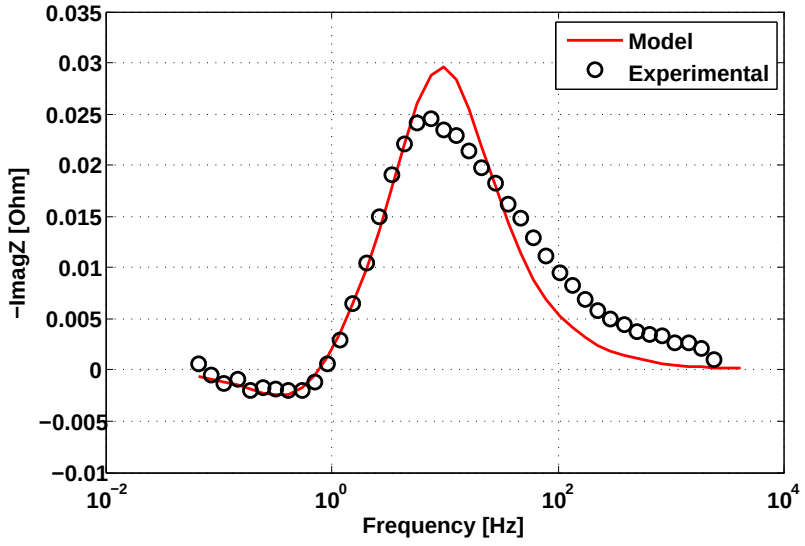

Figure 5.10: Simulated and measured anode Bode plot at 0.075 $A \cdot cm^{-2}$ (MEA GM, met 3.25%wt - 1 $g \cdot min^{-1}$, 333 K, 1 bar).

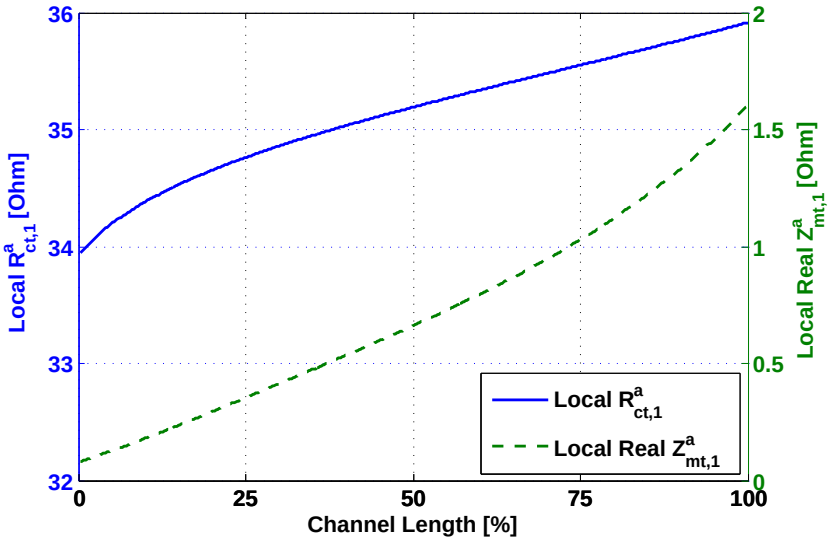

Figure 5.11: Simulated local $R^a_{ct,1}$ and $real(Z^a_{mt,1})$ at 0.075 $A \cdot cm^{-2}$ (MEA GM, met 3.25%wt - 1 $g \cdot min^{-1}$, 333 K, 1 bar).

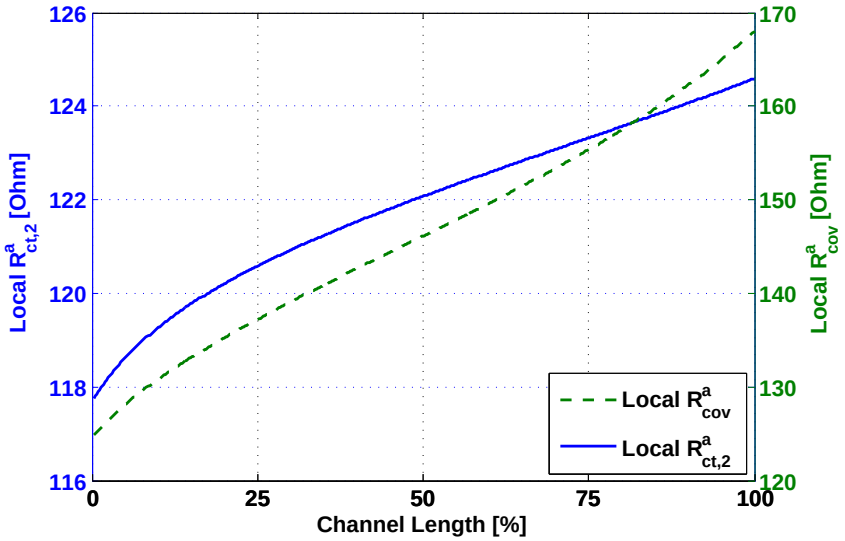

Figure 5.12: Simulated local $R^a_{ct,2}$ and R^a_{cov} at 0.075 $A \cdot cm^{-2}$ (MEA GM, met 3.25%wt - 1 $g \cdot min^{-1}$, 333 K, 1 bar).

Fig. 5.12 illustrates that R^a_{cov} increases along channel length and therefore the magnitude of the inductive loop is more evident towards the end of the channel.
In conclusion, the developed model of DMFC anode impedance is not sufficiently accurate for a quantitative interpretation of experimental data; a more detailed description of mass transport phenomena and the consideration of proton transport through the catalyst layer are necessary to reproduce experimental data with higher accuracy. Consequently a physically based model of DMFC anode impedance is presented in the next chapter.

5.4 Remarks

In this chapter a preliminary model for a quantitative interpretation of both DMFC cathode and anode impedance has been developed. In particular the approach already proposed in [81] has been adapted to DMFC technology and locally integrated in the 1D+1D DMFC model of chapter 3. The following considerations can be highlighted:

- The developed model is more reliable than the classic ECM because the equivalent circuit elements are function of the physical parameters of the system, obtained from the validation of the 1D+1D DMFC model of chapter 3. Moreover by means of the developed approach it is possible to calculate the local values of equivalent circuit elements, providing an insight into the understanding of internal DMFC losses.

- Despite the Nernst hypothesis, cathode simulations reproduce experimental observations with good accuracy. The kinetic losses are considerably higher than mass transfer ones and both the local values of charge transfer resistance and the real part of mass transfer impedance increase along channel length, coherently with a reduction of current density and oxygen concentration, respectively.

- The cathode impedance model qualitatively reproduces the effect of a poor oxygen concentration in the electrode: at high current density a second arch is evident in the low frequency region. This arch, peculiar of mass transport limitations, is enlarged by reduced cathode flow rate and increased methanol concentration.

- The anode model reproduces inductive behavior with high accuracy and the magnitude of the inductive loop increases along channel length.

- The charge transfer resistance of the second reaction step of methanol oxidation is nearly three times higher than that of the first step: this implies that the kinetic losses associated with the oxidation of adsorbed CO are predominant.
- The anode model does not take into account proton transport limitations and the simulated spectrum is not an elongated semicircle. Moreover the simplified two-phase mass transport description through anode GDL, along with the Nernst hypothesis, are not sufficiently accurate to calculate mass transfer impedance.

Despite the cathode simulations are in good agreement with experimental observations, the interpretation of anode data is still difficult and analysis through physical modeling becomes crucial to elucidate the origin of anode impedance features. Indeed the next chapter is about the development of a physical model of anode impedance, in which proton transport through the catalyst layer and a detailed description of mass transport phenomena are implemented.

Chapter 6

EIS: anode physical model development

Since the preliminary modeling approach of chapter 5 showed good agreement with experimental data of cathode impedance, but the anodic one presents the above mentioned limits, a physical model of anode impedance has been developed from scratch.

6.1 Model development

In the literature only few studies [65, 66] report physical model of DMFC cathode impedance, but there is no reference on the DMFC anode. In [65, 66] a clear and detailed explanation of the mathematical model of DMFC cathode impedance is reported and discussed. The models in [65, 66] qualitatively explain the effects of physical phenomena on the shape of impedance spectrum. However the model is not integrated along channel length and no attempts to fit experimental data have been done.
In this chapter, starting from the mathematical approach presented in [65, 66], a DMFC anode impedance model has been developed from scratch, increasing progressively the details of the described phenomena and evaluating different possible modeling solutions. In this work only the final results are reported. In particular a detailed description of mass transport phenomena

through anode GDL and a catalyst layer with a finite thickness have been introduced in the DMFC anode polarization model presented in chapter 5.

6.1.1 GDL model

In the 1D+1D DMFC model presented in chapter 3, due to the high availability of water at the anode, the phenomena governing water transport through anode GDL are omitted and the water transport through the MEA is assumed to be regulated by water transport through the membrane and cathode diffusion layer, Fig. 3.1. Moreover in the original model the methanol flux through the anode GDL is governed by gas and liquid diffusion, assuming that liquid saturation is constant across the diffusion layer thickness (Eq. 18 in [71]).
In the model developed in this chapter the following improvements have been introduced:

- the water is transported through the anodic GDL by liquid convection, Fig. 6.1: however the water transport through the MEA is still regulated by water transport through the membrane and cathode diffusion layer, coherently with the previously proposed interpretations of water management;

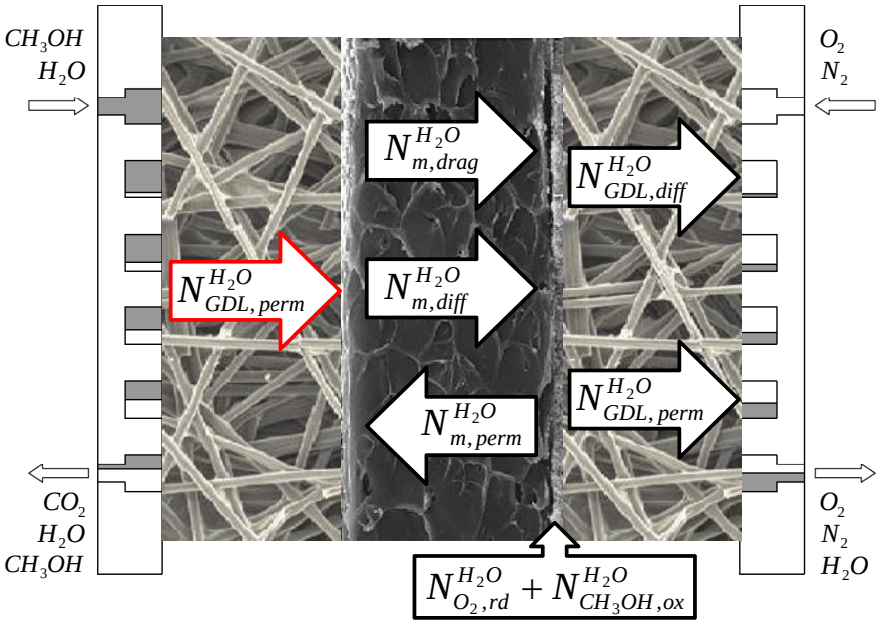

Figure 6.1: Water fluxes through the DMFC.

- the contribution of methanol liquid convection is considered;
- liquid saturation is no longer constant across the diffusion layer thickness due to the liquid convective fluxes.

The equations that fully describe mass transport phenomena through anode GDL are the following[1]:

$$\begin{aligned} -D^{L}_{GDL,CH_3OH} \cdot s_{GDL} \cdot \frac{\partial C^{GDL,L}_{CH_3OH}}{\partial x} - D^{G}_{GDL,CH_3OH} \cdot (1 - s_{GDL}) \\ \cdot \frac{\partial C^{GDL,G}_{CH_3OH}}{\partial x} = N^{CH_3OH}_{GDL} - N^{H_2O}_{GDL} \cdot \frac{C^{GDL,L}_{CH_3OH}}{C^{GDL,L}_{H_2O}} \end{aligned} \tag{6.1}$$

$$\begin{aligned} \frac{\partial s_{GDL}}{\partial x} = \frac{1}{s^3_{GDL} \cdot (1.417 - 4.24 \cdot s_{GDL} + 3.789 \cdot s^2_{GDL})} \\ \cdot \frac{M_{H_2O} \cdot \mu_{H_2O}}{\rho_{H_2O} \cdot \sigma_{H_2O} \cdot cos\theta_c \cdot (\epsilon_{GDL} \cdot K_{GDL})^{0.5}} \cdot N^{H_2O}_{GDL} \end{aligned} \tag{6.2}$$

$$\frac{\partial N^{CH_3OH}_{GDL}}{\partial x} = -\epsilon_{GDL} \cdot s_{GDL} \cdot \frac{\partial C^{GDL,L}_{CH_3OH}}{\partial t} - \epsilon_{GDL} \cdot (1 - s_{GDL}) \cdot \frac{\partial C^{GDL,G}_{CH_3OH}}{\partial t} \tag{6.3}$$

$$\frac{\partial N^{H_2O}_{GDL}}{\partial x} = -\epsilon_{GDL} \cdot s_{GDL} \cdot \frac{\partial C^{GDL,L}_{H_2O}}{\partial t} - \epsilon_{GDL} \cdot (1 - s_{GDL}) \cdot \frac{\partial C^{GDL,G}_{H_2O}}{\partial t} \tag{6.4}$$

Eq. 6.1 is the Fick's law of diffusion for two-phase methanol, in which the second term in the right end side of the equation is the contribution of methanol liquid convection. As proposed in [71], the methanol concentrations in gas and liquid phases are considered in equilibrium, described by Henry's law:

$$C^{GDL,L}_{CH_3OH} = K_{H,CH_3OH} \cdot C^{GDL,G}_{CH_3OH} \cdot R \cdot T \tag{6.5}$$

Instead Eq. 6.2 is the governing equation of water transport, that is described by the Leverett function [101]. Eq. 6.3 and 6.4 express the mass balance of methanol and water, respectively; the liquid phase accumulation term is proportional to the liquid saturation, while the gas phase one is proportional to the void fraction.
Particular attention has been given to the understanding of the mechanisms regulating liquid convective fluxes. In fact the GDL is not assumed to be always flooded with fully liquid pathways, as widely accepted in the literature [74, 101]. Recent studies on liquid convection through GDLs [97, 137] showed

[1] All the interested quantities are relative to the anode: for this reason the superscript ^{a} is removed from all the symbols.

that liquid paths are intermittent and breakthrough locations change with time. These flow visualizations [97, 137] suggest that the liquid transport within the GDL is a process of capillary pressure buildup and breakthrough at the interface of GDL intersecting fibers, Fig. 6.2.a.

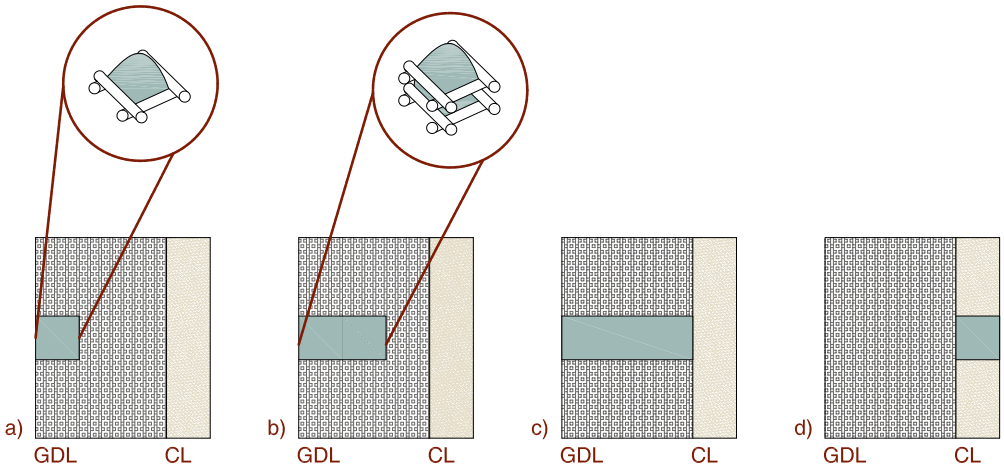

Figure 6.2: Schematic illustration of intermittent liquid convection.

When the liquid pressure exceeds the breakthrough value, the liquid expands rapidly through this interface until the fluid contacts the next fiber intersections interface, Fig. 6.2.b. Then the process of pressure buildup and breakthrough begins again until the fluid reaches the GDL-CL interface, Fig. 6.2.c. At this interface, when the capillary pressure exceeds the threshold value, the liquid is quickly removed from GDL pores, that become empty, Fig. 6.2.d. The dynamic of liquid emergence and detachment from GDL surface is very fast, in the order of few milliseconds, and it is enhanced by GDL hydrophobicity [138, 139].
The proposed description of intermittent liquid convective flux implies that the effect of liquid accumulation terms in the GDL (Eq. 6.3 and 6.4) is only present meanwhile liquid flux to the CL effectively occurs[2], or rather for frequencies higher than tens of Hertz. A threshold value of 75 Hz is assumed.

6.1.2 Electrode model

In the original 1D+1D anode polarization model presented in paragraph 5.3.1, the electrode is assumed to be monodimensional in the direction of channel length. In the new model an electrode with a finite thickness is

[2]Note that when no liquid flux to the CL occurs, this intermittent description excludes the effect, but not the presence, of liquid accumulations in the GDL.

introduced in order to take into account proton transport limitations. The system that fully describes the catalyst layer behavior is the following:

$$\frac{\partial i}{\partial x} = i_{*v1} \cdot \frac{\bar{C}^t_{CH_3OH}}{C_{ref,1}} \cdot (1 - \gamma_{CO}) \cdot e^{\frac{\eta}{b_1}} + i_{*v2} \cdot \frac{\bar{C}^t_{H_2O}}{C_{ref,2}} \cdot \gamma_{CO} \cdot e^{\frac{\eta}{b_2}} \tag{6.6}$$

$$-\bar{D}_{t,CH_3OH} \cdot \frac{\partial^2 \bar{C}^t_{CH_3OH}}{\partial x^2} = -\frac{1}{4 \cdot F} \cdot \frac{\partial i_1}{\partial x} - \epsilon_t \cdot \frac{\partial \bar{C}^t_{CH_3OH}}{\partial t} \tag{6.7}$$

$$-\bar{D}_{t,H_2O} \cdot \frac{\partial^2 \bar{C}^t_{H_2O}}{\partial x^2} = -\frac{1}{2 \cdot F} \cdot \frac{\partial i_2}{\partial x} - \epsilon_t \cdot \frac{\partial \bar{C}^t_{H_2O}}{\partial t} \tag{6.8}$$

$$\frac{\partial \eta}{\partial x} = \frac{i}{\sigma_t} \tag{6.9}$$

$$\Gamma_{Pt} \cdot \frac{\partial \gamma_{CO}}{\partial t} = \frac{1}{4 \cdot F} \cdot \frac{\partial i_1}{\partial x} - \frac{1}{2 \cdot F} \cdot \frac{\partial i_2}{\partial x} \tag{6.10}$$

Eq. 6.6 describes charge conservation in the catalyst layer; the methanol oxidation reaction mechanism is the same of that of paragraph 5.3.1, but two differences are appreciable:

- the reaction order of the first reaction step is assumed equal to 1 [12];
- the second reaction step is dependent on the average water concentration in the electrode.

Eq. 6.7 and 6.8 express the mass balance of methanol and water, respectively. Due to the strong uncertainties related to the two-phase mass transport phenomena in the electrode [96], considering for example the mixture phase transition and the evolution of CO_2 bubbles, average concentrations and diffusivities are considered for simplicity. In particular, the average diffusivities of methanol and water are assumed equal to each other and proportional to the average diffusivity of the GDL:

$$\bar{D}_{t,CH_3OH} = \bar{D}_{t,H_2O} = \frac{N^{CH_3OH}_{GDL} \cdot l_{GDL}}{\bar{\Delta C}^{GDL,L} \cdot \bar{s}_{GDL} + \bar{\Delta C}^{GDL,G} \cdot (1 - \bar{s}_{GDL})} \cdot CF \tag{6.11}$$

CF is a correction factor, that takes into account the different porosity and void fraction of the catalyst layer.
Eq. 6.9 is the Ohm's law relating the proton current density to the gradient of overpotential; it is necessary to take into account the proton transport limitations in the impedance spectrum.
Eq. 6.10 describes the variation of the surface coverage by the CO adsorbed intermediate: the first reaction step produces CO coverage, while the second reaction step consumes CO coverage.

6.1.3 DMFC anode polarization model

The systems characterizing GDL (Eq. 6.1-6.4) and catalyst layer (Eq. 6.6-6.10) behavior have been introduced in the steady state DMFC anode polarization model of paragraph 5.3.1. The GDL equations are solved applying the appropriate boundary conditions regarding methanol concentration and saturation at the channel-GDL interface. The complicated two-phase hydrodynamics in the channel makes the liquid saturation at this interface difficult to determine theoretically. In the literature, the most of the works [8, 28] suppose its value: in [8] it is equal to 0.8, while in [28] it is equal 0.65, despite the lower hydrophobicity of the considered diffusion media. Moreover, the above cited works [8, 28] propose a 1D model along the thickness of the DMFC and no attempts to calculate s_{ch-GDL} profile along channel length have been done. In [69], in which a complete DMFC model is presented, the saturation at channel-GDL interface is assumed equal to the channel one: however this assumption is not coherent with the different hydrophilic-hydrophobic properties between the channel and the diffusion media. In [107], instead, an empirical approach is taken: the boundary condition regarding s_{ch-GDL} profile along channel length is expressed as a function of the current density. According to [107], also in this work an empirical approach is adopted. The saturation is not assumed directly proportional to the current density, but the following dependence on saturation in the channel is proposed:

$$s_{ch-GDL} = S_1 \cdot s_{ch}^{S_2} + S_3 \tag{6.12}$$

where s_{ch} is the saturation in the channel and the parameters S_1, S_2 and S_3 are calibrated over experimental data.
Subsequently, as widely accepted in the literature [8, 140], the liquid saturation at the GDL-electrode interface in the electrode can be calculated by assuming that the capillary pressure remains uniform across the interface:

$$p_c|_{GDL-el^-} = p_c|_{GDL-el^+} \tag{6.13}$$

According to [101], the capillary pressure can be expressed as:

$$p_c = \sigma_{H_2O} \cdot cos\theta_c \cdot (\epsilon/K)^{0.5} \cdot J(s) \tag{6.14}$$

where $J(s)$ is the Leverett function and for an hydrophobic medium is given by the following relation:

$$J(s) = 1.417 \cdot s - 2.120 \cdot s^2 + 1.263 \cdot s^3 \tag{6.15}$$

Instead the system describing catalyst layer behavior is subject to the following boundary conditions:

$$i|_{GDL-el} = 0 \tag{6.16}$$

$$i|_{el-m} = i_{cell} \tag{6.17}$$

$$-\bar{D}_{t,CH_3OH} \cdot \left.\frac{\partial \bar{C}^t_{CH_3OH}}{\partial x}\right|_{GDL-el} = N^{CH_3OH}_{GDL} \tag{6.18}$$

$$-\bar{D}_{t,H_2O} \cdot \left.\frac{\partial \bar{C}^t_{H_2O}}{\partial x}\right|_{GDL-el} = N^{H_2O}_{GDL} \tag{6.19}$$

$$\bar{C}^t_{CH_3OH}\big|_{GDL-el} = s_{el} \cdot C^L_{CH_3OH}\big|_{GDL-el} + (1 - s_{el}) \cdot C^G_{CH_3OH}\big|_{GDL-el} \tag{6.20}$$

$$\bar{C}^t_{CH_2O}\big|_{GDL-el} = s_{el} \cdot C^L_{CH_2O}\big|_{GDL-el} + (1 - s_{el}) \cdot C^{sat}_{H_2O} \tag{6.21}$$

This is a two-point boundary value problem and the built in BVP function of MATLAB® environment has been used for the numerical resolution of the system of Eq. 6.6-6.10. The increased complexity of the developed model and the more detailed description of the DMFC operation make the calibration procedure more difficult; however the model reproduces experimental observations with good accuracy (Fig. 6.3) and all the obtained calibration parameters have reasonable values (Table 6.1).

α_1	-	0.74
i_{*v1}	$A \cdot cm^{-3}$	$6.18 \cdot 10^{-5} \cdot exp(8024 \cdot (1/353 - 1/T))$
α_2	-	0.38
i_{*v2}	$A \cdot cm^{-3}$	$2.39 \cdot 10^{-2} \cdot exp(8024 \cdot (1/353 - 1/T))$
$C_{ref,2}$	$mol \cdot cm^{-3}$	0.055
l_t	cm	$4 \cdot 10^{-3}$
σ_t	$\Omega^{-1} \cdot cm^{-1}$	$4 \cdot 10^{-3}$
D^G_{GDL,CH_3OH}	$cm^2 \cdot s^{-1}$	$1.52 \cdot 10^{-2}$
K_{GDL}	m^2	$1 \cdot 10^{-14}$
θ_c	^{o}	130
σ_{H_2O}	$N \cdot m^{-1}$	0.0625
CF	–	0.1
S_1	–	0.75
S_2	–	2
$S_{3,@0.075A \cdot cm^{-2}}$	–	0.085
$S_{3,@0.15A \cdot cm^{-2}}$	–	0.13

Table 6.1: Assumed and fitted parameters of anode polarization (MEA GM, met 3.25%wt - 1 $g \cdot min^{-1}$, 333 K, 1 bar).

Despite the calibrated anode polarization is the same of that reported in Fig.

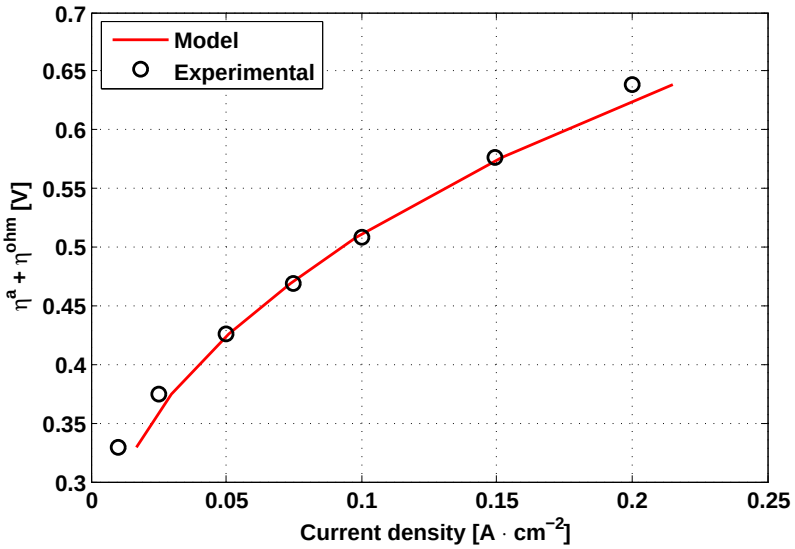

Figure 6.3: Comparison of the simulated and measured anode polarization (MEA GM, met 3.25%wt - 1 $g \cdot min^{-1}$, 333 K, 1 bar).

5.7, the resulting values of kinetic parameters are not directly comparable with those of Table 5.2. In fact not only a finite thickness electrode and proton transport losses have been introduced in the model, but also a second reaction step dependent on concentration and a detailed mass transport description through the GDL have been considered.
The resulting value of CF is lower than 1 and therefore the catalyst layer average diffusivity is lower than the diffusion layer one, coherently with reduced values of porosity and void fraction in the catalyst layer.
Regarding the calibration parameters of saturation profile at channel-GDL interface (Eq. 6.12), the values of S_1 and S_2 are quite high: this implies a very strong dependence of s_{ch-GDL} on the saturation in the channel. Fig. 6.4 reports a comparison between the simulated profile of s_{ch} and $s_{ch,GDL}$ along channel length: the saturation at the channel-GDL interface is lower than the channel one, coherently with the higher hydrophobicity of the diffusion media. Moreover it is interesting to note that S_3 increases with the current density: this implies that towards the end of the channel s_{ch-GDL} is slightly higher than s_{ch}. This behavior could be due to the higher outler flow velocity and total pressure [141], peculiar of high operating current densities. However this aspect should be further investigated by means of specific experimental and modeling analyses.
By solving the entire DMFC anode polarization model it is therefore possible to obtain the steady-state profiles along channel length and both GDL and

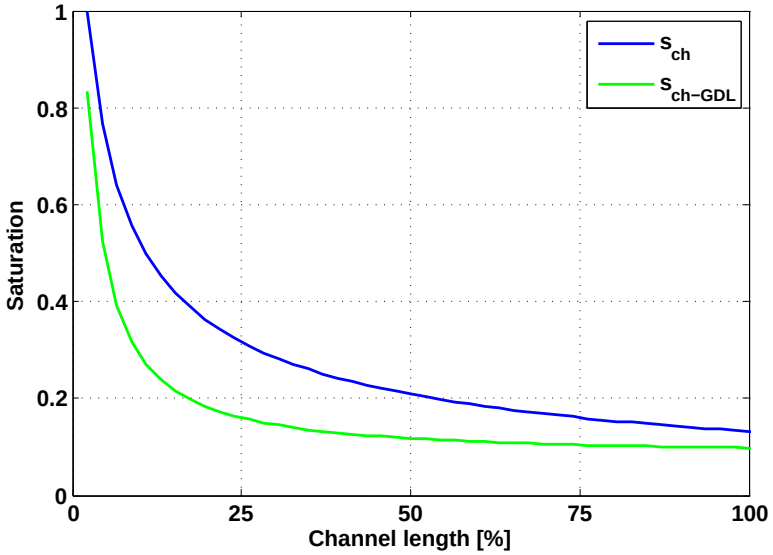

Figure 6.4: Profile of s_{ch} and s_{ch-GDL} along channel length at 0.075 $A \cdot cm^{-2}$ (MEA GM, met 3.25%wt - 1 $g \cdot min^{-1}$, 333 K, 1 bar).

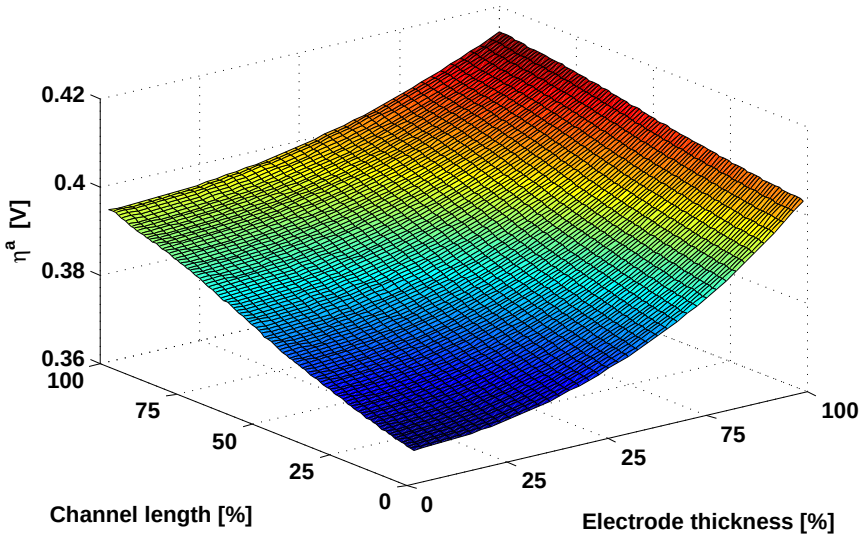

Figure 6.5: Profile of η^a along channel length and electrode thickness at 0.075 $A \cdot cm^{-2}$ (MEA GM, met 3.25%wt - 1 $g \cdot min^{-1}$, 333 K, 1 bar).

CL thickness of all the quantities necessary for the development of the physically based DMFC anode impedance model. By way of example Fig. 6.5 illustrates an anode overpotential profile along channel length and electrode thickness.

6.1.4 DMFC anode impedance model

After obtaining the stationary solution, the transient perturbation solution of the DMFC anode can be obtained in the following way. Eq. 6.2 and 6.6 are linearized about a steady-state value and subsequently each of the variables of Eq. 6.1-6.4 and 6.6-6.10 are perturbed about a steady-state value with a sufficiently low sinusoidal disturbance[3]:

$$\begin{aligned}
i(t) &= i^o + Re\{\Delta i \cdot exp\,(j \cdot \omega \cdot t)\} \\
\eta(t) &= \eta^o + Re\{\Delta \eta \cdot exp(j \cdot \omega \cdot t)\} \\
C_i(t) &= C_i^o + Re\{\Delta C_i \cdot exp(j \cdot \omega \cdot t)\} \\
N_j(t) &= N_j^o + Re\{\Delta N_j \cdot exp(j \cdot \omega \cdot t)\} \\
\gamma_{CO}(t) &= \gamma_{CO}^o + Re\{\Delta \gamma_{CO} \cdot exp(j \cdot \omega \cdot t)\} \\
s(t) &= s^o + Re\{\Delta s \cdot exp(j \cdot \omega \cdot t)\}
\end{aligned} \tag{6.22}$$

Neglecting the terms with products of the disturbances and subtracting the steady-state equations, it is possible to obtain a system of linear equations for the complex perturbation amplitudes Δi-Δs in the frequency domain [65, 66]. In particular the GDL equations 6.1-6.4 become:

$$\begin{aligned}
\frac{\partial \Delta C_{CH_3OH}^{GDL,L}}{\partial x} \cdot \left(D_{GDL,CH_3OH}^{L} \cdot s_{GDL}^{o} + \frac{D_{GDL,CH_3OH}^{G}}{K_{H,CH_3OH} \cdot R \cdot T} \cdot (1 - s_{GDL}^{o}) \right) \\
= -\Delta N_{GDL}^{CH_3OH} + \Delta N_{GDL}^{H_2O} \cdot \frac{C_{CH_3OH}^{GDL,L,o}}{C_{H_2O}^{GDL,L,o}} + N_{GDL}^{H_2O,o} \cdot \frac{\Delta C_{CH_3OH}^{GDL,L}}{C_{H_2O}^{GDL,L,o}} \\
-\Delta s_{GDL} \cdot \left(D_{GDL,CH_3OH}^{L} - \frac{D_{GDL,CH_3OH}^{G}}{K_{H,CH_3OH} \cdot R \cdot T} \right) \cdot \left. \frac{\partial C_{CH_3OH}^{GDL,L}}{\partial x} \right|^{o}
\end{aligned} \tag{6.23}$$

[3] In the following eqauations the steady-state values are denoted by the superscript ^{o}.

$$\frac{\partial \Delta s_{GDL}}{\partial x} = \left.\frac{\partial f}{\partial s_{GDL}}\right|^{o} \cdot \Delta s_{GDL} + \left.\frac{\partial f}{\partial N_{GDL}^{H_2O}}\right|^{o} \cdot \Delta N_{GDL}^{H_2O} \tag{6.24}$$

$$\begin{aligned}\frac{\partial \Delta N_{GDL}^{CH_3OH}}{\partial x} &= -j \cdot \omega \cdot \epsilon_{GDL} \cdot \left(\Delta s_{GDL} \cdot C_{CH_3OH}^{GDL,L,o} + \Delta C_{CH_3OH}^{GDL,L} \cdot s^o\right) \\ &+ j \cdot \omega \cdot \epsilon_{GDL} \cdot \left(\frac{\Delta s_{GDL} \cdot C_{CH_3OH}^{GDL,L,o} - \Delta C_{CH_3OH}^{GDL,L} + \Delta C_{CH_3OH}^{GDL,L} \cdot s^o}{K_{H,CH_3OH} \cdot R \cdot T}\right)\end{aligned} \tag{6.25}$$

$$\frac{\partial \Delta N_{GDL}^{H_2O}}{\partial x} = -j \cdot \omega \cdot \epsilon_{GDL} \cdot \left(\Delta s_{GDL} \cdot C_{H_2O}^{GDL,L,o} - \Delta s_{GDL} \cdot C_{H_2O}^{sat}\right) \tag{6.26}$$

Instead the catalyst layer equations 6.6-6.10 take the following form:

$$\begin{aligned}\frac{\partial \Delta i}{\partial x} &= \left.\frac{\partial i_1}{\partial \eta}\right|^{o} \cdot \Delta\eta + \left.\frac{\partial i_1}{\partial \bar{C}_{CH_3OH}^{t}}\right|^{o} \cdot \Delta \bar{C}_{CH_3OH}^{t} + \left.\frac{\partial i_1}{\partial \gamma_{CO}}\right|^{o} \cdot \Delta\gamma_{CO} \\ &+ \left.\frac{\partial i_2}{\partial \eta}\right|^{o} \cdot \Delta\eta + \left.\frac{\partial i_2}{\partial \bar{C}_{H_2O}^{t}}\right|^{o} \cdot \Delta \bar{C}_{H_2O}^{t} + \left.\frac{\partial i_2}{\partial \gamma_{CO}}\right|^{o} \cdot \Delta\gamma_{CO} + j \cdot \omega \cdot C_{dl} \\ &= \Delta i_1 + \Delta i_2 + j \cdot \omega \cdot C_{dl}\end{aligned} \tag{6.27}$$

$$\frac{\partial \Delta N_t^{CH_3OH}}{\partial x} = -\frac{\Delta i_1}{4 \cdot F} - j \cdot \omega \cdot \epsilon_t \cdot \Delta \bar{C}_{CH_3OH}^{t} \tag{6.28}$$

$$\frac{\partial \Delta N_t^{H_2O}}{\partial x} = -\frac{\Delta i_2}{2 \cdot F} - j \cdot \omega \cdot \epsilon_t \cdot \Delta \bar{C}_{H_2O}^{t} \tag{6.29}$$

$$-\bar{D}_{t,CH_3OH} \cdot \frac{\partial \Delta \bar{C}_{CH_3OH}^{t}}{\partial x} = \Delta N_t^{CH_3OH} \tag{6.30}$$

$$-\bar{D}_{t,H_2O} \cdot \frac{\partial \Delta \bar{C}_{H_2O}^{t}}{\partial x} = \Delta N_t^{H_2O} \tag{6.31}$$

$$\frac{\partial \Delta\eta}{\partial x} = \frac{\Delta i}{\sigma_t} \tag{6.32}$$

$$j \cdot \omega \cdot \Delta\gamma_{CO} \cdot \Gamma_{Pt} = \frac{\Delta i_1}{4 \cdot F} - \frac{\Delta i_2}{2 \cdot F} \tag{6.33}$$

The boundary conditions to Eq. 6.23-6.33 are as following:

$$\Delta\eta|_{GDL-el} = \eta_{EIS} \tag{6.34}$$

$$\Delta i|_{GDL-el} = 0 \tag{6.35}$$

$$\Delta C_{CH_3OH}|_{ch-GDL} = 0 \qquad \Delta C_{H_2O}|_{ch-GDL} = 0 \tag{6.36}$$

$$\Delta N^{CH_3OH}|_{el-m} = \Delta N^{CH_3OH}_{m,drag} \qquad \Delta N^{H_2O}|_{el-m} = \Delta N^{H_2O}_{m,drag} \tag{6.37}$$

Eq. 6.34 establishes a small amplitude perturbation at GDL-CL interface. As demonstrated in [10], the system of Eq. 6.23-6.33 is linear and homogenous and the impedance does not depend on the amplitude of this boundary condition. Instead Eq. 6.35 means zero proton current at the GDL-CL interface. Eq. 6.36 expresses zero disturbance of methanol and water concentration at channel-GDL interface, respectively. This implies that the concentration in the channel remains unperturbed by the change in overpotential: considering the high liquid accumulation in the channel, that is present for all the perturbation frequencies, this is a reasonable assumption.
Since the membrane is permeable to both methanol and water, the oscillation of the corresponding flux at the membrane interface cannot be assumed equal to zero. As reported in the 1D+1D DMFC model of chapter 3, water cross-over flux is due to three transport mechanisms: electro-osmotic drag and liquid diffusion and convection. Instead, the methanol cross-over flux is only governed by electro-osmotic drag and liquid diffusion. The contributions of liquid diffusion and convection are influenced by the corresponding concentration and pressure at the cathode side, that during dynamic operation are difficult to determine with a reduced uncertainty. Considering also the considerable accumulation in the membrane, Eq. 6.37 imposes that the disturbance of methanol and water flux is equal only to the oscillation of drag component.
Finally the impedance of the anode can be numerically calculated with Eq. 5.3. Furthermore, considering all the steady-state profiles obtained by the DMFC anode polarization model, it is possible to calculate the local value of DMFC impedance along channel length. Thus the total impedance is equal to the parallel between each local impedance, given by Eq. 5.39.

6.2 Modeling results

The system of Eq. 6.23-6.33, along with the boundary conditions Eq. 6.34-6.37, is solved in Matlab® environment. In particular the FSOLVE function solves the CL equations (Eq. 6.27-6.33) by iteratively changing the value of the oscillatory fluxes at electrode inlet till the boundary conditions (Eq. 6.37) are fulfilled. At the same time these fluxes are imposed, together with Eq. 6.36, as boundary conditions in a BVP function, that solves the GDL equations (Eq. 6.23-6.26). In this way all the boundary conditions reported in Eq. 6.34-6.37 are simultaneously satisfied and the iterations are performed by means of an optimized built in function, increasing the numerical stability of the problem.

6.2.1 Reference operating condition

The developed model has been firstly validated on the same anode impedance of paragraph 5.3.3, performed on MEA GM at 333 K, with a methanol concentration and flow rate equal to 3.25%wt and 1 $g \cdot min^{-1}$, respectively. All the kinetic and transport parameters necessary for the calculation of DMFC anode spectrum have been previously obtained from the calibration of DMFC anode polarization model on the corresponding experimental data (Table 6.1); while the value of the double layer capacitance, active site density and porosities have been assumed, Table 6.2.

C_{dl}	$F \cdot cm^{-3}$	30
Γ_{Pt}	$mol \cdot cm^{-3}$	$1 \cdot 10^{-3}$
ϵ_t	–	0.12
ϵ_{GDL}	–	0.6

Table 6.2: Assumed parameters of anode impedance (MEA GM, met 3.25%wt - 1 $g \cdot min^{-1}$, 333 K, 1bar).

Fig. 6.6 reports the simulated Nyquist plot at 0.075 $A \cdot cm^{-2}$. The model

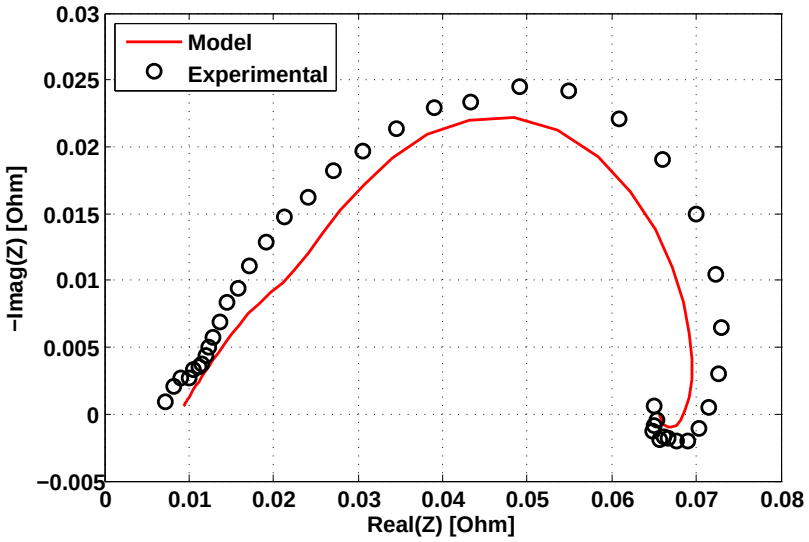

Figure 6.6: Simulated and measured anode Nyquist plot at 0.075 $A \cdot cm^{-2}$ (MEA GM, met 3.25%wt - 1 $g \cdot min^{-1}$, 333 K, 1 bar).

reproduces experimental observations with sufficient accuracy and it is possible to notice the presence of the linear branch due to the proton transport

limitations in the electrode. Moreover the detailed mass transport description of both methanol and water fluxes through the anode GDL, without the simplifying assumption of Nernst stagnant diffusion, provides a more accurate estimation of the mass transport impedance; in fact the total resistance is close to the experimental value.
Fig. 6.7 illustrates the Bode plot at 0.075 $A \cdot cm^{-2}$: there is full agreement between model and experiment and therefore all the processes are correctly described.

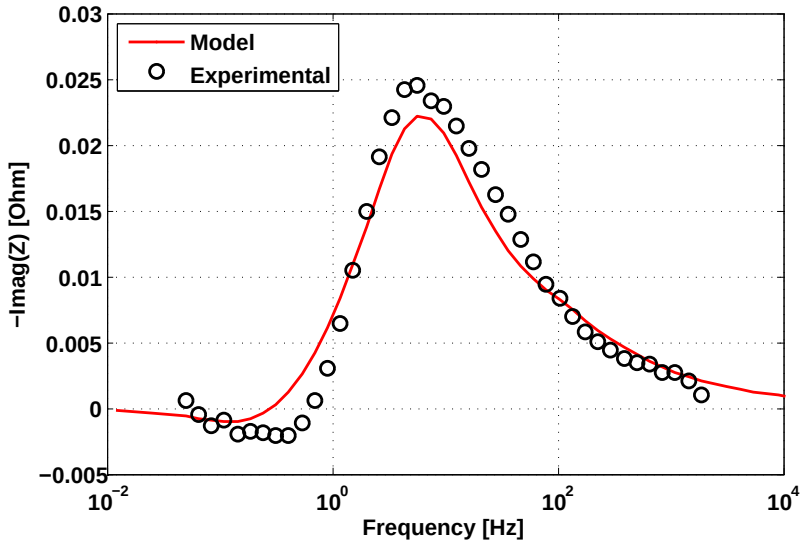

Figure 6.7: Simulated and measured anode Bode plot at 0.075 $A \cdot cm^{-2}$ (MEA GM, met 3.25%wt - 1 $g \cdot min^{-1}$, 333 K, 1 bar).

It is very important to figure out that the developed model is also able to reproduce DMFC operating current with high accuracy: in fact the simulated value of current density, equal to 0.074 $A \cdot cm^{-2}$, is almost identical to the experimental one. This is a very important feature because it would be possible to obtain more accurate impedance simulations by slightly changing few physical parameters, but in this case the DMFC operating current would be rather different from the experimental one. An example is reported in Fig. 6.8: increasing by 2% the Tafel slope of the first reaction step, model simulates experimental data with higher accuracy, but the model output current density is equal to 0.071 $A \cdot cm^{-2}$.
In Fig. 6.9, the blue line shows impedance simulations performed with the assumption that GDL is always flooded with fully liquid pathways: therefore GDL liquid accumulation terms dampen the oscillations of concentrations for all the perturbation frequencies. Model predictions are inconsistent with the

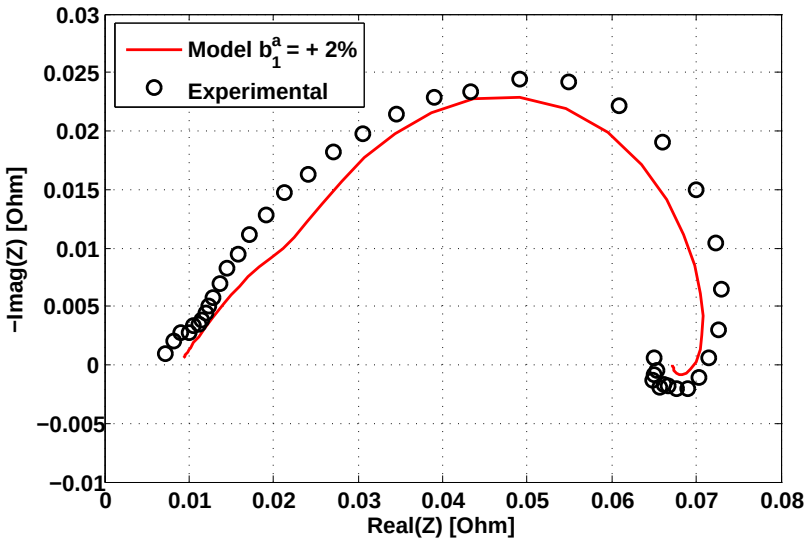

Figure 6.8: Simulated anode Nyquist plot at 0.075 $A \cdot cm^{-2}$ obtained by increasing b_1^a by 2% (MEA GM, met 3.25%wt - 1 $g \cdot min^{-1}$, 333 K, 1 bar).

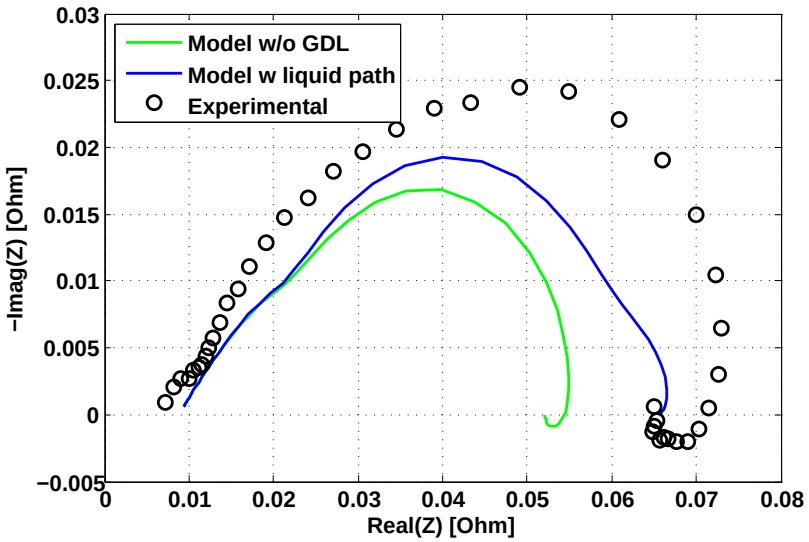

Figure 6.9: Simulated anode Nyquist plot at 0.075 $A \cdot cm^{-2}$ without the assumption of intermittent permeation and without the effect of GDL (MEA GM, met 3.25%wt - 1 $g \cdot min^{-1}$, 333 K, 1 bar).

experimental data and this is a further confirmation that liquid convection through the GDL is an intermittent phenomenon.
Instead the green line in Fig. 6.9 represents impedance simulations without the effect of the GDL: therefore the concentration disturbances at the GDL-CL interface are null and the fluxes are not affected by the GDL accumulation terms. Even at low current density GDL has a relevant influence on impedance behavior. This result is considerable different from that reported in Fig. 5.11, in which the mass transfer impedance is almost negligible.
Fig. 6.10 reports a comparison between model results with and without the implementation of GDL effects along channel length. It is evident that at the end of channel the mass transport losses due to the presence of GDL are more pronounced, as expected. Moreover, also the magnitude of inductive loop increases towards the end of the channel, coherently with the results of the preliminary impedance model, Fig. 5.12.

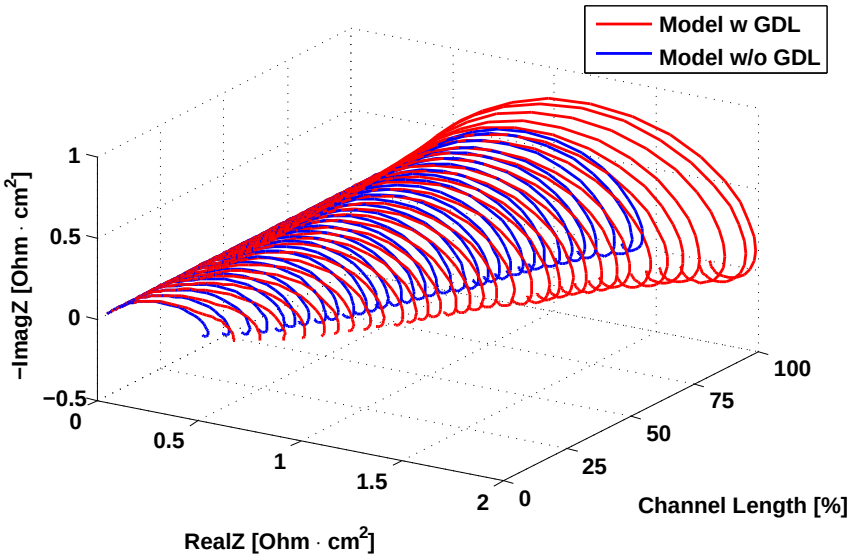

Figure 6.10: Simulated anode Nyquist plot along channel length at 0.075 $A \cdot cm^{-2}$ with and without GDL effects (MEA GM, met 3.25%wt - 1 $g \cdot min^{-1}$, 333 K, 1 bar).

Hereinafter a specific analysis is performed in order to evaluate the effects of the boundary conditions regarding the oscillating fluxes at the electrode-membrane interface. From Fig. 6.11 it is possible to figure out that these boundary conditions affect impedance features in the low-medium frequencies region. In particular $\Delta N^{H_2O}|_{el-m} = 0$ implies an increase of the total resistance and a reduction of inductive behavior, while $\Delta N^{CH_3OH}|_{el-m} = 0$ has the opposite effect. However all the physical phenomena are intercon-

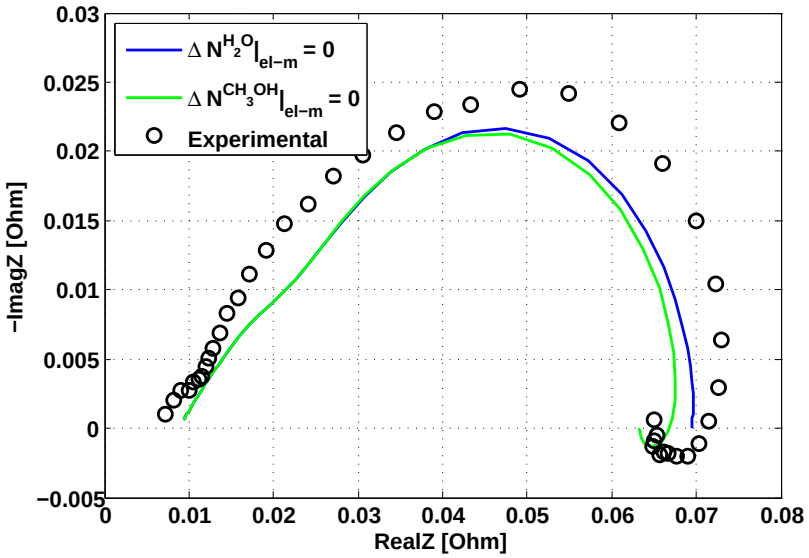

Figure 6.11: Simulated anode Nyquist plot at 0.075 $A \cdot cm^{-2}$ with $\Delta N^{H_2O}|_{el-m} = 0$ and $\Delta N^{CH_3OH}|_{el-m} = 0$ (MEA GM, met 3.25%wt - 1 $g \cdot min^{-1}$, 333 K, 1 bar).

nected: switching off certain physical phenomena may affect the impedance behavior of other physical processes and therefore it is not easy to find out the origin of these different impedance features. However these effects seem to be related to a variation of both water and methanol concentrations in the electrode. This is a further confirmation of the complexity of DMFC anode impedance modeling and therefore the previous model validation on three different typologies of measure at the same time was fundamental to simulate impedance data with high accuracy.

6.2.2 Effect of current density

Doubling the current density the model reproduces experimental observations with sufficient accuracy, Fig. 6.12: the inductive behavior is no longer present and mass transport limitations seem to appear in the low frequency region. However the model slightly overestimates the total resistance.
In Fig. 6.12, the simulations without the effect of GDL (green line) are considerable different from the experimental observations. As expected, at high current density mass transport losses are more relevant than that at low current density, Fig. 6.9.
Instead the blue line represents the effects of fully liquid pathways in the GDL: once again the model predictions are inconsistent with experimental

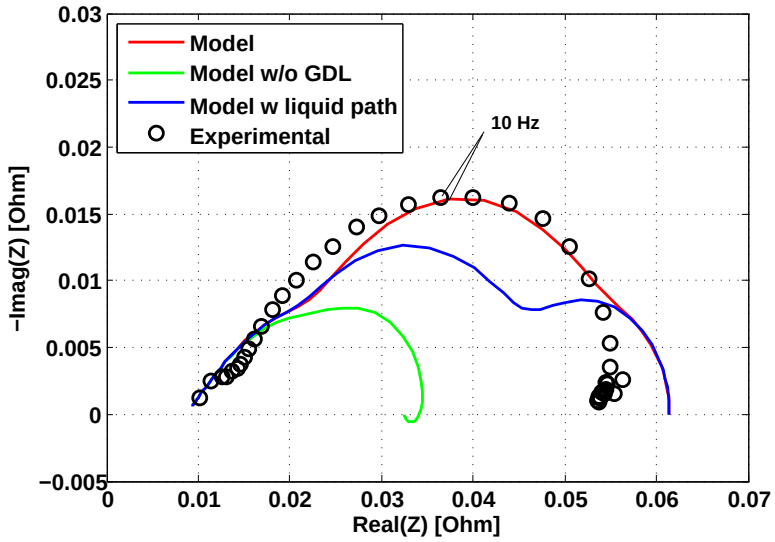

Figure 6.12: Simulated and measured anode Nyquist plot at 0.15 $A \cdot cm^{-2}$ (MEA GM, met 3.25%wt - 1 $g \cdot min^{-1}$, 333 K, 1 bar).

data. Moreover it is possible to clearly distinguish two arches: the first one characterizes kinetic losses, while the second one is peculiar of mass transport limitations. The intermittent description of liquid convection amplifies the oscillations of concentrations at GDL-CL interface for frequencies lower than 75 Hz and this leads to a superimposition of the two arches. These considerations underline the difficulties in the interpretation of DMFC anode spectra: in fact mass transport limitations do not manifest themselves as a second arch, even if their contribution is relevant.

6.2.3 Effect of anode MPL

The developed model has been further validated on IRD MEA MM impedance measurements. The fitted and assumed model parameters are reported in Table 6.3, while the parameters reported in Tables 3.1-3.4 and 6.1 still remain valid. The values of GDL diffusivity and permeability are lower compared to those of Table 6.1, coherently with the presence of anode MPL.
Impedance simulations are in good agreement with experimental data, Fig. 6.13. Despite the high operating current, the magnitude of inductive loop is comparable with that of Fig. 6.6, as already observed in the experimental analysis of paragraph 4.2.2, in which this impedance feature has been attributed to the different kinetic parameters and operating overpotential and to the presence of anode MPL.

α_1	-	0.78
i_{*v1}	$A \cdot cm^{-3}$	$1.24 \cdot 10^{-4} \cdot exp(8024 \cdot (1/353 - 1/T))$
α_2	-	0.42
i_{*v2}	$A \cdot cm^{-3}$	$4.81 \cdot 10^{-2} \cdot exp(8024 \cdot (1/353 - 1/T))$
σ_t	$\Omega^{-1} \cdot cm^{-1}$	$1.2 \cdot 10^{-2}$
D^G_{GDL,CH_3OH}	$cm^2 \cdot s^{-1}$	$1.22 \cdot 10^{-2}$
D^L_{GDL,CH_3OH}	$cm^2 \cdot s^{-1}$	$0.9 \cdot 10^{-5.4163-999.778/T} \cdot 10^4$
K_{GDL}	m^2	$0.5 \cdot 10^{-14}$
CF	–	0.5
$S_{3,@0.25A \cdot cm^{-2}}$	–	0.1
C_{dl}	$F \cdot cm^{-3}$	150
ϵ_{GDL}	–	0.5

Table 6.3: Assumed and fitted parameters of anode polarization and impedance (IRD MEA MM, met 3.25%wt - 3.87 $g \cdot min^{-1}$, 348 K, 1 bar).

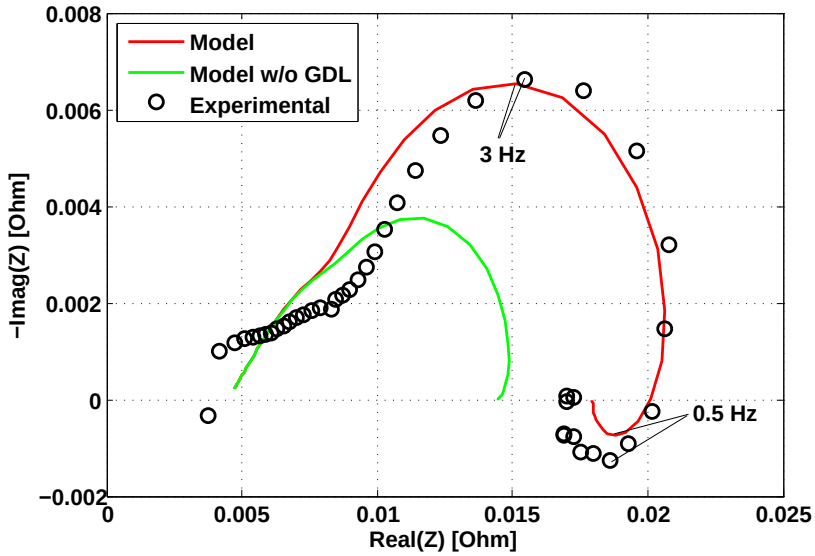

Figure 6.13: Simulated and measured anode Nyquist plot at 0.25 $A \cdot cm^{-2}$ (IRD MEA MM, met 3.25%wt - 3.87 $g \cdot min^{-1}$, 348 K, 1 bar).

In Fig. 6.13 the green line represents impedance simulations without the effect of anode GDL and it is evident that the inductive behavior is no longer present. This consideration suggests that the presence of MPL, that increases the mass transfer resistance and therefore the oscillations of concentrations at GDL-CL interface, amplifies the phase delay between the voltage and the current, with a consequent enlargement of inductive behavior. Therefore model predictions confirm that the different magnitude of inductive loop is mainly due to the presence of anode MPL, rather than the different kinetic parameters or operating potential.

6.2.4 Effect of methanol feeding concentration

In the experimental analysis of paragraph 4.2.2, one of the most influent operating parameter turned out to be methanol feeding concentration, that significantly enlarges the inductive loop.
Fig. 6.14 illustrates simulation results obtained by doubling methanol inlet concentration. The model qualitatively reproduces the shape of impedance

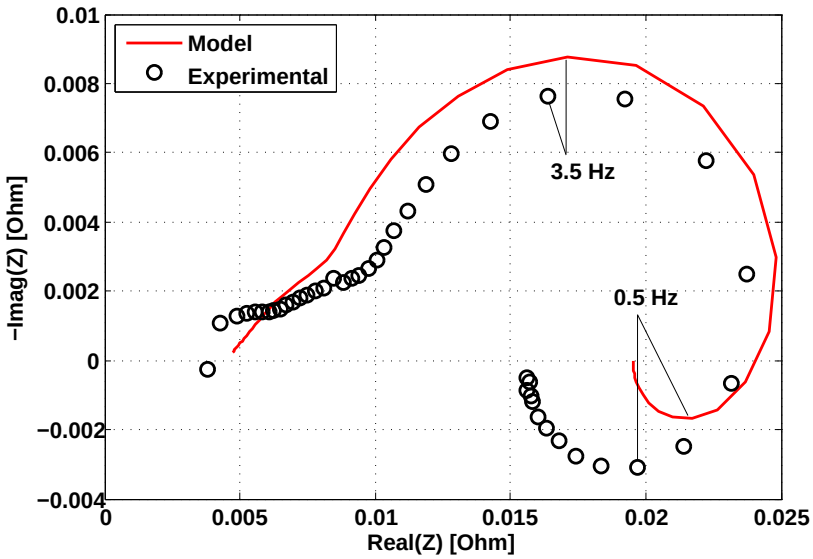

Figure 6.14: Simulated and measured anode Nyquist plot at 0.25 $A \cdot cm^{-2}$ (IRD MEA MM, met 6.5%wt - 3.87 $g \cdot min^{-1}$, 348 K, 1 bar).

spectrum: in fact the magnitude of the inductive loop increases, but there is not such a considerable amplification. Moreover the simulated total resistance increases, while the experimental data evidence a reduction of this parameter, Fig. 6.13. Therefore the model is not sufficiently accurate to predict the effects of methanol concentration on anode impedance spectrum. A

possible reason could be due to the channel methanol concentration influence on saturation profile in the GDL, that is not described in the present model and affects methanol and water concentrations within the electrode.

6.3 Model application to degradation study

The developed impedance model has been finally used as a diagnostic tool to investigate the origins of some anodic degradation effects. In the framework of Premium Act project [60], the MRT Fuel Cell Lab of Politecnico di Milano has carried out several anodic degradation tests, in order to elucidate the effects of operating conditions on the overall degradation rate, defined as the ratio between the total voltage loss and the test duration. But in this way, the comprehension of the possible origins of degradation is still hindered.
In a durability test, the only way to continuously monitor system internal losses is the EIS and therefore the developed model is suitable to increase the understanding of anodic degradation effects. In this paragraph a 100 hours degradation test has been analyzed; the recorded spectra, published in [142] and reported in Fig. 6.15 with the permission of authors, show in the first 30 hours an extension of the linear branch, a reduction of inductive loop and an increase of the total resistance; while in the next 70 hours the spectra are almost superimposed.

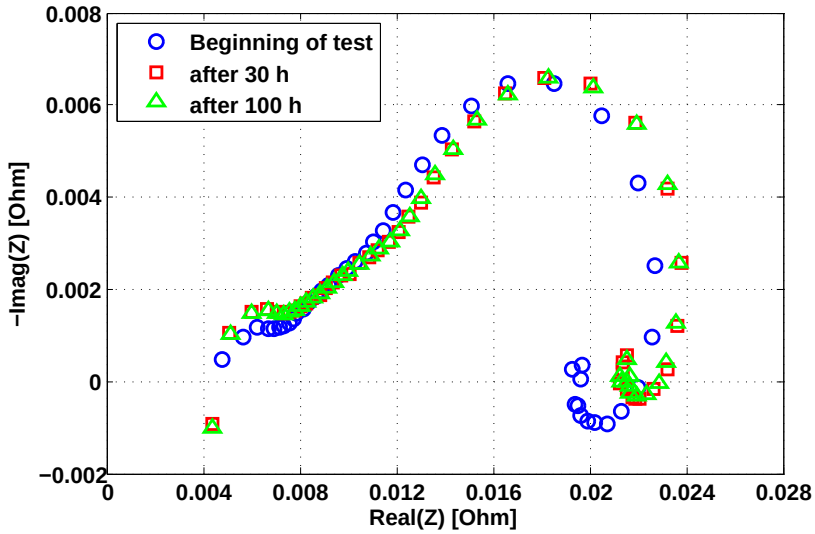

Figure 6.15: Measured anode Nyquist plot during a degradation test at 0.25 $A \cdot cm^{-2}$ (IRD MEA MM, met 3.25%wt - 3.87 $g \cdot min^{-1}$, 348 K, 1 bar).

Finally, after operation interruption, the anode spectrum is nearly the same

of that recorded at the beginning of the test: this implies that the degradation is recoverable and for this reason it is named temporary. This feature is coherent with the time-voltage curve, that after operation interruption returns to the initial value.
Moreover during the durability test also continuous measurements of methanol cross-over and water flux at cathode outlet have been performed[4]. These mass transport measurements evidence a reduction of both the fluxes in the first 50 hours, that can be respectively associated with a decrease of methanol and water concentrations in the anode catalyst layer. Therefore it is plausible to proposed the following origin of degradation effects on impedance features:

- the extension of linear branch might be due to catalyst layer dehydration, that lowers proton transport conductivity;
- the increase of total resistance and the decrease of inductive behavior might be caused by a reduction of methanol concentration in the catalyst layer, that enhances mass transport limitations.

Integrating these effects in the model the simulations qualitatively reproduce experimental observations, Fig. 6.16. Therefore this is a further confirmation of the proposed origins of temporary degradation effects. However, in order

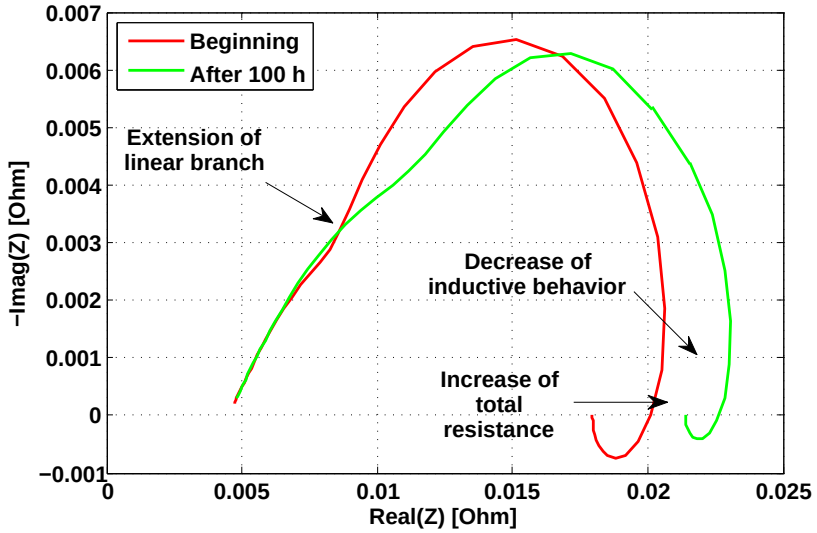

Figure 6.16: Simulated Nyquist plots with temporary degradation effects.

[4]These mass transport measurements, along with the time-voltage curve, are part of another PhD dissertation and are not yet published: for this reason they are not reported.

to increase the reliability of the results and to provide an insight into the understanding of all the phenomena worsening DMFC operation, the model has to be applied to several degradation tests. The one reported in this paragraph is only an example to illustrate the potentialities of the developed DMFC anode impedance model.

6.4 Remarks

In this chapter a detailed description of mass transport phenomena through diffusion layer and an electrode of finite thickness have been introduced in the anode polarization model of paragraph 5.3.1 and subsequently a physical model of anode impedance has been developed. The main conclusions regarding DMFC anode impedance behavior are the following:

- Proton transport limitations through the electrode manifest themselves as a 45^o linear branch at high frequencies.
- The intermittent description of liquid convection through GDL entails that liquid accumulation terms dampen the oscillations of concentrations only for perturbation frequencies higher than 75 Hz. This assumption implies a superimposition between the arches peculiar of kinetic and mass transport losses and it is of fundamental importance to correctly simulate anode impedance features.
- The contribution of GDL to the impedance is relevant even at low current density and increases along channel length, as expected.
- The magnitude of inductive loop increases along channel length, coherently with the results of paragraph 5.3.3.
- Doubling the operating current density the effect of GDL is predominant and in fact without the assumption of intermittent permeation it is possible to clearly distinguish a second arch, peculiar of mass transport limitations.
- The presence of anode MPL increases the mass transfer resistance through the GDL and therefore the oscillations of concentrations at GDL-CL interface, amplifying the phase delay between the voltage and the current. As a consequence an enlargement of inductive loop is evident in the impedance spectrum.
- Doubling methanol inlet concentration an increase of inductive loop is evident. However the developed model reproduces this feature only

qualitatively: in fact the magnitude of the inductive loop increases, but the experimental data exhibit a more considerable enlargement. Moreover the simulated total resistance increases, while the experimental data show the opposite behavior.

- Model predictions confirm the possible origins of the following temporary degradation effects: the extension of linear branch is due to catalyst layer dehydration, that lowers proton transport conductivity, while the increase of total resistance and the decrease of inductive behavior are caused by a reduction of methanol concentration in the catalyst layer, that enhances mass transport limitations.

Conclusions

This work reports a combined experimental and modeling analysis of mass transport phenomena and electrochemical impedance spectroscopy in DMFC. The first objective of the work is to increase and consolidate the understanding of the phenomena governing DMFC water transport. This is firstly achieved by a systematic experimental analysis of operating conditions and GDL configurations influence on water flux at cathode outlet, methanol cross-over and performance. This analysis evidences that the water removal from the cathode GDL is regulated by two different transport mechanisms: gas diffusion and liquid permeation. The former determines a plateau at low current densities, the latter a linear trend at high current densities. The absence of cathode MPL causes a general increase of water flow at cathode outlet, that favors methanol cross-over. Moreover the higher cathode oxygen diffusivity generally enhances DMFC performances, but some exceptions are evident, probably due to cathode flooding phenomenon. Instead the presence of anode MPL implies a reduction of both the water flow at cathode outlet and methanol concentration at the anode. As a consequence the DMFC exhibits both lower performances and methanol cross-over. Influence of temperature, pressure and airflow confirms the expectations.
Subsequently, in order to validate the interpretation of water management and its impact on performance and methanol crossover, a 1D+1D DMFC model has been developed. In particular the model includes a detailed description of water transport through the MEA and two correlations to take into account flooding effects. Moreover it has been validated on three different typologies of measure at the same time over a wide range of operating conditions, providing an exhaustive interpretation of the mechanisms regu-

lating water transport and flooding phenomena. Model simulations confirm that water diffusion through cathode GDL is regulated by vapor concentration gradient, while liquid water permeation through cathode GDL occurs when water pressure exceeds a threshold value, related to GDL characteristics; the permeation linear trend with current density is due to electro-osmotic drag and water production at cathode electrode. The presence of a liquid water barrier to the anode (i.e., the MPL) strongly reduces water cross-over through the membrane and as a consequence liquid permeation through cathode GDL does not occur and water vapor concentration in cathode electrode significantly decreases.
Moreover the developed model is able to predict water fluxes through the membrane. Liquid water diffusion through the membrane is usually directed from anode to cathode and at low current densities it is the predominant water transport mechanism, but the presence of anode MPL causes an inversion of liquid diffusion flux at high current densities. However the total water cross-over flux is always directed from anode to cathode. Instead liquid permeation through the membrane is directed from cathode to anode, but its contribution is negligible. High water cross-over may cause cathode flooding. To reproduce its effects two mechanisms have been introduced in the model, giving comparable contributions: superficial and bulk pores obstructions. The first is proportional to liquid water concentration in cathode channel; the latter is proportional to liquid water permeation. In particular a correlation to reproduce bulk pores obstruction is proposed for two cathode GDLs, with and without MPL; the magnitude of bulk obstruction effect results more relevant without cathode MPL. Therefore the addition of the MPL on cathode GDL increases the mass transfer resistance, causing a performance decrease when no flooding occurs, while performance increases with severe flooding, because the MPL limits its effect.
The proposed combined experimental and modeling analysis of water transport provides an exhaustive characterization of DMFC operation and it is the starting point to delve into the interaction between all the physicochemical phenomena of DMFC, that are characterized by EIS measurements. In fact the second objective of this work is to provide an insight into the basic principles regulating DMFC impedance behavior. Similarly to what was done before, this is firstly achieved by a systematic experimental investigation. The analysis of anode and cathode impedance elucidates the main relevant phenomena governing DMFC impedance behavior and provides an insight into the development of interpretation models.
The cathode spectra are often an almost ideal or slightly elongated semicircle, in which mass transport limitations are not evident. However at high current density and low cathode flow rate a second arch appears and it is considerably

enlarged by increased methanol cross-over. Instead the anode spectra exhibit a high frequency linear branch, due to proton transport limitations through the catalyst layer, and present also an inductive loop, peculiar of a reaction dependent on surface coverage by absorbed intermediates. The magnitude of inductive loop is strongly enlarged by increased methanol concentration and probably by the presence of anode MPL. On the contrary the inductive behavior disappears when mass transport limitations occur, usually at high current density and low methanol concentration.
Subsequently, in order to provide a quantitative interpretation of experimental observations, a preliminary DMFC impedance model has been developed. In particular an existing approach has been adapted to DMFC technology and locally integrated in the previous 1D+1D DMFC model. The developed interpretation model is more reliable than the classic equivalent circuit method because the equivalent circuit elements are function of the physical parameters of the system, obtained from the validation of the 1D+1D DMFC model. Moreover by means of the developed approach it is possible to calculate the local values of equivalent circuit elements, providing an insight into the understanding of internal DMFC losses.
Despite the Nernst hypothesis, cathode simulations reproduce experimental observations with good accuracy. In the investigated operating conditions the kinetic losses are usually higher than mass transfer ones and both the local values of charge transfer resistance and the real part of mass transfer impedance increase along channel length, coherently with a reduction of current density and oxygen concentration, respectively. Moreover cathode impedance model qualitatively reproduces the effect of a poor oxygen concentration in the electrode: at high current density a second arch is evident in the low frequency region. This arch, peculiar of mass transport limitations, is enlarged by reduced cathode flow rate and increased methanol concentration, coherently with the experimental observations.
Instead the anode simulations reproduce inductive behavior with high accuracy, but the model does not take into account proton transport limitations and therefore the simulated spectrum is not an elongated semicircle. Moreover the simplified two-phase mass transport description through anode GDL, along with the Nernst hypothesis, are not sufficiently accurate to calculate mass transfer impedance.
Since the preliminary modeling approach showed good agreement with experimental data of cathode impedance, but the anodic one presents the above mentioned limits, a physical model of anode impedance has been developed. In particular proton transport in a catalyst layer of finite thickness and a detailed description of mass transport phenomena through diffusion layer have been introduced in the 1D+1D DMFC model and subsequently a phys-

ical model of anode impedance has been developed. The developed model permits to further investigate mass transport mechanisms through anode diffusion layer. In fact the intermittent description of liquid permeation through GDL, that entails that liquid accumulation terms dampen the oscillations of concentrations only for perturbation frequencies higher than 75 Hz, is of fundamental importance to correctly simulate anode impedance features.
The model evidences that proton transport limitations manifest themselves as a high-frequency 45^o linear branch and that the contribution of GDL is relevant even at low current density and increases with the operating current and along channel length, as expected. Moreover simulation results highlight that the presence of MPL amplifies the phase delay between the voltage and the current, with a consequent enlargement of inductive loop. However the model is not able, yet, to reproduce accurately the effect of methanol concentration on inductive loop: in fact doubling methanol inlet concentration the magnitude of the inductive loop increases, but the experimental data exhibit a more considerable enlargement. Finally the developed model has been used as a diagnostic tool to investigate the possible origins of few temporary degradation effects. Model predictions suggest that the extension of linear branch is due to catalyst layer dehydration, while the increase of total resistance and the decrease of inductive behavior are caused by a reduction of methanol concentration in the catalyst layer.
In conclusion this work fulfils the proposed objective: to provide a deeper understanding of the basic principles regulating water transport and impedance behavior in DMFC. Particularly original and interesting are both the 1D+1D DMFC water transport model and the physically based anode impedance model. The former has been validated on three different typologies of measure at the same time over a wide range of operating conditions and therefore consolidates the proposed interpretations of water management and flooding effects. The latter provides a solid interpretation of DMFC anode impedance and can be used as a diagnostic tool to investigate anodic degradation effects.

Bibliography

[1] T. Schultz, S. Zhou, K. Sundmacher. *Current status of and recent developments in the direct methanol fuel cell.* Chemical Engineering and Technology 24 (2001) 1223-1233.

[2] S. Wasmus, A. Küver. *Methanol oxidation and direct methanol fuel cells: a selective review.* Journal of Electroanalytical Chemistry 461 (1999) 14-31.

[3] V. Neburchilov, J. Martin, H. Wang, J. Zhang. *A review of polymer electrolyte membranes for direct methanol fuel cells.* Journal of Power Sources 169 (2007) 221-238.

[4] X.Ren, W.Henderson, S.Gottesfeld. *Electro-osmotic drag of water in ionomeric membranes.* Journal of the Electrochemical Society 144 (1997) L267-L270.

[5] T.A. Zawodzinski, C. Derouin, S. Radzinski, R.J. Sherman, et al. *Water uptake by and transport through Nafion 117 membranes.* Journal of the Electrochemical Society 140 (1993) 1041-1047.

[6] S. Litster, G. McLean. *PEM fuel cell electrodes.* Journal of Power Sources 130 (2004) 61-76.

[7] S. Park, J.W. Lee, B.N. Popov. *A review of gas diffusion layer in PEM fuel cells: materials and designs.* International Journal of Hydrogen Energy 37 (2012) 5850-5865.

[8] C.E. Shaffer, C.Y. Wang. *Role of hydrophobic anode MPL in controlling water crossover in DMFC.* Electrochimica Acta 54 (2009) 5761-5769.

[9] H. Li, Y. Tang, Z. Wang, Z. Shi, et al. *A review of water flooding issues in the proton exchange membrane fuel cell.* Journal of Power Sources 178 (2008) 103-117.

[10] A.A. Kulikovsky. *Analytical modelling of fuel cells.* Elsevier 2010.

[11] D. Gerteisen. *Transient and steady-state analysis of catalyst poisoning and mixed potential formation in direct methanol fuel cells*. Journal of Power Sources 195 (2010) 6719-6731.

[12] M.R. Shivhare, C.L. Jackson, K. Scott, E.B. Martin. *Simplified model for the direct methanol fuel cell anode*. Journal of Power Sources 173 (2007) 240-248.

[13] J.P. Meyers, J. Newman. *Simulation of the direct methanol fuel cell. II. Modeling and data analysis of transport and kinetic phenomena*. Journal of The Electrochemical Society 149 (2002) A718-A728.

[14] K. Scott, P. Argyropoulos. *A one dimensional model of a methanol fuel cell anode*. Journal of Power Sources 137 (2004) 228-238.

[15] A.S. Aricò, S. Srinivasan, V. Antonucci. *DMFCs: from fundamental aspects to technology development*. Fuel Cells 1 (2001) 133-161.

[16] A.S. Aricò, P. Creti, E. Modica, G. Monforte, et al. *Investigation of direct methanol fuel cells based on unsupported Pt-Ru anode catalysts with different chemical properties*. Electrochimica Acta 45 (2000) 4319-4328.

[17] X. Ren, P. Zelenay, S. Thomas, J. Davey, S. Gottesfeld. *Recent advances in direct methanol fuel cells at Los Alamos National Laboratory*. Journal of Power Sources 86 (2000) 111-116.

[18] M. Ahmed, I. Dincer. *A review on methanol crossover in direct methanol fuel cells: challenges and achievements*. International Journal of Energy Research 35 (2011) 1213-1228.

[19] X. Ren, T.E. Springer, T.A. Zawodzinski, S. Gottesfeld. *Methanol transport through Nafion membranes. Electro-osmotic drag effects on potential step measurements*. Journal of The Electrochemical Society 147 (2000) 466-474.

[20] A. Heinzel, V.M. Barragàn. *A review of the state of the art of the methanol crossover in direct methanol fuel cells*. Journal of Power Sources 84 (1999) 70-74.

[21] Y.J. Chiu. *An algebraic semi empirical model for evaluating fuel crossover fluxes of a DMFC under various operating conditions*. International Journal of Hydrogen Energy 35 (2010) 6418-6430.

[22] S.S. Sandhu, R.O. Crowther, J.P. Fellner. *Prediction of methanol and water fluxes through a direct methanol fuel cell polymer electrolyte membrane*. Electrochimica Acta 50 (2005) 3985-3991.

[23] V. Gogel, T. Frey, Z. Yongsheng, K.A. Friedrich, et al. *Performance and methanol permeation of direct methanol fuel cells: dependence on operating conditions and on electrode structure*. Journal of Power Sources 127 (2004) 172-180.

[24] S.R. Yoon, G.H. Hwang, W.I. Cho, I.H. Oh, et al. *Modification of polymer electrolyte membranes for DMFCs using Pd films formed by sputtering*. Journal of Power Sources 106 (2002) 215-223.

[25] C. Xu, T.S. Zhao. *A new flow field design for polymer electrolyte-based fuel cells*. Electrochemistry Communications 9 (2007) 497-503.

[26] H. Yang, T.S. Zhao, Q. Ye. *In situ visualization study of CO_2 gas bubble behavior in DMFC anode flow fields*. Journal of Power Sources 139 (2005) 79-90.

[27] C. Xu, T.S. Zhao, Q. Ye. *Effect of anode backing layer on the cell performance of a direct methanol fuel cell*. Electrochimica Acta 51 (2006) 5524-5531.

[28] F. Liu, C.Y. Wang. *Water and methanol crossover in direct methanol fuel cells. Effect of anode diffusion media*. Electrochimica Acta 53 (2008) 5517-5522.

[29] C. Xu, Y.L. He, T.S. Zhao, R. Chen, Q. Ye. *Analysis of mass transport of methanol at the anode of a direct methanol fuel cell*. Journal of The Electrochemical Society 153 (2006) A1358-A1364.

[30] S. Kang, S.J. Lee, H. Chang. *Mass balance in a direct methanol fuel cell*. Journal of The Electrochemical Society 154 (2007) B1179-B1185.

[31] M. Möst, M. Rzepka, U. Stimming. *Analysis of the diffusive mass transport in the anode side porous backing layer of a direct methanol fuel cell*. Journal of Power Sources 191 (2009) 456-464.

[32] A. Blum, T. Duvdevani, M. Philosoph, N. Rudoy, E. Peled. *Water-neutral micro direct methanol fuel cell (DMFC) for portable applications*. Journal of Power Sources 117 (2003) 22-25.

[33] G.Q. Lu, C.Y. Wang. *Electrochemical and flow characterization of a direct methanol fuel cell*. Journal of Power Sources 134 (2004) 33-40.

[34] H. Kim, J. Oh, J. Kim, H. Chang. *Membrane electrode assembly for passive direct methanol fuel cells*. Journal of Power Sources 162 (2006) 497-501.

[35] C. Xu, T.S. Zhao. *In situ measurements of water crossover through the membrane for direct methanol fuel cells*. Journal of Power Sources 168 (2007) 143-153.

[36] E. Peled, A. Blum, A. Aharon, M. Philosoph, Y. Lavi. *Novel approach to recycling water and reducing water loss in DMFCs*. Electrochemical and Solid State Letters 6 (2003) A268-A271.

[37] T. Mennola, M. Noponen, T. Kallio, M. Mikkola, T. Hottinen. *Water balance in a free-breathing polymer electrolyte membrane fuel cell*. Journal of Applied Electrochemistry 34 (2004) 31-36.

[38] S. Ge, B. Yi, P. Ming. *Experimental determination of electro osmotic drag coefficient in Nafion membrane for fuel cells*. Journal of The Electrochemical Society 153 (2006) A1443-A1450.

[39] B.S. Pivovar. *An overview of electro-osmosis in fuel cell polymer electrolytes*. Polymer 47 (2006) 4194-4202.

[40] J. St-Pierre. *Simple mathematical model for water diffusion in Nafion membranes*. Journal of The Electrochemical Society 154 (2007) B88-B95.

[41] G. Lin, T.V. Nguyen. *Effect of thickness and hydrophobic polymer content of the gas diffusion layer on electrode flooding level in a PEMFC*. Journal of The Electrochemical Society 152 (2005) A1942-A1948.

[42] T. Schultz, K. Sundmacher. *Mass, charge and energy transport phenomena in a polymer electrolyte membrane (PEM) used in a direct methanol fuel cell (DMFC): modelling and experimental validation of fluxes*. Journal of Membrane Science 276 (2006) 272-285.

[43] Q. Yan, H. Toghiani, J. Wu. *Investigation of water transport through membrane in a PEM fuel cell by water balance experiments*. Journal of Power Sources 158 (2006) 316-325.

[44] Q.X. Wu, T.S. Zhao, W.W. Yang. *Effect of the cathode gas diffusion layer on the water transport behavior and the performance of passive direct methanol fuel cells operating with neat methanol*. International Journal of Heat and Mass Transfer 54 (2011) 1132-1143.

[45] W.W. Yang, T.S. Zhao, R. Chen, C. Xu. *An approach for determining the liquid water distribution in a liquid-feed direct methanol fuel cell.* Journal of Power Sources 190 (2009) 216-222.

[46] C. Xu, T.S. Zhao, Y.L. He. *Effect of cathode gas diffusion layer on water transport and cell performance in direct methanol fuel cells.* Journal of Power Sources 171 (2007) 268-274.

[47] Y. Tian, G. Sun, Q. Mao, Suli Wang, et al. *In situ analysis on water transport in a direct methanol fuel cell durability test.* Journal of Power Sources 185 (2008) 1015-1021.

[48] J. Prabhuram, N.N. Krishnan, B. Choi, T.H. Lim, et al. *Long-term durability test for direct methanol fuel cell made of hydrocarbon membrane.* International Journal of Hydrogen Energy 35 (2010) 6924-6933.

[49] J. Liu, Z. Zhou, X. Zhao, Q. Xin. *Studies on performance degradation of a direct methanol fuel cell (DMFC) in life test.* Physical Chemistry Chemical Physics 6 (2004) 134-137.

[50] Z.B. Wang, H. Rivera, X.P. Wang, H.X. Zhang, et al. *Catalyst failure analysis of a direct methanol fuel cell membrane electrode assembly.* Journal of Power Sources 177 (2008) 386-392.

[51] S.D. Knights, K.M. Colbow, J. St-Pierre, D.P.Wilkinson. *Aging mechanisms and lifetime of PEFC and DMFC.* Journal of Power Sources 127 (2004) 127-134.

[52] H.C. Cha, C.Y. Chen, J.Y. Shiu. *Investigation on the durability of direct methanol fuel cells.* Journal of Power Sources 192 (2009) 451-456.

[53] W. Chen, G. Sun, J. Guo, X. Zhao, et al. *Test on the degradation of direct methanol fuel cell.* Electrochimica Acta 51 (2006) 2391-2399.

[54] J.Y. Park, J.H. Lee, J. Sauk, I. Son. *The operating mode dependence on electrochemical performance degradation of direct methanol fuel cells.* International Journal of Hydorgen Energy 33 (2008) 4833-4843.

[55] M.K. Jeon, J.Y. Won, K.S. Oh, K.R. Lee, S.I. Woo. *Performance degradation study of a direct methanol fuel cell by electrochemical impedance spectroscopy.* Electrochimica Acta 53 (2007) 447-452.

[56] M.K. Jeon, K.R. Lee, K.S. Oh, D.S. Hong, et al. *Current density dependence on performance degradation of direct methanol fuel cells.* Journal of Power Sources 158 (2006) 1344-1347.

[57] L.S. Sarma, C.H. Chen, G.R. Wang, K.L. Hsueh, et al. *Investigations of direct methanol fuel cell (DMFC) fading mechanisms*. Journal of Power Sources 167 (2007) 358-365.

[58] P. Liu, G.P. Yin, K.D. Cai. *Investigation on cathode degradation of direct methanol fuel cell*. Electrochimica Acta 54 (2009) 6178-6183.

[59] European Project *DECODE: degradation mechanisms to improve components and design*.

[60] European Project *Premium Act: predictive modelling for innovative unit management and accelerated testing procedures of PEFC*.

[61] E. Barsoukov, J.R. Macdonald. *Impedance spectroscopy. Theory, experiment, and applications*. Wiley 2005.

[62] A.A. Kulikovsky. *Model of the flow with bubbles in the anode channel and performance of a direct methanol fuel cell*. Electrochemistry Communications 7 (2005) 237-243.

[63] A.A. Kulikovsky. *Two-dimensional numerical modelling of a direct methanol fuel cell*. Journal of Applied Electrochemistry 30 (2000) 1005-1014.

[64] J. Divisek, J. Fuhrmann, K. Gärtner, R. Jung. *Performance Modeling of a Direct Methanol Fuel Cell*. Journal of The Electrochemical Society 150 (2003) A811-A825.

[65] A.A. Kulikovsky. *A physical model for catalyst layer impedance*. Journal of Electroanalytical Chemistry 669 (2012) 28-34.

[66] A.A. Kulikovsky. *A model for DMFC cathode impedance: the effect of methanol crossover*. Electrochemistry Communications 24 (2012) 65-68.

[67] T. Schultz, K. Sundmacher. *Rigorous dynamic model of a direct methanol fuel cell based on Maxwell-Stefan mass transport equations and a Flory-Huggins activity model: formulation and experimental validation*. Journal of Power Sources 145 (2005) 435-462.

[68] J. Ko, P. Chippar, H. Ju. *A one-dimensional, two-phase model for direct methanol fuel cells. Part I: model development and parametric study*. Energy 35 (2010) 2149-2159.

[69] W.W. Yang, T.S. Zhao. *A two-dimensional, two-phase mass transport model for liquid-feed DMFCs*. Electrochimica Acta 52 (2007) 6125-6140.

[70] C. Xu, T.S. Zhao, W.W. Yang. *Modeling of water transport through the membrane electrode assembly for direct methanol fuel cells*. Journal of Power Sources 178 (2008) 291-308.

[71] A. Casalegno, R. Marchesi, D. Parenti. *Two-phase 1D+1D model of a DMFC: development and validation on extensive operating conditions range*. Fuel Cells 8 (2008) 37-44.

[72] A. Casalegno, R. Marchesi. *DMFC performance and methanol crossover: experimental analysis and model validation*. Journal of Power Sources 185 (2008) 318-330.

[73] A. Casalegno, R. Marchesi. *DMFC anode polarization: experimental analysis and model validation*. Journal of Power Sources 175 (2008) 372-382.

[74] U. Pasaogullari, C.Y. Wang. *Two-phase transport and the role of micro-porous layer in polymer electrolyte fuel cells*. Electrochimica Acta 49 (2004) 4359-4369.

[75] P. Piela, C. Eickes, E. Brosha, F. Garzon, P. Zelenay. *Ruthenium crossover in direct methanol fuel cell with Pt-Ru black anode*. Journal of The Electrochemical Society 151 (2004) A2053-A2059.

[76] Z.B. Wang, X.P. Wang, P.J. Zuo, B.Q. Yang, et al. *Investigation of the performance decay of anodic PtRu catalyst with working time of direct methanol fuel cells*. Journal of Power Sources 181 (2008) 93-100.

[77] N.Y. Hsu, S.C. Yen, K.T. Jeng, C.C. Chien. *Impedance studies and modeling of direct methanol fuel cell anode with interface and porous structure perspectives*. Journal of Power Sources 161 (2006) 232-239.

[78] C.Y. Du, T.S. Zhao, W.W. Yang. *Effect of methanol crossover on the cathode behavior of a DMFC: a half-cell investigation*. Electrochimica Acta 52 (2007) 5266-5271.

[79] D. Chakraborty, I. Chorkendorff, T. Johannessen. *Electrochemical impedance spectroscopy study of methanol oxidation on nanoparticulate PtRu direct methanol fuel cell anodes: kinetics and performance evaluation*. Journal of Power Sources 162 (2006) 1010-1022.

[80] N. Wagner. *Characterization of membrane electrode assemblies in polymer electrolyte fuel cells using a.c. impedance spectroscopy*. Journal of Applied Electrochemistry 32 (2002) 859-863.

[81] M.E. Orazem, B. Tribollet. *Electrochemical impedance spectroscopy*. Wiley 2008.

[82] S.K. Roy, M.E. Orazem, B. Tribollet. *Interpretation of low-frequency inductive loops in PEM fuel cells*. Journal of The Electrochemical Society 154 (2007) B1378-B1388.

[83] Y. Shi, H. Wang, N. Cai. *Direct two-dimensional electrochemical impedance spectra simulation for solid oxide fuel cell*. Journal of Power Sources 208 (2012) 24-34.

[84] A. Bieberle, L.J. Gauckler. *State-space modeling of the anodic SOFC system Ni, H_2-H_2O/YSZ*. Solid State Ionics 146 (2002) 23-41.

[85] Y. Shi, N. Cai, Z. Mao. *Simulation of EIS spectra and polarization curves based on Ni/YSZ patterned anode elementary reaction models*. International Journal of Hydrogen Energy 37 (2012) 1037-1043.

[86] J. Deseure. *Coupling RTD and EIS modelling to characterize operating non-uniformities on PEM cathodes*. Journal of Power Sources 178 (2008) 323-333.

[87] M. Eikerling, A.A. Kornyshev. *Electrochemical impedance of the cathode catalyst layer in polymer electrolyte fuel cells*. Journal of Electroanalytical Chemistry 475 (1999) 107-123.

[88] W.G. Bessler. *A new computational approach for SOFC impedance from detailed electrochemical reaction-diffusion models*. Solid State Ionics 176 (2005) 997-1011.

[89] W.G. Bessler, S. Gewies, M. Vogler. *A new framework for physically based modeling of solid oxide fuel cells*. Electrochimica Acta 53 (2007) 1782-1800.

[90] S. Gewies, W.G. Bessler. *Physically based impedance modeling of Ni/YSZ cermet anodes*. Journal of The Electrochemical Society 155 (2008) B937-B952.

[91] T.E. Springer, T.A. Zawodzinski, M.S. Wilson, S. Gottesfeld. *Characterization of polymer electrolyte fuel cells using AC impedance spectroscopy*. Journal of The Electrochemical Society 143 (1996) 587-599.

[92] A. Casalegno, C. Santoro, F. Rinaldi, R. Marchesi. *Low methanol crossover and high efficiency direct methanol fuel cell: the influence of diffusion layers*. Journal of Power Sources 196 (2011) 2669-2675.

[93] Env 13005, BIPM, IEC, IFCC, ISO, IUPAC, IUPAP, OIML, *Guide to the expression of uncertainty in measurement*, International Organization for Standardization, 1993, 1999, ISBN 92-67-10188-9.

[94] K. Jiao, X. Li. *Water transport in polymer electrolyte membrane fuel cells*. Progress in Energy and Combustion Science 37 (2011) 221-291.

[95] A. Casalegno, F. Bresciani, G. Groppi, R. Marchesi. *Flooding of the diffusion layer in a polymer electrolyte fuel cell: experimental and modelling analysis*. Journal of Power Sources 196 (2011) 10632-10639.

[96] T.S. Zhao, C. Xu, R. Chen, W.W. Yang. *Mass transport phenomena in direct methanol fuel cells*. Progress in Energy and Combustion Science 35 (2009) 275-292.

[97] S. Litster, D. Sinton, N. Djilali. *Ex situ visualization of liquid water transport in PEM fuel cell gas diffusion layers*. Journal of Power Sources 154 (2006) 95-105.

[98] G.Q. Lu, F.Q. Liu, C.Y. Wang. *Water transport through Nafion 112 membrane in DMFCs*. Electrochemical and Solid State Letters 8 (2005) A1-A4.

[99] W. Liu, C.Y. Wang. *Modeling water transport in liquid feed direct methanol fuel cells*. Journal of Power Sources 164 (2007) 189-195.

[100] M.H. Shi, J.Wang, Y.P. Chen. *Study on water transport in PEM of a direct methanol fuel cell*. Journal of Power Sources 166 (2007) 303-309.

[101] U. Pasaogullari, C.Y. Wang. *Liquid water transport in gas diffusion layer of polymer electrolyte fuel cells*. Journal of The Electrochemical Society 151 (2004) A399-A406.

[102] X. Ren, T.E. Springer, S. Gottesfeld. *Water and methanol uptakes in nafion membranes and membrane effects on direct methanol cell performance*. Journal of The Electrochemical Society 147 (2000) 92-98.

[103] A. Oedegaard, C. Hentschel. *Characterisation of a portable DMFC stack and a methanol-feeding concept*. J. Power Sources 158 (2006) 177-187.

[104] F. Meier, G. Eigenberger. *Transport parameters for the modelling of water transport in ionomer membranes for PEM-fuel cells*. Electrochimica Acta 49 (2004) 1731-1742.

[105] Z. Lu, M.M. Daino, C. Rath, S.G. Kandlikar. *Water management studies in PEM fuel cells, part III: Dynamic breakthrough and intermittent drainage characteristics from GDLs with and without MPLs*. International Journal of Hydrogen Energy 35 (2010) 4222-4333.

[106] NIST Standard Reference Database 106, IUPAC-NIST Solubility Database, 2003.

[107] Z.H. Wang, C.Y. Wang. *Mathematical modeling of liquid-feed direct methanol fuel cells*. Journal of The Electrochemical Society 150 (2003) A508-A519.

[108] K. Scott, W. Taama, J. Cruickshank. *Performance and modelling of a direct methanol solid polymer electrolyte fuel cell*. Journal of Power Sources 65 (1997) 159-171.

[109] H. Guo, C. Ma. *2D analytical model of a direct methanol fuel cell*. Electrochemistry Communications 6 (2004) 306-312.

[110] A.A. Kulikovsky, J. Divisek, A.A. Kornyshev. *Two-dimensional simulation of direct methanol fuel cell. A new (embedded) type of current collector*. Journal of The Electrochemical Society 147 (2000) 953-959.

[111] J. Ge, H. Liu. *A three-dimensional mathematical model for liquid-fed direct methanol fuel cells*. Journal of Power Sources 160 (2006) 413-421.

[112] S.Lj. Gojković, T.R. Vidaković, D.R. Durovic. *Kinetic study of methanol oxidation on carbon-supported PtRu electrocatalyst*. Electrochimica Acta 48 (2003) 3607-3614.

[113] R.H. Perry, D.W. Green. *Perry's chemical engineer's handbook*. McGraw Hill 1999.

[114] T. Tschinder, T. Schaffer, S.D. Fraser, V. Hacker. *Electro-osmotic drag of methanol in proton exchange membranes*. Journal of Applied Electrochemistry 37 (2007) 711-716.

[115] A.Z. Weber, J. Newman. *Transport in polymer-electrolyte membranes - I. Physical model*. Journal of The Electrochemical Society 150 (2003) A1008-A1015.

[116] A.Z. Weber, J. Newman. *Transport in polymer-electrolyte membranes - II. Mathematical model*. Journal of The Electrochemical Society 151 (2004) A311-A325.

[117] X.Z. Yuan, C. Song, H. Wang, J. Zhang. *Electrochemical impedance spectroscopy in PEM fuel cells*. Springer 2010.

[118] J.T. Müller, P.M. Urban. *Characterization of direct methanol fuel cells by ac impedance spectroscopy*. Journal of Power Sources 75 (1998) 139-143.

[119] J.T. Müller, P.M. Urban, W.F. Hölderich. *Impedance studies on direct methanol fuel cell anodes*. Journal of Power Sources 84 (1999) 157-160.

[120] J.P. Diard, N. Glandut, P. Landaud, B.L. Gorrec, C. Montella. *A method for determining anode and cathode impedances of a direct methanol fuel cell running on a load*. Electrochimica Acta 48 (2003) 555-562.

[121] X. Wang, J.M. Hu, I.M. Hsing. *Electrochemical investigation of formic acid electro-oxidation and its crossover through a Nafion® membrane*. Journal of Electroanalytical Chemistry 562 (2004) 73-80.

[122] C.M. Lai, J.C. Lin, K.L. Hsueh, C.P. Hwang, et al. *On the accelerating degradation of DMFC at highly anodic potential*. Journal of The Electrochemical Society 155 (2008) B843-B851.

[123] S.K. Roy, M.E. Orazem. *Error analysis of the impedance response of PEM fuel cells*. Journal of The Electrochemical Society 154 (2007) B883-B891.

[124] P. Piela, R. Fields, P. Zelenay. *Electrochemical impedance spectroscopy for direct methanol fuel cell diagnostics*. Journal of The Electrochemical Society 153 (2006) A1902-A1913.

[125] S.H. Yang, C.Y. Chen, W.J. Wang. *An impedance study of an operating direct methanol fuel cell*. Journal of Power Sources 195 (2010) 2319-2330.

[126] M. Ciureanu, R. Roberge. *Electrochemical impedance study of PEM fuel cells. Experimental diagnostics and modeling of air cathodes*. The Journal of Physical Chemistry 105 (2001) 3531-3539.

[127] Z. Xie, S. Holdcroft. *Polarization-dependent mass transport parameters for orr in perfluorosulfonic acid ionomer membranes: an EIS study using microelectrodes*. Journal of Electroanalytical Chemistry 568 (2004) 247-260.

[128] X. Yuan, H. Wang, J.C. Sun, J. Zhang. *AC impedance technique in PEM fuel cell diagnosis-A review*. International Journal of Hydrogen Energy 32 (2007) 4365-4380.

[129] Q. Guo, R.E. White. *A steady-state impedance model for a PEMFC cathode*. Journal of The Electrochemical Society 151 (2004) E133-E149.

[130] F. Jaouen, G. Lindbergh. *Transient techniques for investigating mass-transport limitations in gas diffusion electrodes. I. Modeling the PEFC cathode*. Journal of The Electrochemical Society 150 (2003) A1699-A1710.

[131] M. Chen, C.Y. Dub, G.P. Yin, P.F. Shi, T.S. Zhao. *Numerical analysis of the electrochemical impedance spectra of the cathode of direct methanol fuel cells*. International Journal of Hydrogen Energy 34 (2009) 1522-1530.

[132] M. Zago, A. Casalegno, C. Santoro, R. Marchesi. *Water transport and flooding in DMFC: experimental and modeling analyses*. Journal of Power Sources 217 (2012) 381-391.

[133] S.H. Yang, C.Y. Chen, W.J. Wang. *An impedance study for the anode micro-porous layer in an operating direct methanol fuel cell*. Journal of Power Sources 195 (2010) 3536-3545.

[134] Y.J. Kim, W.H Hong, S.I. Woo, H.K. Lee. *Analysis of the polarization of a direct methanol fuel cell using a pseudo-reversible hydrogen reference electrode*. Journal of Power Sources 159 (2006) 491-500.

[135] H. Dohle, J. Divisek, J. Mergel, H.F. Oetjen, et al. *Recent developments of the measurement of the methanol permeation in a direct methanol fuel cell*. Journal of Power Sources 105 (202) 274-282.

[136] C. Ming Lai, J.C. Lin, K.L. Hsueh, C.P. Hwang, et al. *On the electrochemical impedance spectroscopy of direct methanol fuel cell*. International Journal of Hydrogen Energy 32 (2007) 4381-4388.

[137] T.L. Liu, C. Pan. *Visualization and back pressure analysis of water transport through gas diffusion layers of proton exchange membrane fuel cell*. Journal of Power Sources 207 (2012) 60-69.

[138] X. Zhu, P.C. Sui, N. Djilali. *Three-dimensional numerical simulations of water droplet dynamics in a PEMFC gas channel*. Journal of Power Sources 181 (2008) 101-115.

[139] Y. Ding, H.T. Bi, D.P. Wilkinson. *Three-dimensional numerical simulation of water droplet emerging from a gas diffusion layer surface in micro-channels*. Journal of Power Sources 195 (2010) 7278-7288.

[140] X. Wang, T.V. Nguyen. *Modeling the effects of the microporous layer on the net water transport rate across the membrane in a PEM fuel cell*. Journal of The Electrochemical Society 157 (2010) B496-B505.

[141] D.A. Nield, A. Bejan. *Convection in porous media*. Springer 2006.

[142] F. Bresciani, A. Casalegno, M. Zago, R. Marchesi. *A parametric analysis on DMFC anode degradation*. Proceedings of fundamentals and development of fuel cell conference 2013, Karlsruhe, Germany.

List of Figures

List of Tables

List of Symbols

C	species concentration in channel ($mol \cdot cm^{-3}$)
$\bar{C}$	time-average concentration in channel ($mol \cdot cm^{-3}$)
C_{ref}	reference concentration ($mol \cdot cm^{-3}$)
D_{eff}	effective diffusivity ($cm^2 \cdot s^{-1}$)
D	diffusivity ($cm^2 \cdot s^{-1}$)
$\bar{D}$	time-avergae diffusivity ($cm^2 \cdot s^{-1}$)
h_{conv}	convective mass transport coefficient ($cm \cdot s^{-1}$)
R^G	mass transport coefficient in gas phase ($s \cdot cm^{-1}$)
E_0	ideal potential difference (V)
F	Faraday constant ($C \cdot mol^{-1}$)
h	channel height and width (cm)
L	channel length (cm)
l	thickness (cm)
i	local current density ($A \cdot cm^{-2}$)
i_*	exchange current density ($A \cdot cm^{-2}$)
i_{*v}	volumetric exchange current density ($A \cdot cm^{-3}$)
K_H	Henry constant ($mol \cdot J^{-1}$)
M	molecular weight ($g \cdot mol^{-1}$)
$\dot{m}$	mass flow rate ($g \cdot min^{-1}$)
K	permeability (m^2)
N^{H_2O}	water flux ($mol \cdot cm^{-2} \cdot s^{-1}$)
N^{CH_3OH}	methanol flux ($mol \cdot cm^{-2} \cdot s^{-1}$)
N	flux ($mol \cdot cm^{-2} \cdot s^{-1}$)
X	mass molar fraction (% or $\%wt$)
η_d	water drag coefficient
η_{dx}	methanol drag coefficient
p	channel pressure (Pa)
p_{sat}	saturation pressure (MPa)
p_{lim}	threshold breakthrough pressure (Pa)
p_c	capillary pressure (Pa)

R	universal gas constant ($J \cdot mol^{-1} \cdot K^{-1}$)
T	fuel cell temperature (K)
v	local velocity in channel ($cm \cdot s^{-1}$)
$J(s)$	Leverett function
s	liquid saturation
$\bar{s}_{GDL}$	average liquid saturation across GDL
CF	correction factor
H	dimensionless frequency
Z	impedance (Ω or $\Omega \cdot cm^2$)
R_{ct}	charge transfer resistance (Ω or $\Omega \cdot cm^2$)
Z_{mt}	mass transfer impedance (Ω or $\Omega \cdot cm^2$)
R_{cov}	coverage resistance (Ω or $\Omega \cdot cm^2$)
L_{cov}	coverage inductance (H or $H \cdot cm^2$)

Greek symbol

α	Tafel transport coefficient
γ	reaction order
ε	volumetric void fraction
η	polarization (V)
ρ	compound density ($g \cdot cm^{-3}$)
μ	compound viscosity ($Pa \cdot s$)
ϵ	porosity
θ_c	contact angle (^{o})
σ_m	membrane conductivity ($\Omega^{-1} \cdot cm^{-1}$)
σ_{H_2O}	surface tension ($N \cdot m^{-1}$)
σ_t	electrode proton conductivity ($\Omega^{-1} \cdot cm^{-1}$)
Γ	active site density ($mol \cdot cm^{-2}$ or $mol \cdot cm^{-3}$)
γ_k	surface coverage by k intermediate
ω	angular frequency ($rad \cdot s^{-1}$)
Δi	oscillation of current density ($A \cdot cm^{-2}$)
$\Delta\eta$	oscillation of overpotential (V)
ΔC	oscillation of concentration ($mol \cdot cm^{-3}$)
ΔN	oscillation of flux ($mol \cdot cm^{-2} \cdot s^{-1}$)
$\Delta\gamma$	oscillation of surface coverage
Δs	oscillation of liquid saturation
δ	characteristic length (cm)
ζ	dimensionless position
Θ	dimensionless concentration
$\bar{\Delta C}^{GDL}$	average concentration difference across GDL ($mol \cdot cm^{-3}$)

Superscript

a	relative to anode
c	relative to cathode
t	relative to catalyst layer
m	relative to membrane
GDL	relative to gas diffusion layer
G	relative to gas phase
L	relative to liquid phase
sat	relative to saturation
o	relative to steady-state
$\sim$	relative to oscillating component

Subscript

GDL	relative to gas diffusion layer
MPL	relative to micro porous layer
m	relative to membrane
el	relative to electrode
ch	relative to channel
eq	relative to equilibrium
CO_2	relative to carbon dioxide
CO	relative to carbon monoxide
H_2O	relative to water
CH_3OH	relative to methanol
N_2	relative to nitrogen
O_2	relative to oxygen
air	relative to air
in	relative to inlet
out	relative to outlet
$drag$	relative to electro-osmotic drag
$diff$	relative to diffusion
$cross$	relative to cross-over
$perm$	relative to permeation
tot	relative to total
$conv$	relative to convective
ox	relative to oxidation
rd	relative to reduction
1	relative to first reaction step
2	relative to second reaction step
Pt	relative to platinum